ρ^0 Photoproduction using Linearly Polarised Photons with the CLAS Detector

by

Christopher Ian Osyp Gordon

Presented as a Thesis for the Degree of Doctor of Philosophy

Nuclear Physics Group
Department of Physics and Astronomy
University of Glasgow

Abstract

The work presented in this thesis describes the first experimental measurement of the photon asymmetry of the exclusive $\overrightarrow{\gamma}\mathrm{p} \rightarrow \rho^0\mathrm{p} \rightarrow \pi^+\pi^-\mathrm{p}$ reaction. The data were gathered during the summer of 2001 as a proof of principle study using a polarised beam of photons with the CLAS [1] detector in Hall B of Jefferson Lab [2] for the first time. The aim of the g8a [3, 4, 5, 6] set of experiments is to improve the understanding of the underlying symmetry of the quark degrees of freedom in the nucleon, the nature of the parity exchange between the incident photon and the target nucleon, the mechanism of associated strangeness production in electromagnetic reactions, and to search for evidence for the existence of the so called 'missing resonances'.

A beam of tagged and collimated linearly polarised photons (energy range 1.8-2.2 GeV) in conjunction with the large solid angle coverage of CLAS make possible the extraction of polarisation observables for the photoproduction of vector mesons. For example, the azimuthal distribution of the ρ^0 as a function of its polar angle in the $(\overrightarrow{\gamma}, \mathrm{p})$ c.m. system enables the measurement of the photon asymmetry parameter, Σ. This has been measured for $\theta_{\mathrm{c.m.}} \leq 65^\circ$, the results of which are compared with the prediction of the quark model of Zhao [7] for the ω vector meson. It has been found that the tensor coupling for the ρ^0 is quite different than that of the ω.

The experimental technique of using a beam of linear polarised photons with the CLAS detector has been shown to be viable. By the end of the second phase of these experiments we expect to have a high quality data set which will allow the measurement of the spin density matrix elements for the ρ^0 and provide evidence relating to the existence of the missing resonances.

Declaration

The data presented in this thesis were obtained as part of the g8a collboration at Jefferson Laboratory, Virginia, USA, and the Nuclear Physics Experiment Group, The University of Glasgow. I participated fully in the preparation and execution of the experiment. The analysis of the experimental data is my own work. This thesis was composed by myself.

Christopher Ian Osyp Gordon

March 2004.

Contents

List of Figures

List of Tables

Chapter 1

Introduction

In 1964 the Standard Model of the physical world was put forward by Gell-Mann and his collaborators [8]. In this model all hadrons consist of elementary particles and their anti-particles which have fractional charge. Gell-Mann called the particles "quarks". At the beginning there were only thought to be three quarks, but it is now known that there are six quarks which are grouped into three flavours. Table 1.1 contains some properties of these.

Name	Symbol	Q/e	Spin	Mass (GeV/c^2)
up	u	$\frac{2}{3}$	$\frac{1}{2}$	0.004
down	d	$-\frac{1}{3}$	$\frac{1}{2}$	0.008
charm	c	$\frac{2}{3}$	$\frac{1}{2}$	1.5
strange	s	$-\frac{1}{3}$	$\frac{1}{2}$	0.15
top	t	$\frac{2}{3}$	$\frac{1}{2}$	176
bottom	b	$-\frac{1}{3}$	$\frac{1}{2}$	4.7

Table 1.1: A summary table of some properties of the six known quarks.

Within the framework of the standard model a meson can be described as a state containing one quark and one anti-quark ($q\overline{q}$) and a baryon as a state containing three quarks (qqq). In this model Quantum Chromodynamics (QCD) [9] describes the interaction of quarks as through the exchange of gluons, which couple with the *colour* charge of the quarks. The colour of a quark can be red, green, or blue, and for an anti-quark it can be anti-red, anti-green, or anti-blue. Allowed hadronic states must be overall colourless. The production of these states is limited not only by the requirements of energy and momentum conservation, but also by the conservation of the appropriate quantum numbers for a particular type of interaction to occur.

Using these laws and combinations of the three lightest quarks the standard model is able to predict the spectrum of ground states for mesons and baryons very well. These ground states can be excited into higher energy states, which are known as resonances. Fig. 1.1 shows the photoproduction cross-section on the proton in the $E_{c.m.} = 1.1 - 2.5\,\mathrm{GeV}$ region [10]. The $\Delta(1232)$ resonance excitation is associated with the first of the four resonance regions in the $\gamma p \rightarrow$ Hadrons curve. This is also known as the $P_{33}(1232)$ resonance, following the notation L_{2I2J}, where L is the orbital angular momentum of the resonance in spectroscopical notation (S,P,D,F corresponding to L=0,1,2,3), and I (J) is the isospin (total angular momentum) of the resonance. It can be seen that as the energy increases the threshold for more decay modes is surpassed and it becomes increasingly difficult to identify individual states.

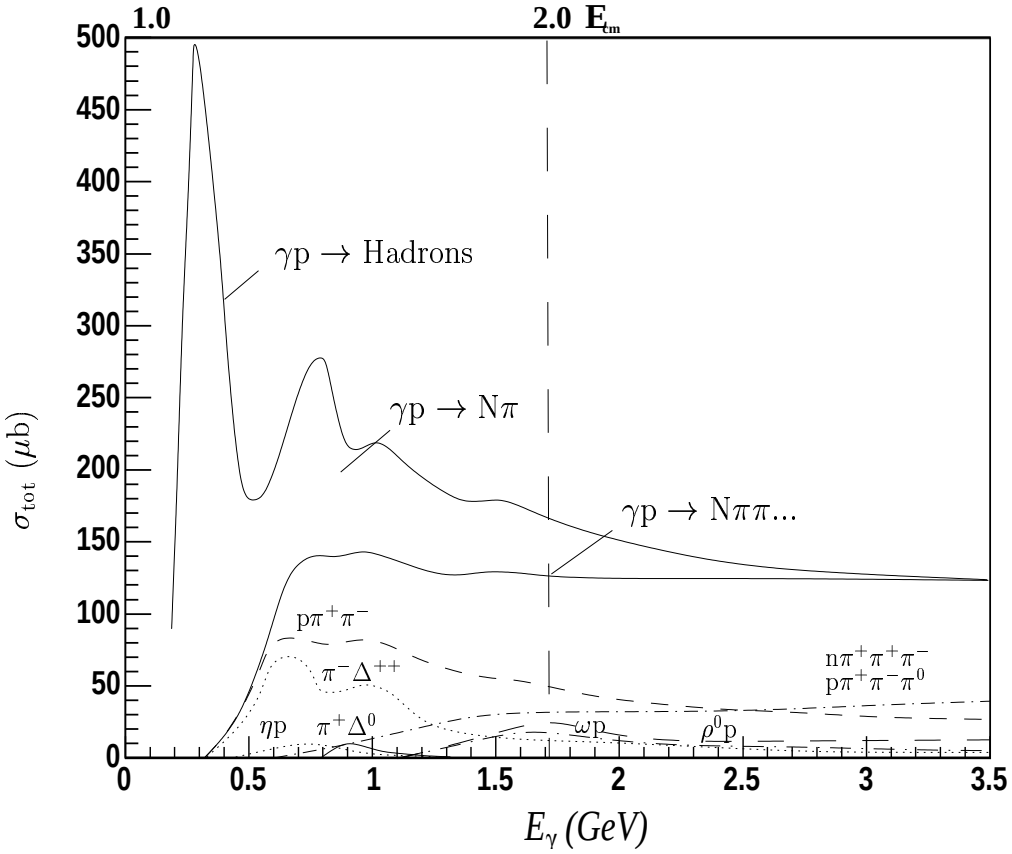

Figure 1.1: The photoproduction cross-section on the proton for the $E_{c.m.} = 1.1$-2.5 GeV range. Four resonance regions can be seen with the one at the lowest energy being associated with the $\Delta(1232)$ resonance. Plot reproduced from Ref. [10].

The baryon resonances decay strongly and are therefore only in existence for a very short time ($\tau \approx 10^{-24}\,\mathrm{s}$). The observation of such an excited state is obtained through the detection of the decay products the state is allowed to emit. For example, the prominent transitions via meson emisson for the low lying states of the nucleon are shown in Fig. 1.2. In this case the measurement of the emitted mesons will lead to information of the nucleon resonance it decayed from.

As the spacing between individual resonances is often no more than $\sim 10\,\mathrm{MeV}$ and their widths are often $\geq 100\,\mathrm{MeV}$, to identify and investigate individual states with such an overlap is experimentally very difficult. A possible solution to this problem is through partial-wave-analysis (PWA) [11]. The partial wave formalism expands particle wave functions in terms of complex amplitudes, which are defined for given spin and parity. The information available from such analysis is typically insufficient to obtain unambiguous results, and additional physics assumptions are often introduced. Since these depend on the reaction under study, the approximations and limitations cannot easily be generalised. Using linear polarised photons as a probe provides added constraints in the analysis, which is desireable to have an increased knowledge of the processes leading to baryon resonance formation and decay.

A major problem in our current day understanding of baryon spectroscopy is that many of the resonances predicted by QCD in the $\mathrm{SU}(6) \otimes \mathrm{O}(3)$ symmetric quark model have not yet been observed. These are known as the "missing resonances". Most of our knowledge of this spectrum has come from the reactions $\pi\mathrm{N} \to \pi\mathrm{N}$, $\pi\mathrm{N} \to \pi\pi\mathrm{N}$, and $\gamma\mathrm{N} \to \pi\mathrm{N}$. Alternative descriptions such as the di-quark model [12, 13] have evolved to provide a solution to missing resonance problem. These restrict the number of internal degrees of freedom by assuming that two of the three quarks making up the baryon state are bound together. A solution has been put forward by Koniuk and Isgur [14] and others [15, 16] in the non-relativistic constituent quark model. In this model the missing resonances tend to couple weakly to the $\pi\mathrm{N}$ channel and strongly to the $\pi\pi\mathrm{N}$ channel.

Since most of the information on the baryon resonance spectrum has come from PWA of $\pi\mathrm{N} \to \pi\mathrm{N}$ measurements, the missing resonances may be simply due to a lack of experimental data. In Table 1.2 [17] the supermultiplet assignments for the measured and missing baryon resonances from the QCD-improved model of Cutkosky [18] are shown. The highlighted supermultiplets are fully consistent with the di-quark model and the star ratings are from the particle data group [19].

It is predicted that the missing resonances will have a reasonable coupling to

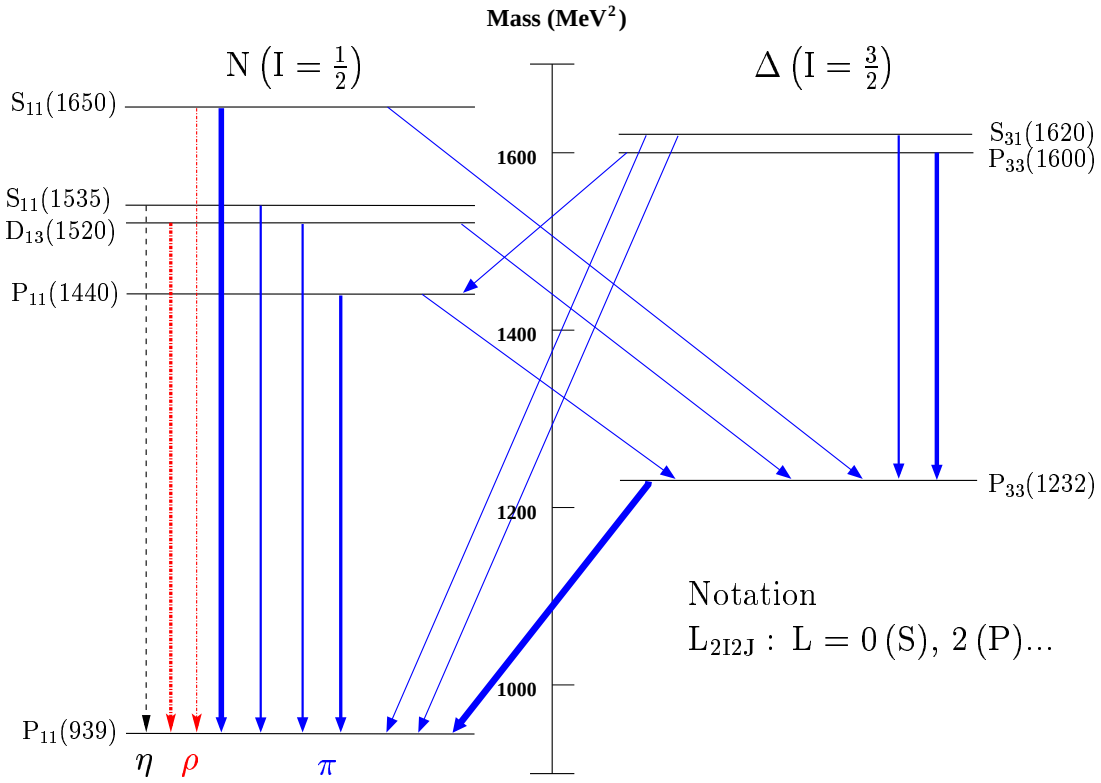

Figure 1.2: The low lying excited states of the nucleon with I=1/2 (left) and I=3/2 (right). The thickness of the arrows represent the main branching ratios via $\eta-$emission (dashed), $\rho-$emission (dash-dot), and $\pi-$emission (solid).

N^*	**Status**	$SU(6) \otimes O(3)$	**Parity**	Δ^*	**Status**	$SU(6) \otimes O(3)$
$P_{11}(938)$	****	$(56, 0^+)$	+	$P_{33}(1232)$	****	$(56, 0^+)$
$S_{11}(1535)$	****	$(70, 1^-)$				
$S_{11}(1650)$	****	$(70, 1^-)$		$S_{31}(1620)$	****	$(70, 1^-)$
$D_{13}(1520)$	****	$(70, 1^-)$	-	$D_{33}(1700)$	****	$(70, 1^-)$
$D_{13}(1700)$	***	$(70, 1^-)$				
$D_{15}(1675)$	****	$(70, 1^-)$				
$P_{11}(1520)$		$(56, 0^+)$		$P_{31}(1875)$	****	$(56, 2^+)$
$P_{11}(1710)$	***	$(70, 0^+)$	+	$P_{31}(1835)$		$(70, 0^+)$
$P_{11}(1880)$		$(70, 2^+)$				
$P_{11}(1975)$		$(20, 1^+)$				
$P_{13}(1720)$	****	$(56, 2^+)$		$P_{33}(1600)$	***	$(56, 0^+)$
$P_{13}(1870)$		$(70, 0^+)$		$P_{33}(1920)$	***	$(56, 2^+)$
$P_{13}(1910)$		$(70, 2^+)$	+	$P_{33}(1985)$		$(70, 2^+)$
$P_{13}(1950)$		$(70, 2^+)$				
$P_{13}(2030)$		$(20, 1^+)$				
$F_{15}(1680)$	****	$(56, 2^+)$		$F_{35}(1905)$	****	$(56, 2^+)$
$F_{15}(2000)$	**	$(70, 2^+)$	+	$F_{35}(2000)$	**	$(70, 2^+)$
$F_{15}(1995)$		$(70, 2^+)$				
$F_{17}(1990)$	**	$(70, 2^+)$	+	$F_{37}(1950)$	****	$(56, 2^+)$

Table 1.2: The $SU(6) \otimes O(3)$ supermultiplet assignments from the QCD-improved model of Cutkosky [18] for the measured and missing baryon resonances. The highlighted supermultiplets are fully consistent with the di-quark model. Star ratings are from the particle data group [19].

the photon. It is for this reason that recent photoproduction experiments have been carried out at TJNAF [2] and other laboratories [20, 21, 22], employing an unpolarised beam of photons and searching for resonances decaying via the ρN channel amongst others. Due to the large number of resonances in conjunction with their broad widths and narrow spacing, this is experimentally a very difficult task. However, by performing similar photoproduction experiments using a beam of linearly polarised photons several more constraints can be placed on the physics of the underlying interactions. This is the motivation for the g8 set of experiments [3, 4, 5, 6] which ran at TJNAF in the summer of 2001. The g8 experiments saw the commissioning of the linearly polarised photon beamline with the CLAS detector [1] in Hall B, and ran in the photon energy range 1.8-2.2 GeV.

The ultimate aim of the analysis of the $\overrightarrow{\gamma}\mathrm{p} \rightarrow \rho^0\mathrm{p} \rightarrow \pi^+\pi^-\mathrm{p}$ channel is to measure the spin density matrix elements, which are discussed further in Chapter 2.4. Also offered within this data-set is the opportunity to make the first measurement of the photon asymmetry (Σ) for ρ^0 photo-production. The following chapter serves as a brief introduction to the theory of ρ^0 photo-production and explains how Σ is to be measured. Chapter 3 presents an overview of all the main detector systems used to aquire the data, while Chapter 4 documents the extensive calibration and data-processing procedures which must be applied before any final physics analysis is carried out. In Chapter 5 the particle identification technique is explained along with the corrections applied to particle four-momenta. The measurements of Σ are presented in Chapter 6 and in Chapter 7 the results are compared with the predictions of Zhao, Li, and Bennhold [7] who describe the photoproduction of vector mesons with an effective Lagrangian in the quark model.

Chapter 2

Theoretical Background

2.1 Cross Sections and the Resonance Region

As mentioned in Chapter 1 the strong interaction has mainly been studied with the scattering of hadrons from hadrons. A comparison of the differential cross sections [23] of $\pi^-\mathrm{p} \to \pi^-\mathrm{p}$ elastic scattering and $\gamma\mathrm{p} \to \rho^0\mathrm{p}$ photoproduction is shown in Fig. 2.1. It can be seen that both sets of data demonstrate very similar trends for comparable energies. The main difference is the photoproduction amplitude is smaller by a ratio approximately equal to the fine structure constant, $\alpha_{\mathrm{e.m.}}$. Similar trends can also be seen when looking at a comparison of the total cross sections for the same reactions in Fig. 2.2. The enhancements below centre-of-mass energy $\sqrt{\mathrm{s}}$ ~3 GeV are known as the *resonance region.* Following this the total cross sections are observed to be nearly independent of energy until $\sqrt{\mathrm{s}}$ ~10 GeV and then rises with increasing $\sqrt{\mathrm{s}}$ due to pomeron exchange [24].

There have been two types of approach when attempting to model the behaviour in the diffractive cross section data. One is based on QCD where quarks and gluons are exchanged. The other approach is Regge theory [26] in which hadronic degrees of freedom are used to describe the process by considering the reaction to proceed with the exchange of mesons in the t-channel (see Chapter 2.2 for definition) which have similar quantum numbers. In this description the exchange mesons are said to lie along the same *Regge trajectory,* thus the reaction is termed Reggeon exchange.

The similar behaviour of the differential cross section of the processes in Fig. 2.1 have led to the idea that the photon has intrinsic hadronic properties when used to probe the proton target. This interpretation is called the Vector Meson Dominance model of the photon (VMD). The quantum numbers of the

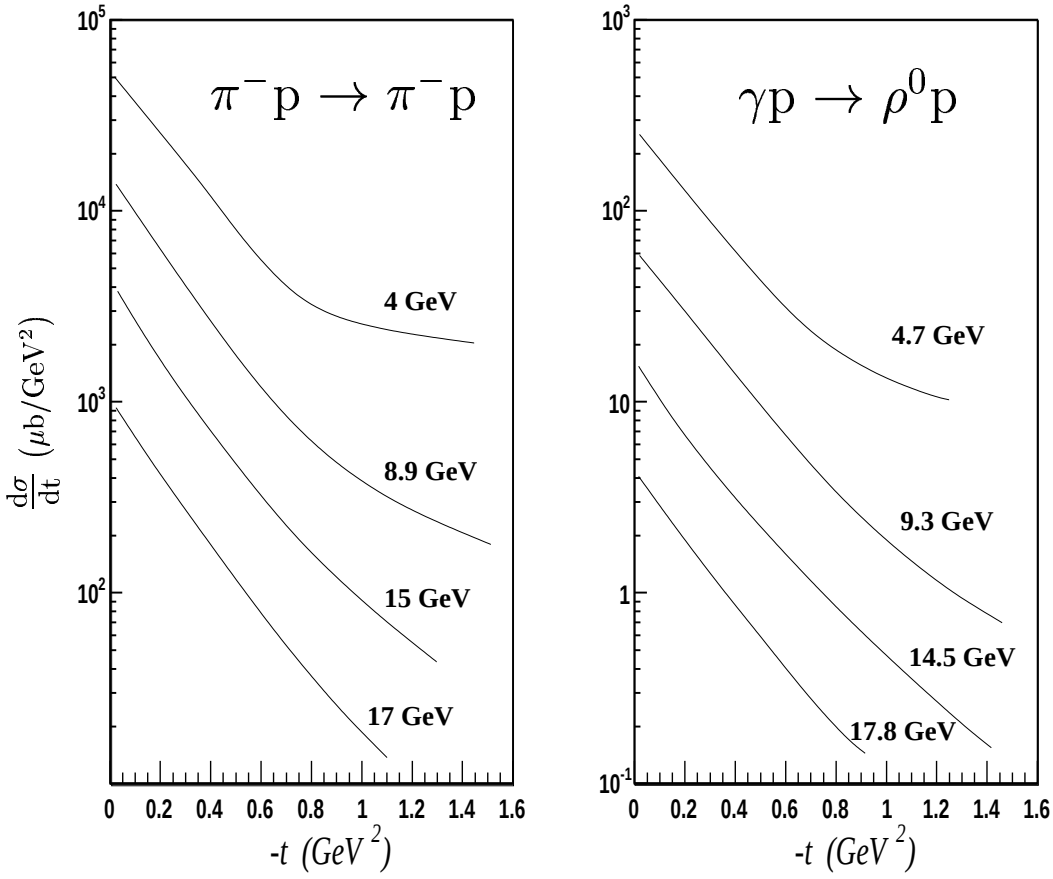

Figure 2.1: The differential cross sections of $\pi^- p \rightarrow \pi^- p$ elastic scattering and $\gamma p \rightarrow \rho^0 p$ photoproduction versus the momentum transfer to the target proton, -t. At forward angles (small t) the differential cross section is observed to fall sharply at all energies for both processes. These plots have been reproduced from Ref [23].

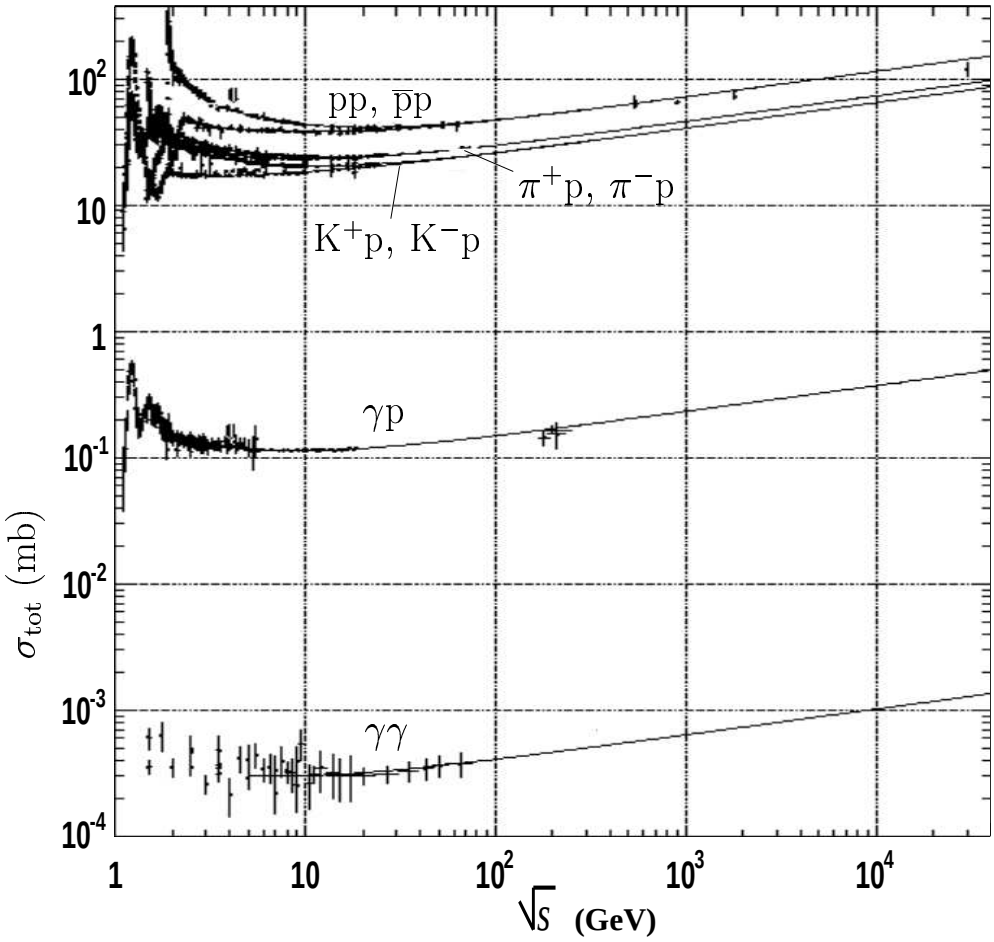

Figure 2.2: The total cross section (σ) for several hadron-p and $\gamma-$p reactions shown as a function of centre-of-mass energy ($\sqrt{s}$). The lines represent Regge fits to the data which show σ does not have a strong dependence on the type of incident particle. This plot is obtained from Refs. [19, 25].

photon are $J^{PC} = 1^{--}$, which are the same as that of vector mesons. In the VMD model the $\gamma - N$ interaction is therefore considered to proceed with the photon fluctuating into a $q\overline{q}$ pair which forms a light vector meson that then undergoes diffractive scattering off the nucleon via the strong interaction.

The first results of the total photoproduction cross section of the ρ^0 and other light vector mesons were published in the late 1960s. Fig. 2.3 shows the total photon reaction cross section, σ_{tot}, along with the total photoproduction cross sections of the ρ^0 and some other vector mesons. With the VMD approach σ_{tot} can be described very well using the exchange of Regge trajectories. At higher energies in Fig. 2.3 it can be seen there is a slow increase for the total photoproduction cross sections of the ρ^0, ω and ϕ. This is attributed to the exchange of a Regge trajectory which has the quantum numbers of the vacuum, known as Pomeron exchange. As lower energies are reached the ρ^0 and ω total photoproduction cross sections increase sharply which is explained by increasing Reggeon exchange amplitudes for these reactions.

2.2 Processes Contributing to ρ^0 Photoproduction

There are four processes involved in the production of ρ^0 mesons. A set of Lorentz invariant quantities known as the Mandelstam variables (s, t and u) are used to describe three of the processes. These three variables describe the kinematics of multi-body final states when viewed as two incident and two outgoing systems. By definition s is equivalent to the square of the centre-of-mass energy of the reaction, t is the square of the four-momentum transfer in the direct channel, and u is the square of the four-momentum transfer in the exchange channel. The fourth process is diffractive scattering via Pomeron exchange. All four processes are represented in Fig. 2.4.

2.3 A Quark Model for the Photoproduction of Vector Mesons

The quark model [7, 29] for which this work will make comparison with is described here. The model consists of three processes;

1. s and u-channel vector meson production with an effective Lagrangian (S+U).

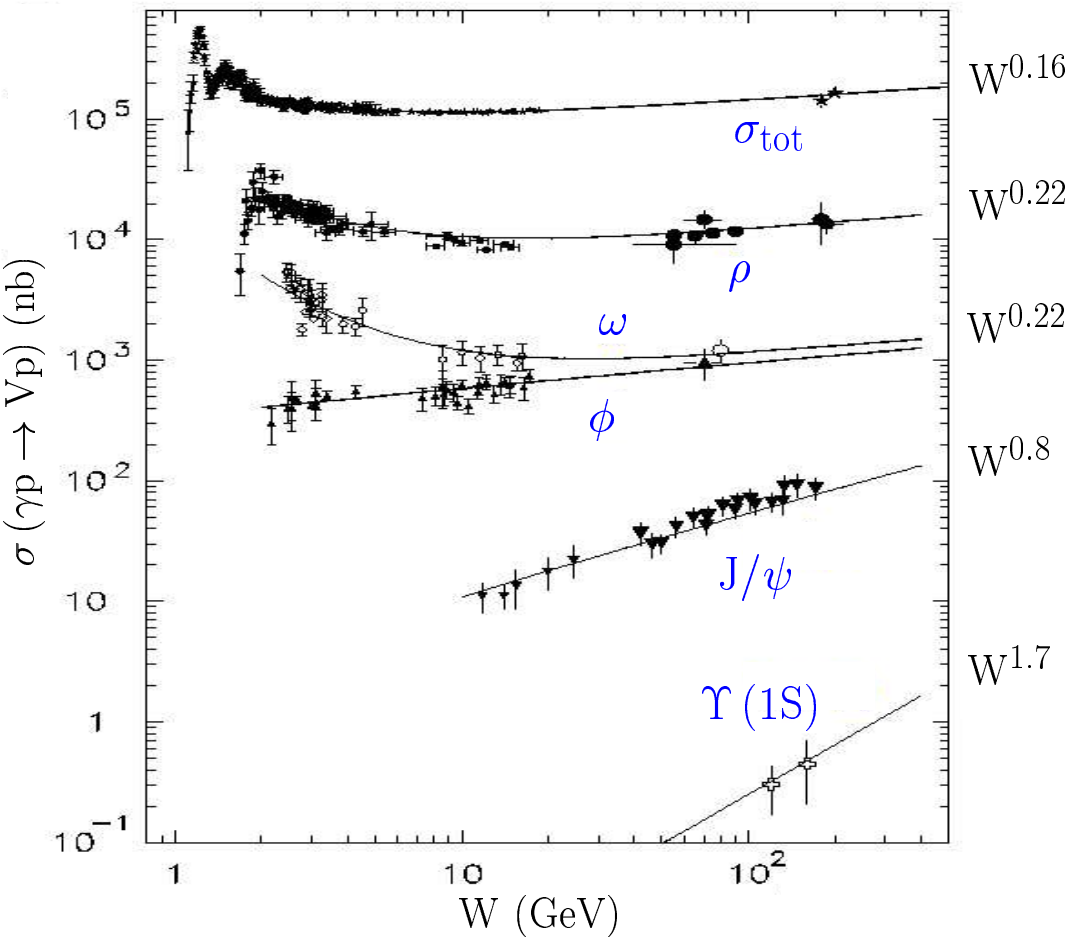

Figure 2.3: The total $\gamma-$p reaction cross section and the total photoproduction cross sections for several vector mesons shown as a function of the centre-of-mass energy (W). The lines represent Regge based power law fits from Refs. [27, 28]. This plot was obtained from Ref. [25].

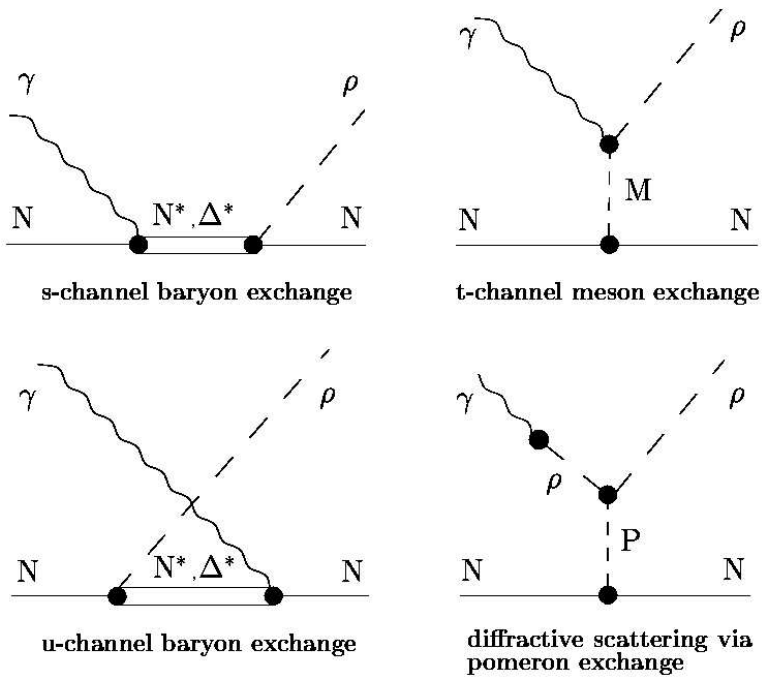

Figure 2.4: Born diagrams of the processes contributing to ρ^0 photoproduction.

2. t-channel Pomeron exchange (P) for ω, ρ^0 and ϕ production.

3. t-channel light meson exchange.

The starting point of the model is an effective Lagrangian of the interaction between the vector meson quarks inside the baryon as shown in Eqn. 2.1.

$$\mathrm{L_{eff}} = -\overline{\psi}\gamma_\mu \mathrm{p}^\mu \psi + \overline{\psi}\gamma_\mu \mathrm{e_q} \mathrm{A}^\mu \psi + \overline{\psi}\left(a\gamma_\mu + \frac{\mathrm{ib}\sigma_{\mu\nu}\mathrm{q}^\nu}{2\mathrm{m_q}}\right)\phi_\mathrm{m}^\mu \psi \tag{2.1}$$

Here the quark (anti-quark) field, ψ ($\overline{\psi}$), is represented by Eqn. 2.2 and the meson field, ϕ_m^μ, is a 3$\otimes$3 matrix as shown in Eqn. 2.3. The meson field treats the vector mesons as point-like particles. The mass and charge of the quark are represented by $\mathrm{m_q}$ and $\mathrm{e_q}$.

$$\psi = \begin{pmatrix} \psi\,(\mathrm{u}) \\ \psi\,(\mathrm{d}) \\ \psi\,(\mathrm{s}) \end{pmatrix} \tag{2.2}$$

$$\phi^{\mu}_{\mathrm{m}} = \begin{pmatrix} \frac{1}{\sqrt{2}}\rho^0 + \frac{1}{\sqrt{2}}\omega & \rho^+ & \mathrm{K}^{*+} \\ \rho^- & -\frac{1}{\sqrt{2}}\rho^0 + \frac{1}{\sqrt{2}}\omega & \mathrm{K}^{*0} \\ \mathrm{K}^{*-} & \overline{\mathrm{K}}^{*0} & \phi \end{pmatrix} \tag{2.3}$$

Resonance contributions at quark level are introduced using the quark-vector-meson effective couplings. The two types of coupling are vector and tensor which are represented by the parameters a and b respectively and allow the s-channel and u-channel resonances and nucleon pole terms to be included. These parameters are independent of quark model and can only be determined experimentally. A complete set of helicity amplitudes are included in the model for s-channel resonances below 2 GeV in the SU (6) $\otimes$ O (3) symmetry limit, with the resonances above 2 GeV being treated as degenerate in order to express each contribution from all resonances with quantum number n in a compact form.

While there has been insufficient data available to measure the vector and tensor couplings accurately for the ρ^0 there have been measurements for the ω vector meson. Due to the approximate isospin symmetry between the ω and ρ^0 the value of these couplings can then be used to make initial calculations of some observables for the ρ^0. While the vector couplings of both should be very similar the tensor couplings may well be very different [30]. In Chapter 7 the parameter $\mathrm{b}' = \mathrm{b} - \mathrm{a}$ has been varied and the calculated photon asymmetry (Σ) compared with the results from this work.

When compared with data from SAPHIR [31, 32] the model successfully reproduces both the differential and total cross-sections for $\gamma\mathrm{p} \rightarrow \omega\mathrm{p}$. These are shown in Figs. 2.5 and 2.6. In these calculations eight low-lying resonances (P_{11} 1440, S_{11} 1535, D_{13} 1520, P_{13} 1720, F_{15} 1680, P_{11} 1710, P_{13} 1900, and F_{15} 2000) with the quark harmonic oscillator shell $\mathrm{n} \leq 2$ are explicitly included, with the higher mass states treated as degenerate with n. A full comparison of data to theory is given in Ref. [33], but it is clear that the model succeeds well with the limited data available to date. In comparison with data from a recent ω electroproduction experiment [34, 35] at JLab, success has also been met as can be seen in Fig. 2.7. In summary the quark model has been shown to provide a solid framework on which a systematic investigation of resonance excitation in vector meson production can be built.

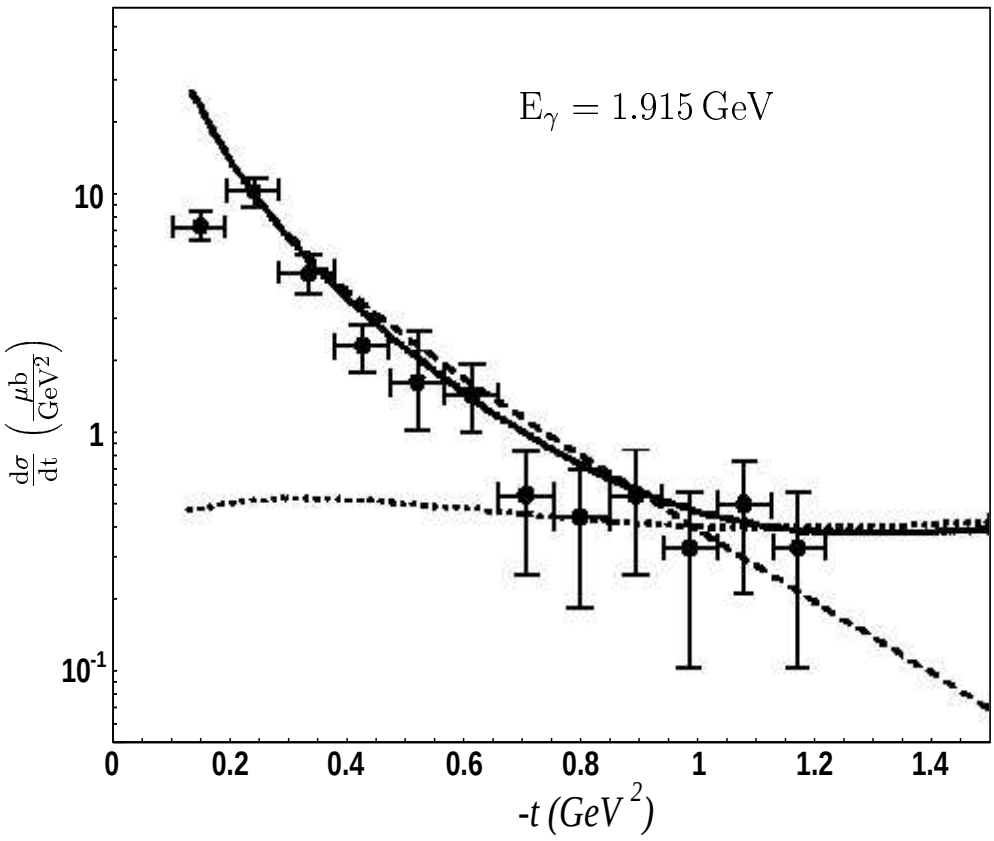

Figure 2.5: The differential cross-section (solid line) for $\gamma p \to \omega p$ as calculated with the quark model [7]. Data is from Ref. [31]. The π^0 exchanges are shown by the dashed curve and the dotted curve shows the contributions from s- and u-channel exclusively.

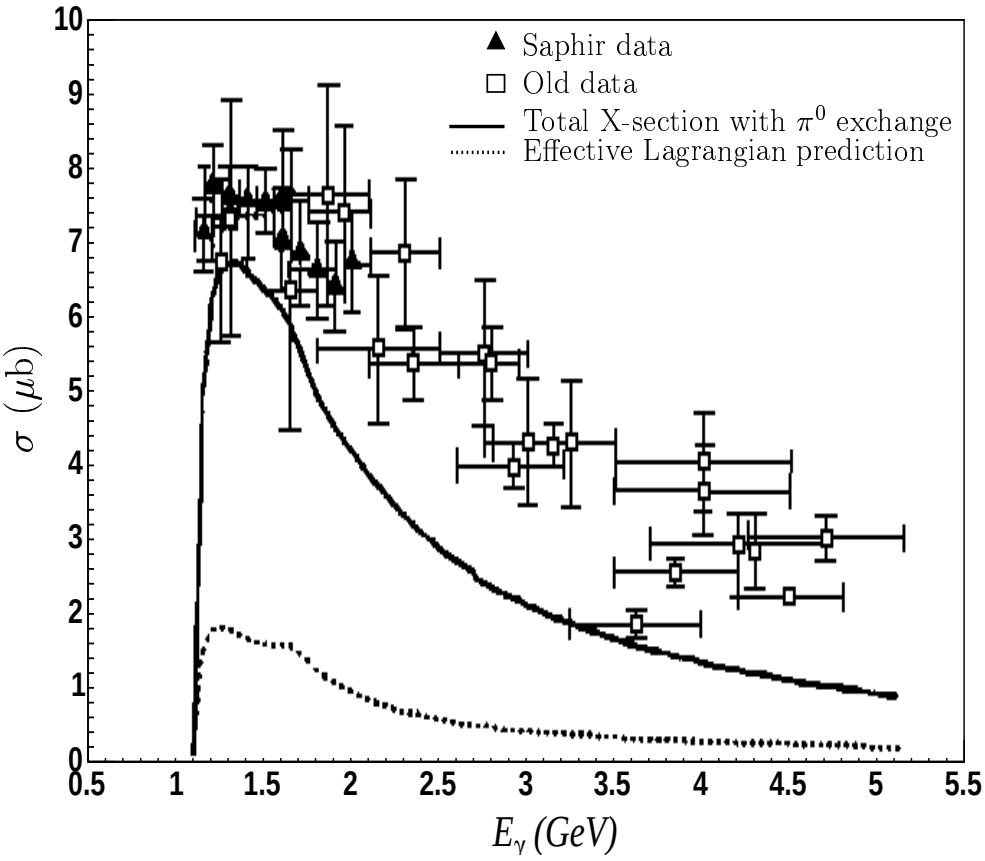

Figure 2.6: The total cross-section (solid line) for $\gamma p \to \omega p$ as calculated with the quark model [7] taking into account π^0 exchange. Data is from Refs [31, 36] (triangle) and Refs. [37, 38, 39, 40, 41, 42] (square). The dotted curve describes the pure s- and u-channel contributions.

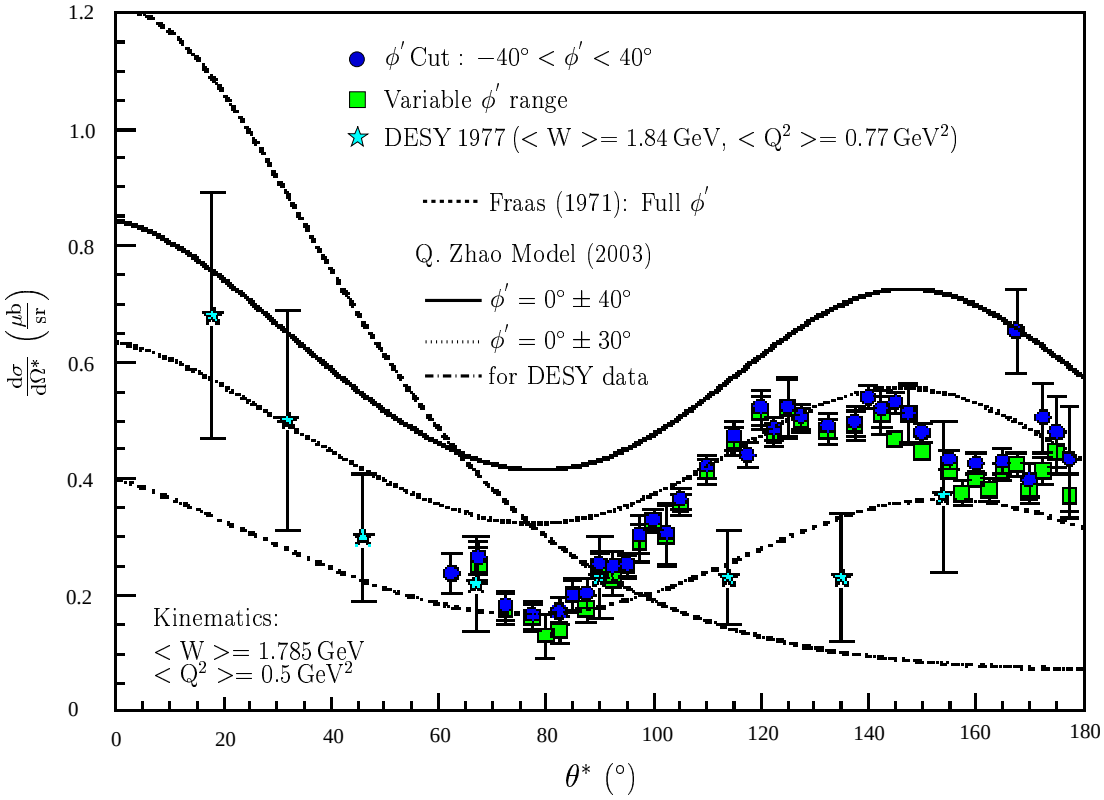

Figure 2.7: Recent ω electroproduction data from JLab [34, 35] compared with the quark model. θ^* is the polar angle in the total c.m. frame.

2.4 The Decay Angular Distribution

For vector meson production the final state vector meson decays allow the measurement of the density matrix elements of the vector meson decay. These can be related to the vector or tensor polarisations of the vector meson, or the complete decay angle distributions of the cross sections. For the $\rho^0 \to \pi^+\pi^-$ case the complete angular distribution $\mathrm{W}(\cos\theta, \phi, \Phi)$ is given by Eqn. 2.4.

$$\begin{aligned} \mathrm{W}(\cos\theta, \phi, \Phi) = \; & \mathrm{W}^0\left(\cos\theta, \phi, \rho^0_{\alpha\beta}\right) \; -\mathrm{P}_\gamma \cos 2\Phi \mathrm{W}^1\left(\cos\theta, \phi, \rho^1_{\alpha\beta}\right) \\ & -\mathrm{P}_\gamma \sin 2\Phi \mathrm{W}^2\left(\cos\theta, \phi, \rho^2_{\alpha\beta}\right) \end{aligned} \tag{2.4}$$

where

$$\begin{aligned} \mathrm{W}^0\left(\cos\theta, \phi, \rho^0_{\alpha\beta}\right) = \; & \tfrac{3}{4\pi}\left[\tfrac{1}{2}\sin^2\theta + \tfrac{1}{2}\left(3\cos^2\theta - 1\right)\rho^0_{00} \; -\sqrt{2}\Re e\rho^0_{10}\sin 2\theta\cos\phi \right. \\ & \left. -\rho^0_{1-1}\sin^2\theta\cos 2\phi\right] \\ \mathrm{W}^1\left(\cos\theta, \phi, \rho^1_{\alpha\beta}\right) = \; & \tfrac{3}{4\pi}\left[\rho^1_{11}\sin^2\theta + \rho^1_{00}\cos^2\theta \; -\sqrt{2}\Re e\rho^1_{10}\sin 2\theta\cos\phi \right. \\ & \left. -\rho^1_{1-1}\sin^2\theta\cos 2\phi\right] \\ \mathrm{W}^2\left(\cos\theta, \phi, \rho^2_{\alpha\beta}\right) = \; & \tfrac{3}{4\pi}\left[\sqrt{2}\mathrm{Im}\rho^2_{10}\sin 2\theta\sin\phi \; +\mathrm{Im}\rho^2_{1-1}\sin^2\theta\sin 2\phi\right] \end{aligned}$$

Here $\rho^n_{\alpha\beta}$ are the spin density matrix elements which determine the angular decay spectrum of the $\pi^+\pi^-$ decay of the ρ^0. The upper index n is related to the photon spin by the Pauli spin matrices and $\alpha, \beta = -1, 0, 1$ correspond to the possible helicity states of the ρ^0. θ and ϕ are the polar and azimuthal angles of the π^+ decay product in the helicity reference frame[1], P_γ is the degree of linear polarisation of the photon beam, and Φ is the angle between the photon polarisation vector and the ρ^0 production plane. These frames are represented in Fig. 2.8.

From Eqn. 2.4 it is clear that using a linearly polarised photon beam will give access to six more independent $\rho^n_{\alpha\beta}$ than can be obtained from using an unpolarised photon beam. The rigid constraints introduced by using a linearly polarised beam coupled with the large angular acceptance of CLAS will contribute to the advancement of our understanding of the baryon spectrum. The ultimate

[1]The helicity reference frame is defined as the rest frame of the ρ^0 with the spin quantisation axis (z-axis) in the opposite direction of the proton in the ρ^0 rest frame. Alternative reference frames such as the Gottfried-Jackson and Adair frames may also be used, these differ only in the choice of z-axis.

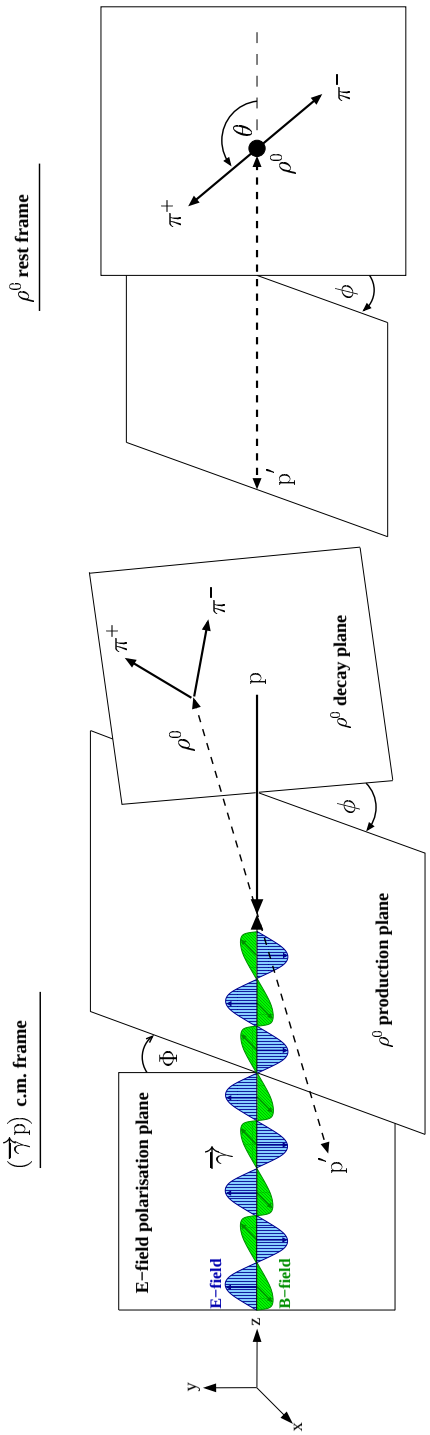

Figure 2.8: A representation of the $(\overrightarrow{\gamma}, \mathrm{p})$ c.m. frame and the rest frame of the ρ^0 with the z-axis defined as opposite the recoil proton, i.e. the helicity system.

aim of g8a experiment [3] is to measure the $\rho^n_{\alpha\beta}$ for ρ^0 photoproduction to improve our knowledge in this area. Due to the complexity of these measurements and a limited time frame, the scope of this work is limited to a first measurement of the photon asymmetry for ρ^0 photoproduction at low |t|.

2.5 Measurement of the Photon Asymmetry

The definition of the photon asymmetry parameter, Σ, is shown in Eqn. 2.5. Here $Y_{||}(Y_{\perp})$ is the yield of the ρ^0 emerging parallel (perpendicular) to the plane of polarisation defined by the electric vector of the incident photon beam.

$$\Sigma = \frac{Y_{||} - Y_{\perp}}{Y_{||} + Y_{\perp}} \tag{2.5}$$

In this analysis the photon asymmetry is measured in the $(\overrightarrow{\gamma}, p)$ c.m. system which is shown in Fig. 2.8. It is obtained by measuring the angle between the photon polarisation vector and the ρ^0 production plane, Φ, and from knowledge of the average degree of linear polarisation of the photon beam, P_γ. An integration of Eqn. 2.4 with respect to θ and ϕ results in the W (Φ) distribution to be of the form shown in Eqn. 2.6.

$$W(\Phi) = 1 - \Sigma P_\gamma \cos 2\Phi \tag{2.6}$$

where $\Sigma = \rho^1_{00} + 2\rho^1_{11}$ in terms of the spin density matrix elements, and all other parameters are as described previously. In experiment, what is actually measured to extract Σ is shown in Eqn. 2.7.

$$W_{pol} = W_{amo}(1 - \Sigma P_\gamma \cos 2\Phi) \tag{2.7}$$

where W_{pol} is the distribution of Φ obtained from data taken with the linearly polarised photon beam and W_{amo} is the distribution of Φ obtained from data set taken with an unpolarised beam of photons, which is referred to as amorphous data[2]. Examples of polarised distributions obtained from an experiment [43] using the cylindrically symmetric 4π detector DAPHNE at the Mainz Laboratory [44] are shown in Fig. 2.9. In this experiment the $p\left(\overrightarrow{\gamma}, p'\right)\pi^0$ reaction was measured using 270 to 420 MeV tagged linearly polarised photons, with Σ being measured

[2]The unpolarised beam of photons is produced via the bremsstrahlung method using a carbon radiator, which has no regular crystalline structure, hence the term amorphous.

from the angular distributions of the recoil proton. In the right hand plot the polarisation plane has been rotated by 90° with respect to that used in the left hand plot resulting in a phase-shift of 90° in the azimuthal distribution of the recoil proton.

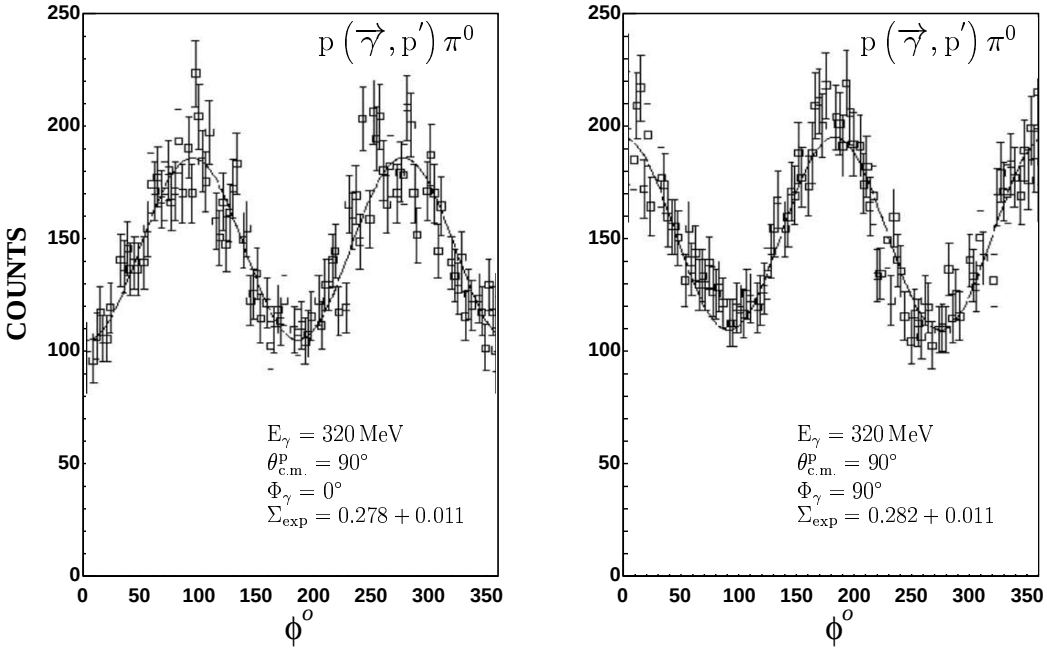

Figure 2.9: The azimuthal distribution of the recoil proton from the $p\left(\overrightarrow{\gamma},p'\right)\pi^0$ reaction measured from experimental data [43] acquired using the DAPHNE detector at the Mainz Laboratory [44]. The only difference between both distributions is that the polarisation plane has been rotated by 90°resulting in a phase-shift of 90° in the azimuthal distribution of p'.

The measurement of $\frac{W_{pol}}{W_{amo}}$ allows the determination of Σ without the need for measuring cross-sections or to carry out a simulation of the detector acceptance. This is because the systematic errors and detector efficiencies cancel out in what is known as the *normalisation* process. In this process analysis on both data sets using the same kinematical cuts and bins in $\theta_{c.m.}$ is carried out. After this W_{amo} is scaled relative to W_{pol} in order to account for the different number of entries in each distribution, then W_{pol} is divided through by the scaled W_{amo} distribution. By fitting the normalised $W(\Phi)$ distribution over 2π it is possible to use the amplitude of the cosine function with a measurement of the average degree of linear polarisation to establish the photon asymmetry parameter. This

method is represented graphically in Fig. 2.10.

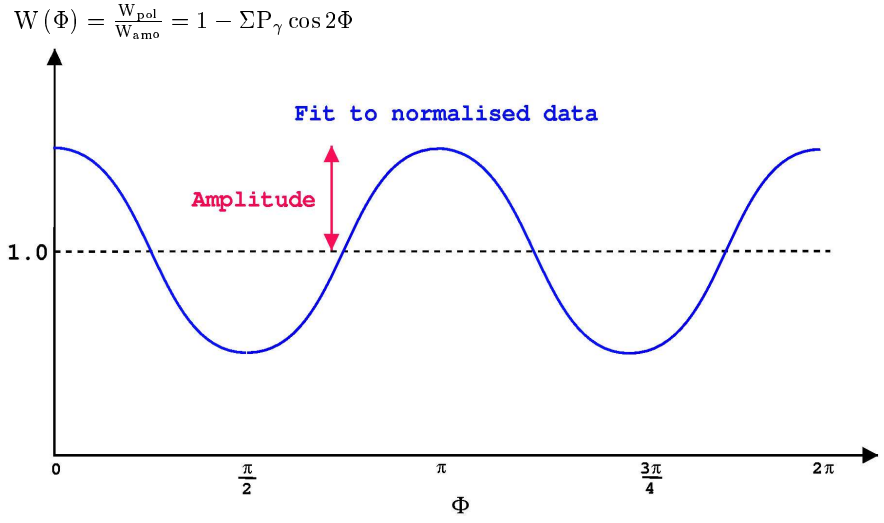

Figure 2.10: A diagram showing how the normalised $W(\Phi)$ distribution is fitted to ascertain Σ.

The measurements of Σ using the method as described above will be presented in Chapter 6.4. In the following Chapter, I will present an overview of all the main detector systems used to aquire the data to make these measurments.

Chapter 3

Experimental Apparatus

3.1 Introduction

This experiment was conducted using the facilities of the Thomas Jefferson National Accelerator Facility (TJNAF), Virginia, USA. The facility is dedicated to investigating the electromagnetic structure of mesons, nucleons, and nuclei, using either an electron or a photon beam. There are three end stations, Halls A, B, and C, that can receive the recirculating electron beam simultaneously. Each hall contains complementary experimental equipment to enable the TJNAF to address a wide range of physics issues. The experimental data was obtained from the g8a run in Hall B of TJNAF, during the period June to August of 2001. The g8a run was the commissioning experiment for the linearly polarised photon beam at CLAS.

3.2 Accelerator

The laboratory has a recirculating linear electron accelerator that supplies three experimental halls with a continuous beam of electrons of energies up to ~ 6 GeV. The accelerator itself consists of two linear accelerators in parallel, which are connected at the ends by five recirculation arcs. Fig. 3.1 shows the relative location of the accelerator, experimental halls, and other main buildings.

Electrons of energies ~ 67 MeV are injected into the first linac, which is essentially a procession of twenty cryomodules. The injected electrons are obtained by the process of thermionic emission, and passed through a rotating disk that has three variable slits in it. By controlling the frequency of the disk, and the

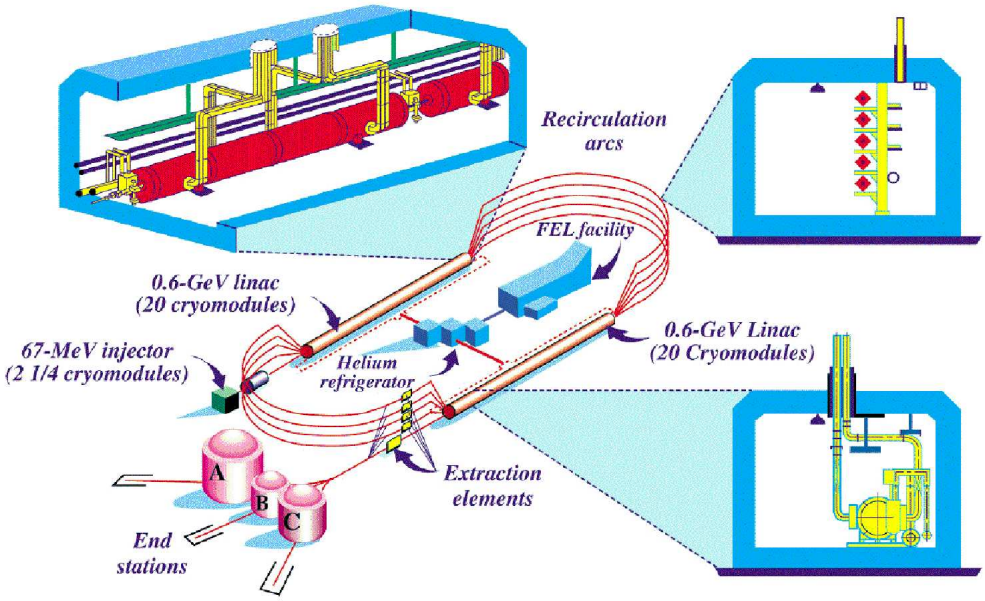

Figure 3.1: The Thomas Jefferson National Accelerator Facility (TJNAF).

slit size, three separate bunches can be produced. This allows each experimental hall to receive a bunch of electrons with a different current and energy than the other halls. The cryomodules are superconducting niobium radio frequency (RF) cavities. As the injected electrons pass through the cavity, the Machine Control Centre (MCC) direct microwaves into the cavity which create a negatively charged area behind the electrons, and a positively charged area in front of them. Both cases give the electrons an energy boost. The microwaves must cycle the positive and negative charged areas in the cavity $\sim$ 1.5 billion times per second to allow the electrons to be boosted in this way for each cavity they enter. Each linear accelerator provides the electrons with an energy boost of $\sim$ 0.6 GeV.

The five recirculation arcs contain magnets that steer the electrons of different energies into the next linear accelerator. At the end of the second linear accelerator, any of the five recirculation arcs can provide each experimental hall with a bunch of electrons at a frequency of 499 MHz. This corresponds to each hall recieving a bunch of electrons every 2.004 ns, which is referred to as a "beam bucket". This is a crucial feature of the beam that is exploited when calibrating the detector, and also in carrying out the particle identification. Fig. 3.12 shows the 2.004 ns beam bucket structure when looking at the timing of the photon tagger relative to the start-counter.

3.3 Hall B

Hall B is the home of the Continuous Electron Beam Accelerator Facility (CEBAF) [45] Large Acceptance Spectrometer, known as CLAS [1]. This is a near 4π detector, containing six super-conducting magnets. The toroidal field is the unique aspect of the detector, providing the means of focusing all particles to obtain the near 4π acceptance. Both electron and photon beam experiments can be run using CLAS. For this experiment the electron beam is used to produce a linearly polarised photon beam using the Hall B coherent bremsstrahlung facility [46]. Fig. 3.2 shows the layout of Hall B, with the beam entering the hall from the bottom right, then passing through the photon tagger, and then proceeding to the target within CLAS. The beam pipe continues to a set of downstream detectors used for photon normalisation, and then to the beam dump.

The CLAS detector is split geometrically into six sectors by the magnets coils, and each of these sectors contain many instrumented layers of detectors. Some of these detectors can been seen in Figs. 3.3 & 3.4. Upstream of the tagger the electron beam was measured by two beam-position monitors (BPMs) during the g8a run. Each of these consists of three RF cavities which provide a beam position coordinate and intensity measurement.

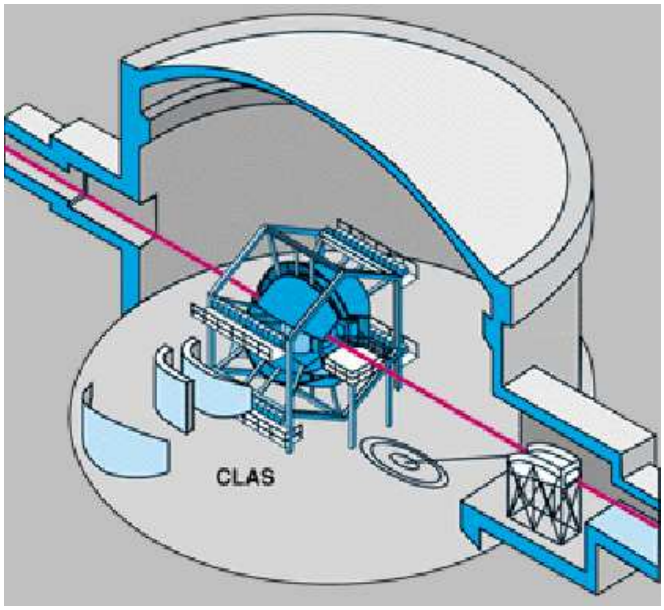

Figure 3.2: Hall B at JLab. The beam passes through the tagger (right lower corner) and then into the CLAS detector.

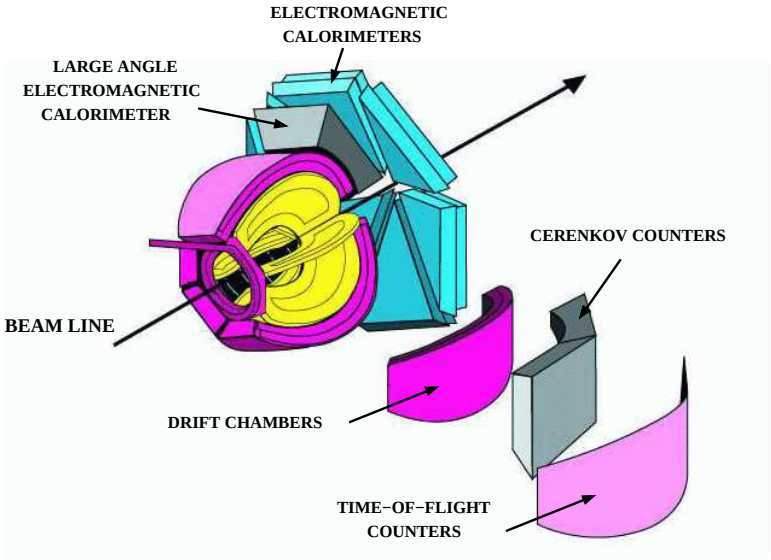

Figure 3.3: The detector regions of CLAS peeled back; DC - drift chambers, CC - Cerenkov counters, EMC - electromagnetic calorimeters, TOF - time-of-flight.

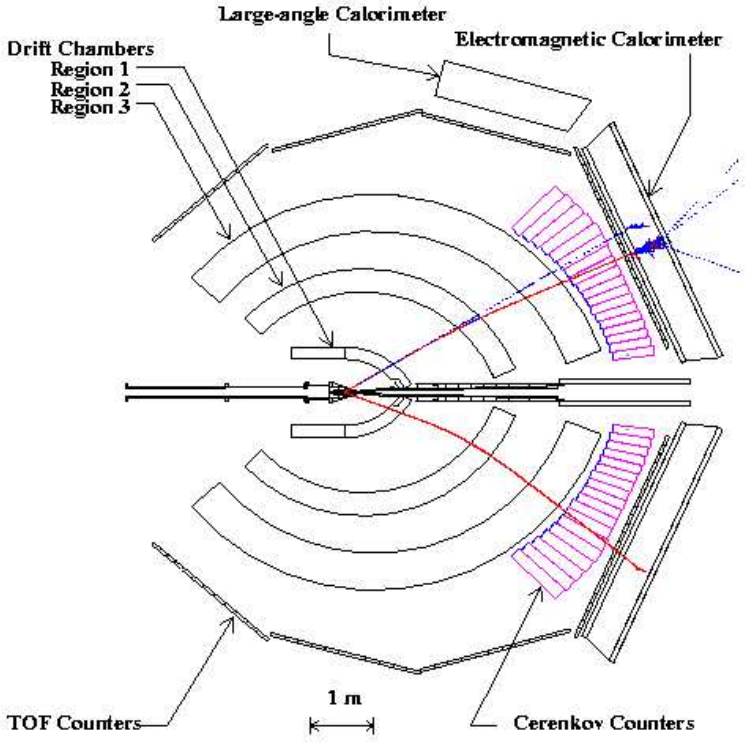

Figure 3.4: A top view of the CLAS detector cut along the beam line. Electron, photon and proton tracks are shown as an example of a hadronic event.

3.4 The Coherent Bremsstrahlung Facility

Linearly polarised photons are produced using the coherent bremsstrahlung technique, where the CEBAF [45] electron beam is incident on a suitably orientated diamond radiator [47]. The bremstrahlung photons are tagged using the Hall B tagging spectrometer [46]. The relative layout of the main components used to produce coherent bremsstrahlung can be seen in Fig. 3.5. The sections below will be used to describe their functions in more detail.

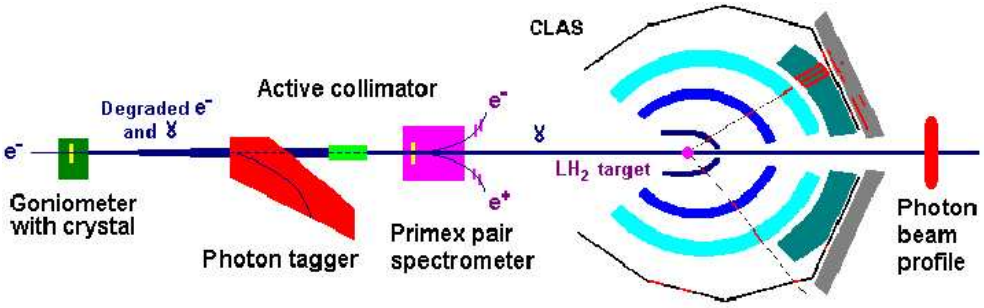

Figure 3.5: The g8a beamline in Hall B of Jefferson Lab (not to scale).

3.4.1 Production of Linearly Polarised Photons

An electron incident on a suitable radiator will be decelerated by the electromagnetic field of the radiator's nuclei, thus emitting an energetic photon. This process is known as bremsstrahlung radiation. If the radiator is a material with no regular crystal lattice structure, such as carbon, then the photon energy spectrum will fall as shown in Fig. 3.6. This is an example of incoherent bremsstrahlung.

However, if a radiator is used that has a regular crystal lattice structure, such as diamond, then this radiator can be aligned to produce coherent bremsstrahlung from a specific set of lattice vectors. This coherent scattering produces a photon with its electric vector oscillating in a particular *plane of polarisation*. The process is analogous to Bragg scattering.

The linearly polarised photons show up in the energy spectrum as a set of discrete coherent peaks, superimposed on an incoherent background. Fig. 3.7 (top) shows an example of such an energy spectrum obtained from simulation using the anb code [48]. Each peak in the energy spectrum corresponds to a different lattice vector. The positions are adjusted by changing the angle between the electron

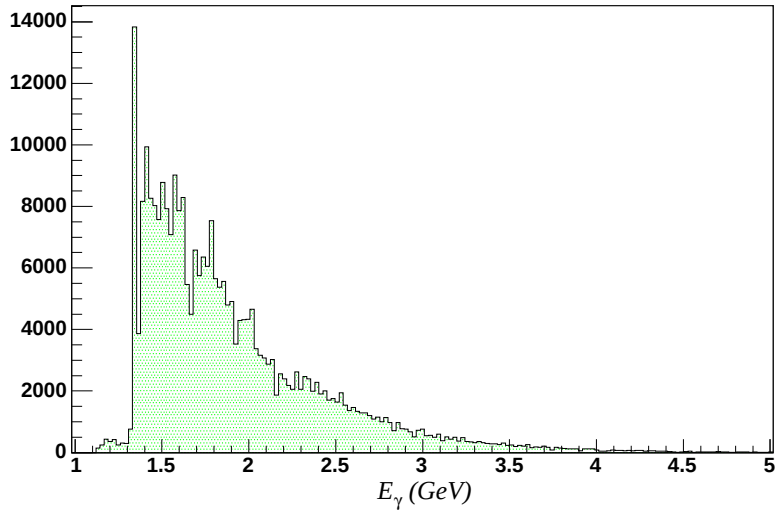

Figure 3.6: The photon energy spectrum for a carbon radiator used in g8a production running. This is an example of incoherent bremsstrahlung. The distribution is not smooth due to varying counter efficiencies.

beam and the crystal lattice. See Appendix A. for a more formal description of coherent bremsstrahlung.

3.4.2 The Goniometer

The GWU goniometer [49] was used for the g8a run. This device is used to control the angle between the electron beam and the crystal lattice of a diamond radiator, and is shown in a test environment in Fig. 3.8. The goniometer is used to measure 1) the angular offsets between the crystal axes and the goniometer axes and 2) the zero offsets between the goniometer and the electron beam axis. This allows six degrees of freedom that define the radiator position and orientation, which are given in Table 3.1. Radiators with a non-crystalline structure can also be orientated by the goniometer, relative to the CLAS detector.

3.4.3 Diamond and Other Radiators

The selection of suitable diamond radiators for production of coherent bremsstrah -lung [50] was carried out prior to the g8a run. During this process a crystal must pass three tests before it will be used in experimental running. The first involves illuminating the crystal from below with polarised light, and viewing it from

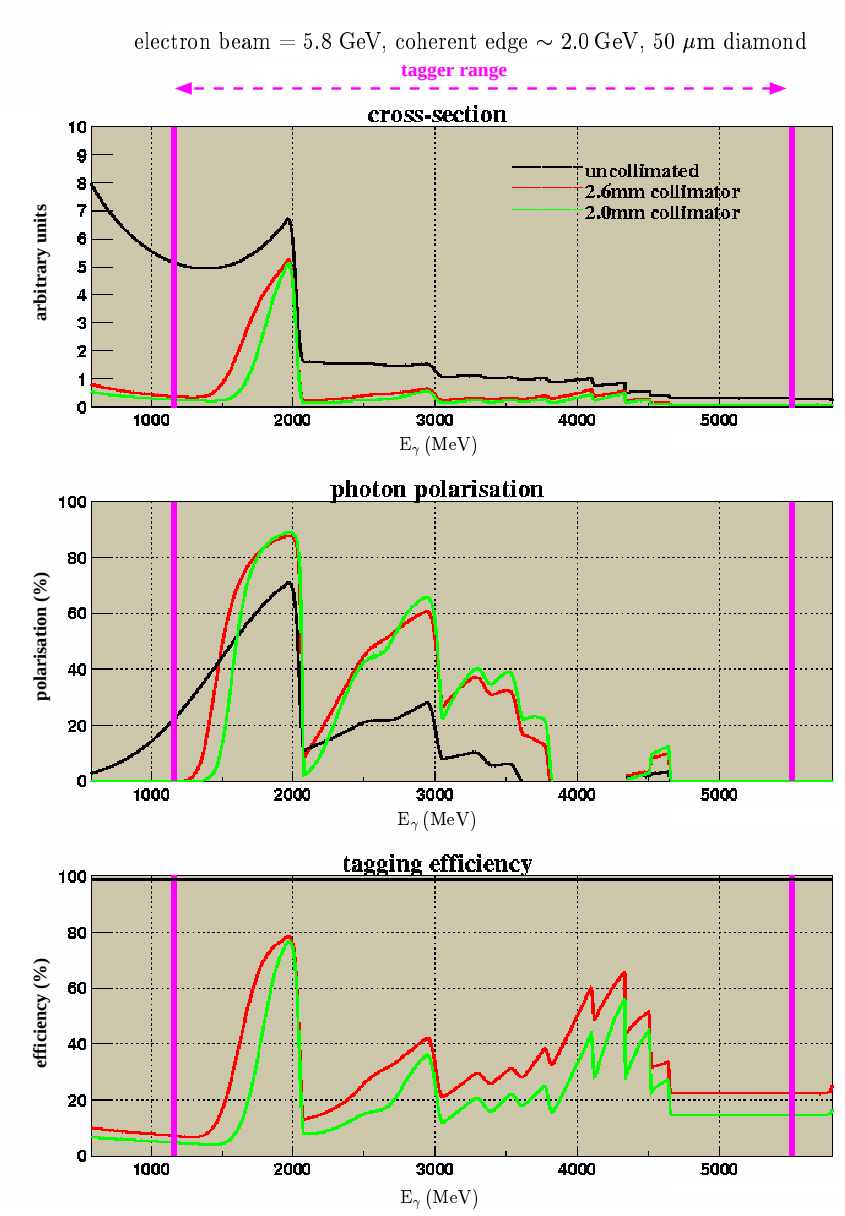

Figure 3.7: Simulation of coherent bremsstrahlung from a 50 μm thick diamond radiator with an incident 5.8 GeV electron beam using the anb code [48]. From top to bottom the effects of collimation on the cross-section, the degree of linear polarisation of the photons, and the tagging efficiency are represented by the different coloured lines.

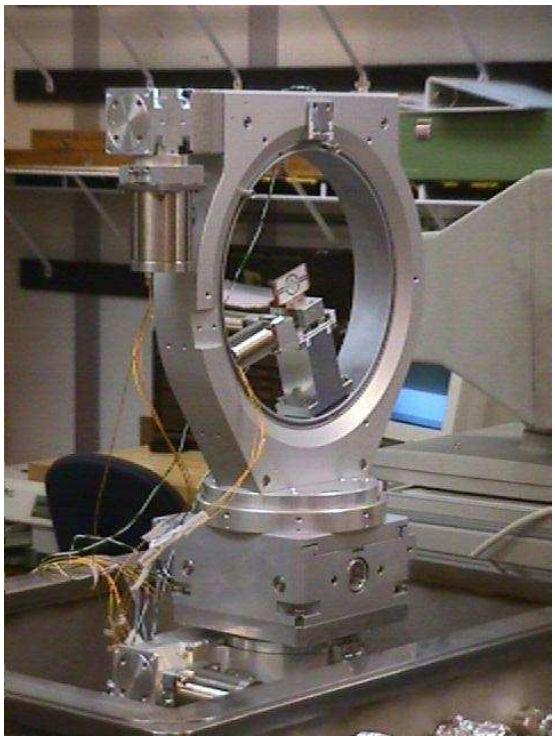

Figure 3.8: The GWU goniometer [49] in a test environment. A prototype radiator ladder can be seen in the centre of the goniometer.

Degree of freedom	**Description**	**Measured accuracy**
Coarse translation	Allows for horizontal translation of the device into the beam position	$\pm 35\,\mu$m
Fine translation	Allowing for fine translation houses the target ladder	$\pm 25\,\mu$m
Vertical translation	Allows for adjustment of the position vertically	$\pm 180\,\mu$m
Pitch	A circle segment allowing the crystal to be inclined wrt the beam axis	$\pm 0.006°$
Yaw	Allows the crystal to be rotated around the vertical axis	$\pm 0.004°$
Roll	An eulerian cradle allows for rotation of the crystal vertically around the beam axis	$\pm 0.008°$

Table 3.1: The specifications of the GWU goniometer [49].

above through another polaroid which is crossed perpendicular to the polaroid below. This allows only areas where local birefringence in the crystal caused by strain fields associated with defects to be seen. An example of this can be seen in Fig. 3.9. Apart from growth horizons and dust on its surface, this 20 μm diamond is without feature.

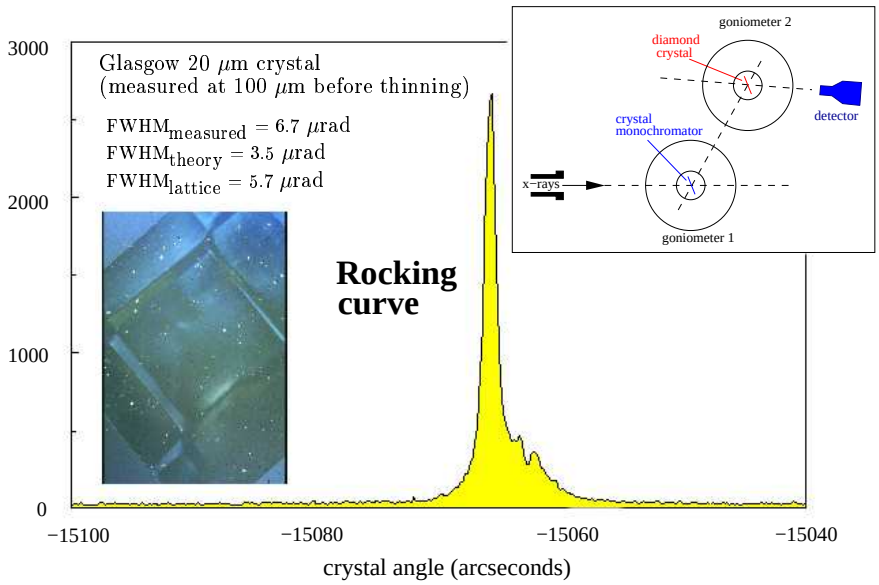

Figure 3.9: An example of a rocking curve measurement for a 20 μm thick diamond. The narrow width is a desirable characteristic of a radiator to be used in the production of coherent bremsstrahlung. On the left is a polarised light analysis of the crystal, showing only growth horizons and some dust on its surface. Upper right is a representation of the experimental set-up to carry out a rocking curve measurement.

The second and third tests allow the defects to be studied with greater resolution with the use of X-rays. The first of these is X-ray topography [51], in which an image of the crystal is obtained using a reflected parallel beam of X-rays. Contrast in the image is due to the presence of defects, which cause variation in the lattice parameters of the crystal. The final test is to measure the rocking curve [51, 52] of the crystal. This is a plot of the intensity of the reflected X-rays against the range of angles over which reflection occurs for a given set of crystal planes. Fig. 3.9 shows an example of this measurement.

For the production of coherent bremsstrahlung, a diamond with a suitably narrow rocking curve is preferable to achieve photons with a high degree of linear polarisation. Once such a diamond is found, it is ideal to reduce the thickness of the crystal so that the electron multiple scattering angle is approximately the

same as the bremsstrahlung characteristic angle [50]. This condition will provide the highest possible degree of linear polarisation from this process. For a 6 GeV electron beam, this corresponds to a diamond thickness of around 20 μm. Such a diamond was available for the g8a run, although suspected problems with the mounting of the crystal on the radiator ladder resulted in the data acquired during this period to be of inferior quality. As a result of this a 50 μm thick diamond was mainly used during the g8a experiment, with the disadvantage of this being the lesser degree of linear polarisation obtained.

An amorphous carbon radiator was also used. This provided complementary data that is used in calculation of the photon polarisation, and also to understand the azimuthal acceptances of particles detected in CLAS. A screen radiator was also used to observe with the naked eye the position of the electron beam when preparing for data acquisition. All radiators were mounted on the same radiator ladder, which is represented in Fig. 3.10. The radiator properties are given in Table 3.2.

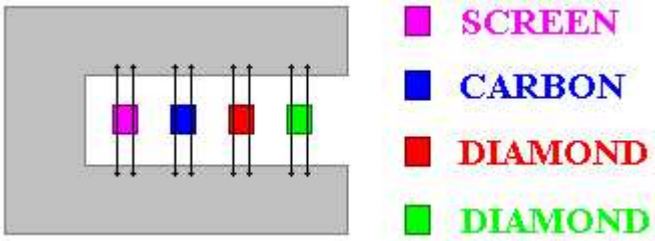

Figure 3.10: A representation of the radiator ladder used during the g8a experiment.

Mounted radiator	**Thickness**
Screen (ZnS)	20 μm
Carbon	50 μm
Diamond	20 μm
Diamond	50 μm

Table 3.2: The mounted radiators used during the g8a experiment.

3.4.4 The Photon Tagger

The photon tagger used in Hall B has a broad tagging range of 20-95% of the incident electron beam energy. The scattered electron and bremsstrahlung photon

enter the tagger, and the electron is then acted upon by a uniform field dipole. As the photon has no electric charge, it passes straight through the magnetic yoke as shown in Fig. 3.11. This homogeneous dipole field focuses the energy degraded electrons onto the flat focal plane hodoscope, which consists of two separate planes of scintillator detectors. Full energy electrons are directed to the tagger beam dump.

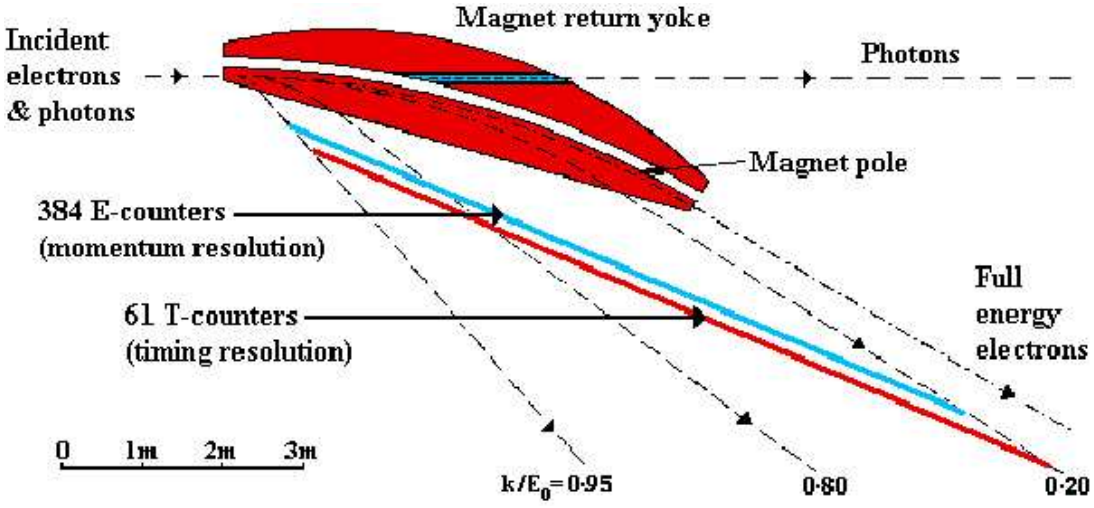

Figure 3.11: A schematic of the tagger, showing the relative positions of the scintillator hodoscope (E & T counters), magnet, and electron and photon paths. k is the photon energy, E_0 is the incident electron beam energy.

There are 384 scintillators in the first plane, which is known as the energy plane (E-plane). These are 20 cm long and 4 mm thick, with varying widths of 6-18 mm to provide roughly constant momentum bins of 0.003 x E_0. These scintillators are partially overlapped to provide 767 channels. The signals are read out using optical fibres and photomultiplier tubes (PMTs), and a time is obtained from a time-to-digital converter (TDC) with a resolution of 500 ps/ch. The E counters are also equipped with scaler units to count hits throughout the tagger.

The second plane is known as the timing plane (T-plane), and lies 20 cm downstream of the E-plane. There are 61 scintillators in this plane, each of which is 2 cm thick. The signals are read out from both sides (transverse to the momentum axis) using fixed light guides, PMTs, TDCs with a resolution of 50 ps/ch, and also counted using scalers. Overlapping allows 121 channels whose timing is compared to the machine RF time, which is then used to establish

the electron beam bucket that the bremstrahlung photon was produced from. Fig. 3.12 shows a clear peak which contains the real photons which produced the hadronic event in CLAS. The T counters also have a multi-hit TDC (500 ps/ch) readout to assist in normalisation calculations.

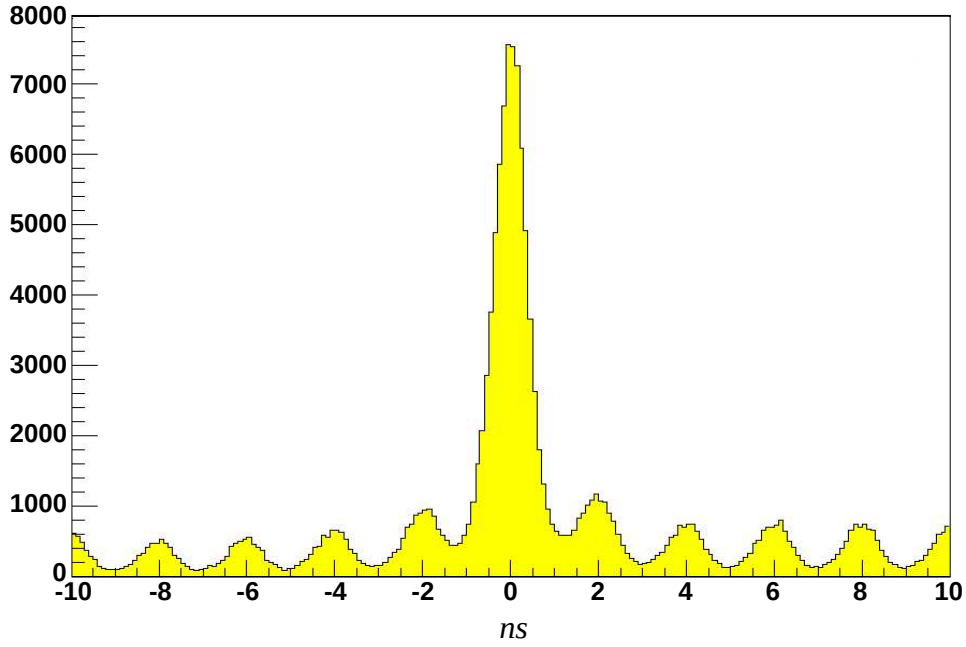

Figure 3.12: Tagger time (effectively the RF time, see Chapter 4.4) minus start-counter time for highly relativistic pions are identified by $\frac{dE}{dx}$ in the time-of-flight paddles. The peak contains the photons producing the hadronic event in CLAS and the 2 ns beam bucket structure can be seen.

The E-T coincidence logic associates groups of E-counters with a T-counter from geometric considerations. This is done to exclude events not originating from the radiator. The signature of any event is set with times from both the E and T planes, and recorded on receiving a valid tagger/CLAS event trigger. This arrangement allows a rate of polarised photons on target of the order of $5 \times 10^6\,\mathrm{s}^{-1}$.

3.4.5 The Active Collimator

Downstream of the tagger the photons encounter the UTEP/Orsay active collimator [53]. This device is made up of 13 diskettes, each with an outer diameter of 50 mm, a thickness of 15 mm, and a small aperture bored in the centre of each.

The first three diskettes are made of an alloy of tungsten, while the remaining ten are made of nickel. This choice is to satisfy the competing needs of highly attenuating the photon beam with the tungsten, reabsorbing the photoproduced neutrons from the tungsten in the nickel, and maintaining a manageable collimator length. Fig. 3.13 shows a picture of the collimator.

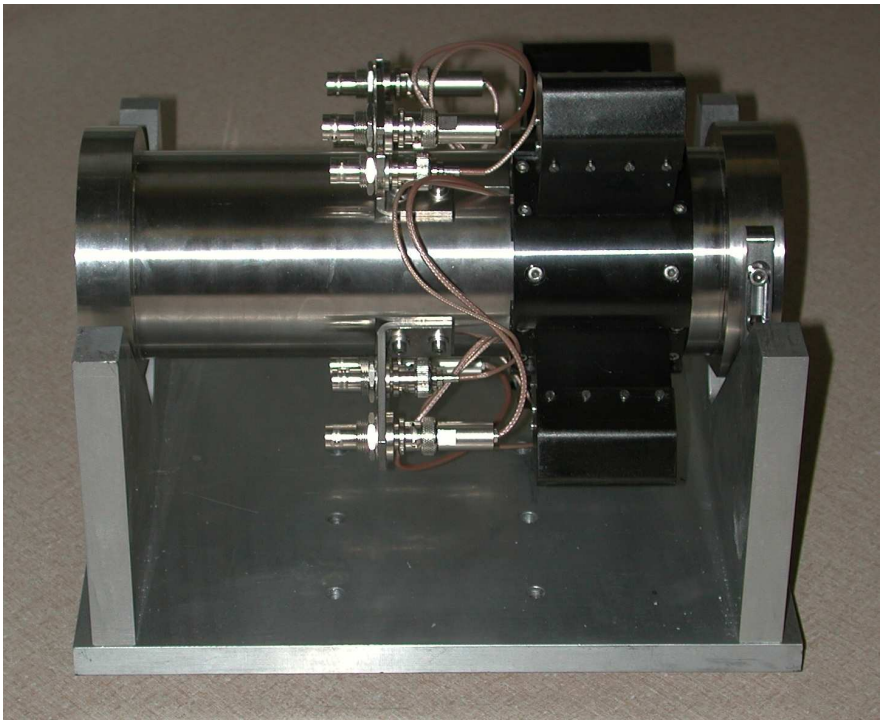

Figure 3.13: The UTEP/Orsay active collimator [53].

The function of the collimator is to reduce the incoherent background of the photon spectrum, serving to increase the degree of polarisation, and to avoid contamination from the tail of the second coherent peak. High polarisation in tandem with high count rates can be achieved by collimating the beam to roughly half a characteristic angle, θ_γ. For the g8a run the goniometer-collimator distance was 22.9 m, therefore the aperture of the collimator should be approximately 2 mm for an incident electron energy of 5.7 GeV. The collimator contains four radially mounted scintillators, lightguides, and photomultiplier elements possessing a left-right, up-down symmetry. These are situated between the first and second tungsten plates allowing us to view the shape of the photon beam downstream of the tagger, and also providing further monitoring of the beam stability.

The effect of collimating the photon beam can be seen from the simulation of a 50 μm thick diamond in Fig. 3.7. The simulation is based on the anb code [48].

Fig. 3.7 shows some predicted properties from this simulation. From top to bottom, these are the cross-section versus photon energy, the degree of linear polarisation versus photon energy, and the tagging efficiency versus photon energy for an uncollimated beam (black), a 2.6 mm aperture (red), a 2.0 mm aperture (green). The contributions to coherent scattering off a particular lattice vector can be seen in the discrete peak behaviour as photon energy increases.

An example of normalised photon spectra before and after collimation for g8a data are shown in Fig. 3.14. Here, *normalised* means that the spectrum obtained with the diamond radiator is divided by the reference spectrum from the amorphous carbon radiator, this method is discussed in more detail in Chapter 2.5. Both data sets are fitted with the anb code [48]. It can be seen that there is good agreement between the data and fits, and that a maximum degree of polarisation of 84% is achieved for the selected period of data.

3.5 The Target

For the g8a experimental run the target cell [54] was a cylinder of 180 mm in length, and a 14mm radius. The cell walls were 170 μm thick Mylar. The cell was filled with liquid hydrogen and cooled to $\sim$ 1 K. The target cell for g8a was positioned at the centre of CLAS, although the ability to move it along the beamline axis does exist to enable the maximisation of the acceptance for a particular channel. Fig. 3.15 shows a photograph of the g8a target cell.

3.6 The CLAS Detector

3.6.1 The Toroidal Magnet

The magnetic field in CLAS is produced by six super conducting coils. These are mounted around the beamline in such a way that six sectors of $\sim 60^{\circ}$ are created. Figs. 3.16 and 3.18 represent the geometric positions of the coils relative to the beamline. The diameter and length of the magnet are both approximately 5 m. The magnetic field is always transverse to the particle's momentum, and does not appreciably affect the azimuthal component of the the particle's momentum. The maximum field during operation is $\sim$ 2 T. For the g8a run period the main torus was set to positive polarity to bend positively charged particles away from the beamline.

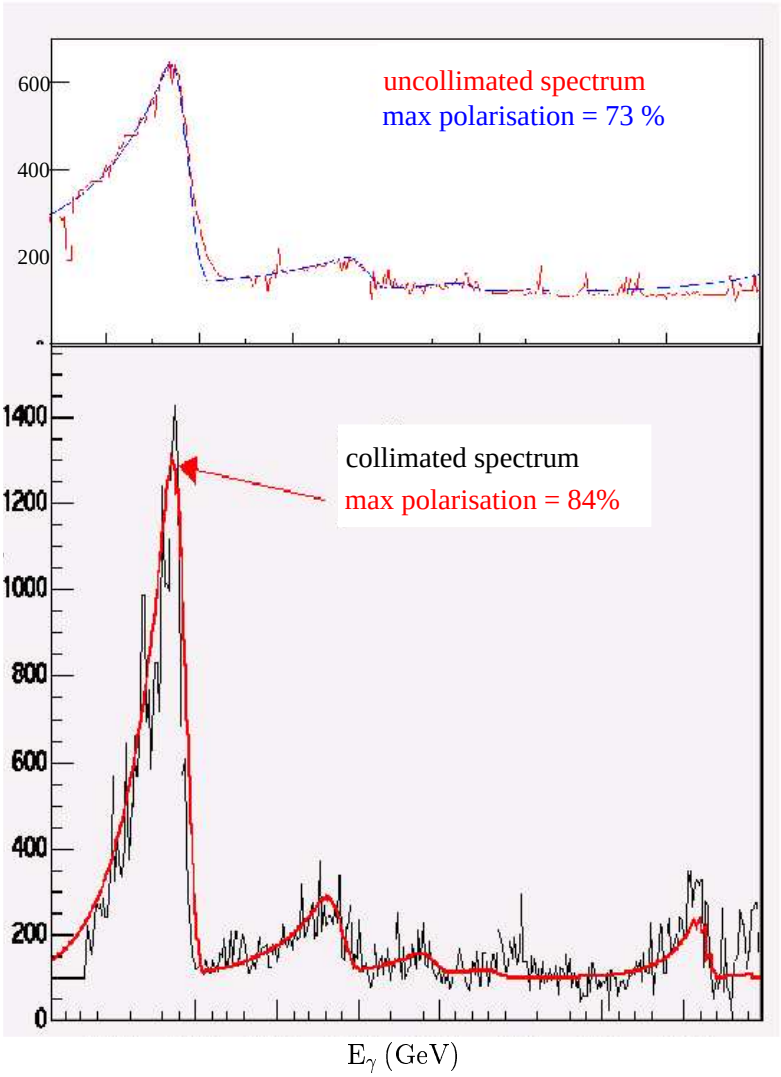

Figure 3.14: Normalised spectra before and after collimation. The enhancement of the spectral peaks are due to the collimation of the photon beam. Both fits are obtained from the anb code [48].

Figure 3.15: The g8a target cell.

Surrounding the target there is a small conducting mini-torus which can be seen in Fig. 3.18. This is used only during electron running to prevent low momentum Mϕller electrons from reaching the region 1 drift chambers. For photon running the mini-torus is replaced by the start-counter. Further information on both the main torus and the mini-torus can be obtained from Refs. [1, 55].

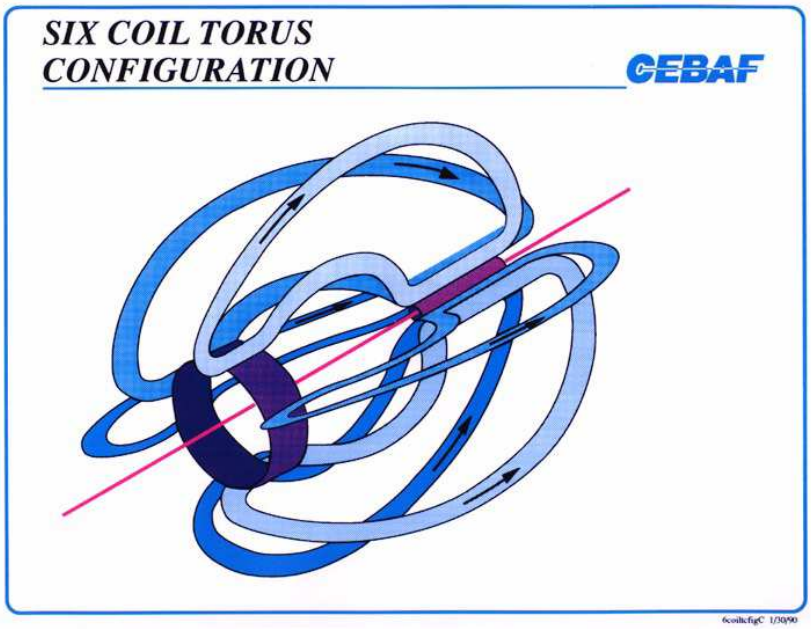

Figure 3.16: The coils of the CLAS magnet.

3.6.2 The Start Counter

For photon running in CLAS the mini-torus is replaced by a detector called the start counter [56]. It is used to obtain the correct start time for time-of-flight measurements. It does this by identifying the correct electron beam bucket that produced the bremsstrahlung photon causing the hadronic event in CLAS. This information coupled with tracking the particles through the drift chambers to the time-of-flight paddles allows particle identification to be carried out.

The start counter consists of three 3 mm thick coupled-paddle plastic scintillators. Each coupled-paddle covers two sectors of CLAS. Any type of ionising radiation will be detected in the scintillators. The signal is read out at both ends of the coupled-paddle with a solid light guide and photomultiplier tube (PMT). Each channel also has an analogue-to-digital converter (ADC) and a time-to-digital converter (TDC) for energy and timing information.

The scintillators are each bent in three places to construct a hexagonal tube and cone (leg and nose). Fig. 3.17 shows one half of a coupled-paddle surrounding the target cell. Each leg has a PMT attached, giving six channels corresponding to the six sectors of CLAS. A software corrected time resolution of 260 ps can be obtained, and the detector can operate comfortably up to rates of $\sim$ 1.2 MHz. The angular coverage of the detector relative to each sector is approximately equal to that of the time-of-flight system; $7^\circ < \theta < 145^\circ$, $-29^\circ < \phi < 29^\circ$, where θ (ϕ) is the polar (azimuthal) angle relative to the beam direction.

3.6.3 The Drift Chambers

Charged particles in CLAS are detected in three regions of drift chambers [57], from which their momenta can be measured. These are positioned within the space between the torus coils, as shown in Fig. 3.18. Each region has six chambers covering a single sector of CLAS, leading to a total of eighteen chambers. In each chamber there are two superlayers, the axial layer, and the stereo layer. The axial layer is axial to the magnetic field, and the stereo layer is oriented at a 6° angle to this to give azimuthal information. Each superlayer contains six layers of hexagonal drift cells, except the stereo superlayer of region 1, which has only four layers due to spacial constraints. The cells are constructed to produce six field wires around a single sense wire in a repeating hexagonal pattern. There are 35,148 sense wires in the drift chamber system, with resolution of each cell varying from $\sim$310-380 μm.

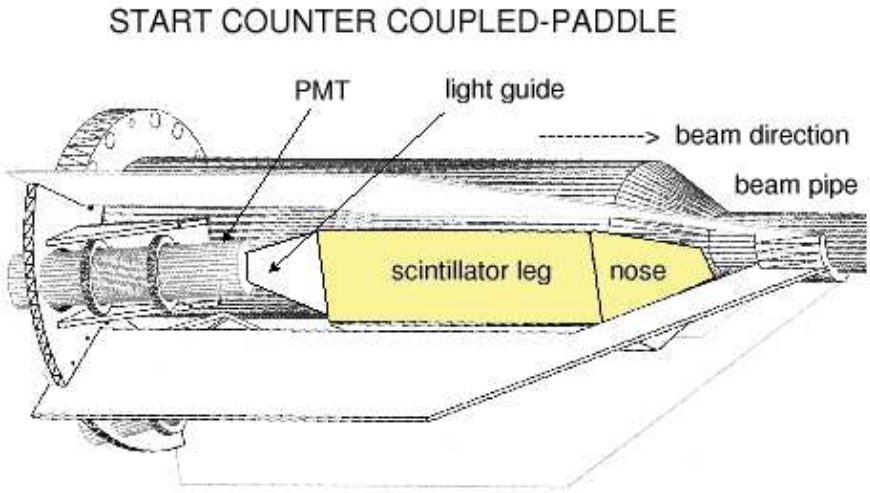

Figure 3.17: One half of a coupled-paddle scintillator. Six of these make for a hexagonal surrounding of the target cell, and provide the start time for the time-of-flight measurement.

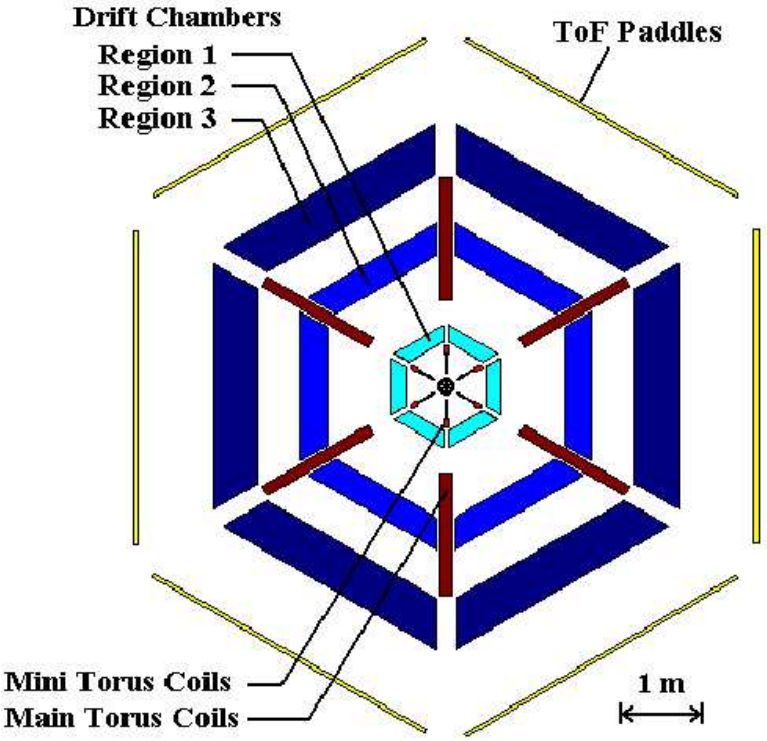

Figure 3.18: The CLAS detector perpendicular to the beamline.

The chambers are all filled with the same gas mixture of 90% argon - 10% carbon dioxide. A high voltage is applied to the field wires. A charged particle entering a chamber will ionise the gas molecules, with the liberated electrons then drifting to the sense wire. The drift time for the electrons to arrive on the sense wire is then measured to determine the drift distance of the particle to the sense wire. The particle's trajectory can then be tracked using this method throughout all three regions. In Fig. 3.19 a representation of a particle track through the two superlayers of region 3 is given.

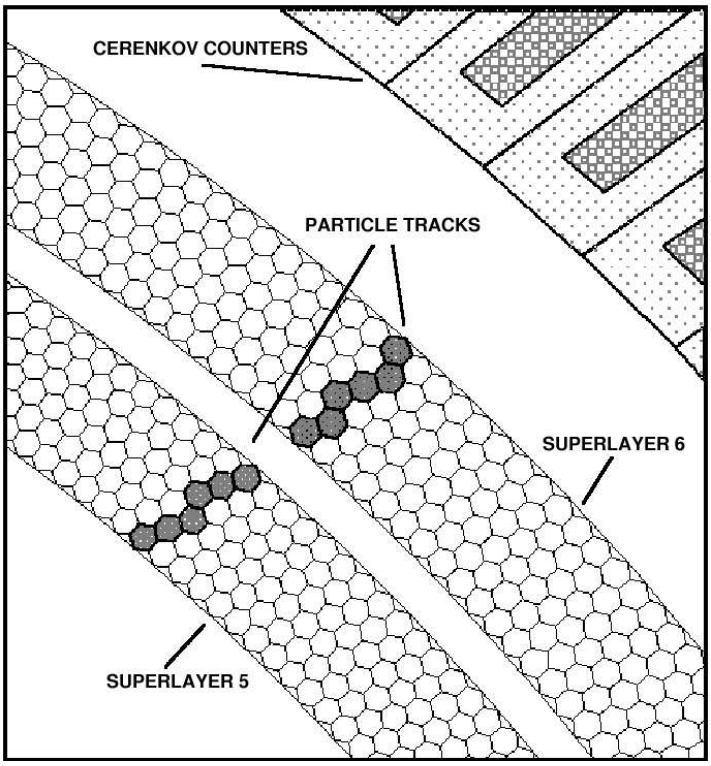

Figure 3.19: A particle passing through the two superlayers of region 3 of the drift chamber system.

The first region is closest to the target, lying within the (nearly) field free region inside the torus bore. It is used to determine the initial direction of charged particle tracks. The second region lies between the torus coils, in the region of strong toroidal magnetic field. It is used to obtain a second measurement of the particle track at a point where the curvature is maximal, to achieve good momentum resolution. The third region is located outside the torus coils, once more in a region with low magnetic field.

3.6.4 Cerenkov Counters

The Cerenkov counters [58] in the CLAS detector are only present at forward angles. As mentioned previously, this detector is used only during electron running. It is part of the trigger during electron running, and is also used to separate electrons from pions. When a charged particle enters one of the perfluorobutane filled Cerenkov counters, and is travelling faster than the speed of light in the gas, the particle will emit a cone of Cerenkov light. The opening angle of the cone depends on the velocity of the particle creating the light.

3.6.5 Time-of-Flight Scintillators

The time-of-flight [59] system for CLAS consists of 57 plastic scintillator paddles per sector, covering a total area of 206 m^2. All of the scintillators have a thickness of 5.08 cm, but they vary in both length and width depending on which lab angle an individual paddle may cover. The lengths vary from 32.3 cm at the lowest nominal lab angle of 8.6°, to 445.1 cm at a nominal lab angle of 75.7°, and back down to 212.7 cm at a nominal lab angle of 141.0°. For forward angles a width of 15 cm was chosen after considering spacial constraints, for the large-angles a larger width of 22 cm was chosen, except for the last four which are again 15 cm. The last 18 paddles in each sector are paired into nine logical counters, which gives a total of 48 channels per sector. Fig. 3.20 shows the four panels of the time-of-flight scintillators for a single sector.

For each of the forty eight channels, at both ends of each scintillator bar the pulse height of any analogue signal is read out by an ADC, and digitised timing information is read out by a TDC. This information is used to determine the mass of the particle travelling through CLAS. This is done using the momentum measurement from the drift chambers, and the particle's velocity which is obtained from the flight time of the particle from the target to the ToF bars. The intrinsic time resolution for the short (long) counters is $\sigma \sim 80$ ps ($\sigma \sim 350$ ps). For pions from electroproduction the time resolution for the short (long) counters has been measured to be $\sigma \sim 150$ ps ($\sigma \sim 350$ ps).

3.6.6 Electromagnetic Calorimeters

For each sector of CLAS there exists an electromagnetic calorimeter [60] which covers the laboratory angular range of $8° < \theta < 45°$. The electromagnetic

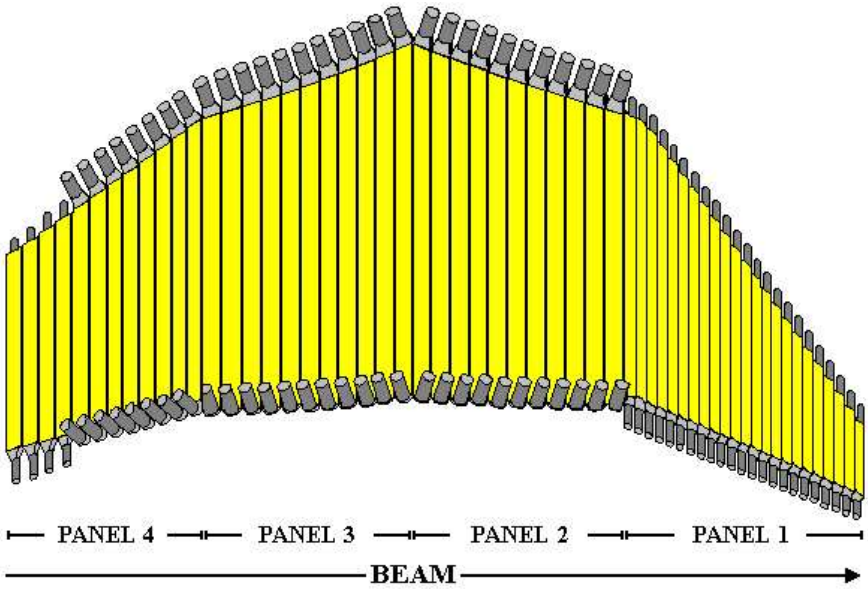

Figure 3.20: The four panels of scintillators in each sector of the CLAS ToF system.

calorimeter consists of 39 layers, with each layer consisting of a 10 mm thick scintillator, and a 2.2 mm thick lead sheet. This lead-scintillator sandwich is in the shape of an equilateral triangle to match the hexagonal geometry of CLAS. The scintillator layer is made up of thirty-six strips parallel to one side of the triangle, and for each successive scintillator layer the orientation of the strips is rotated by 120°. This provides three possible orientations, labeled u, v, and w, which provide stereo information on the location of the energy deposition, see Fig. 3.21. There are thirteen layers of each possible orientation. For each of the three possible views, the first five layers make up what is known as the "inner" stack, and the remaining eight the "outer" stack. This is done to provide longitudinal sampling of the shower.

The electromagnetic calorimeter is capable of detecting electrons at energies above 0.5 GeV, photons above 0.2 GeV, and also the detection of neutrons. These particles will lose energy in the lead sandwich by typically radiating a photon after a single radiation length in the material. A shower of energy is created by the layers of lead, and the radiated energy is detected by the scintillators.

For sectors 1 and 2 only, there exists a large angle calorimeter, which provides coverage between the lab angles $45° < \theta < 70°$. These calorimeters consist of 33 layers, each layer being made up of 1.5 cm thick plastic scintillator strips

and 2 mm thick lead. Each layer is at right angles to the pervious layer. The method of detection is based on the same principals as described above for the electromagnetic calorimeter.

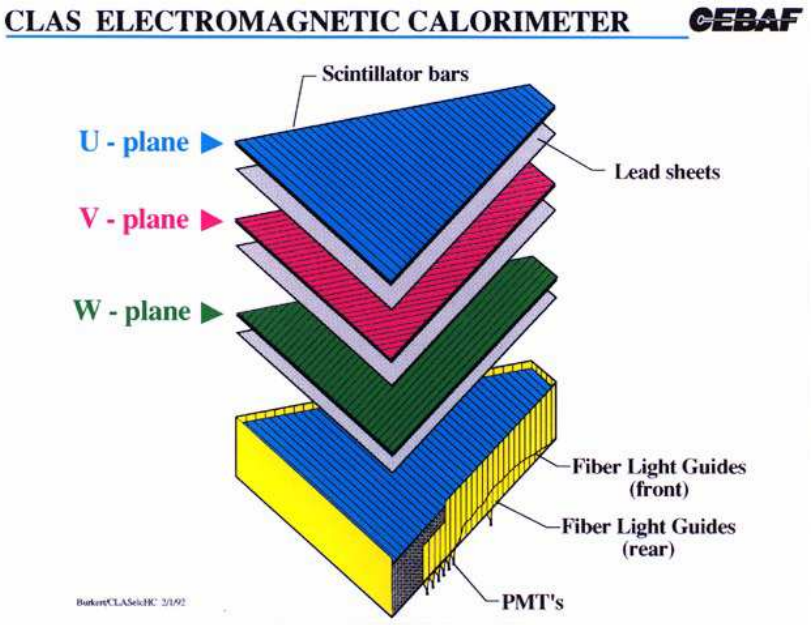

Figure 3.21: The three possible orientations of each scintillator in successive scintillator-lead sandwiches.

3.7 Downstream Devices

There are three detectors downstream of CLAS whose purpose is to measure the photon flux normalisation [46]. The detectors are called the Pair Spectrometer, Pair Counter, and the Total Absorption Shower Counter. Fig. 3.22 shows the layout of these detectors, and a full description of these are given in Ref. [46].

When a photon interacts with the thin converter at the front end of the pair spectrometer, e^+e^- pairs are produced which then travel through the magnetic field produced by the dipole magnet. These are detected in eight scintillators around the beamline, providing rough energy information on the photon beam. The pair counter is a backup device to monitor the full beam intensity. This detector has a veto converter to eliminate charged background from CLAS, a thin converter that produces e^+e^- pairs, and a single scintillator paddle with four slightly overlapping scintillators behind it. The total absorption counter consists of four bars of lead glass which are used as the primary method of measuring

the photon flux. The total absorption counter has an efficiency of nearly 100% at rates of $\sim 10^5$ tagged photons/s , which is too low for linear polarised photon beam running conditions where the rate is $\sim 10^6$ tagged photons/s. This detector is therefore only used for low intensity normalisation runs, and is removed during normal running.

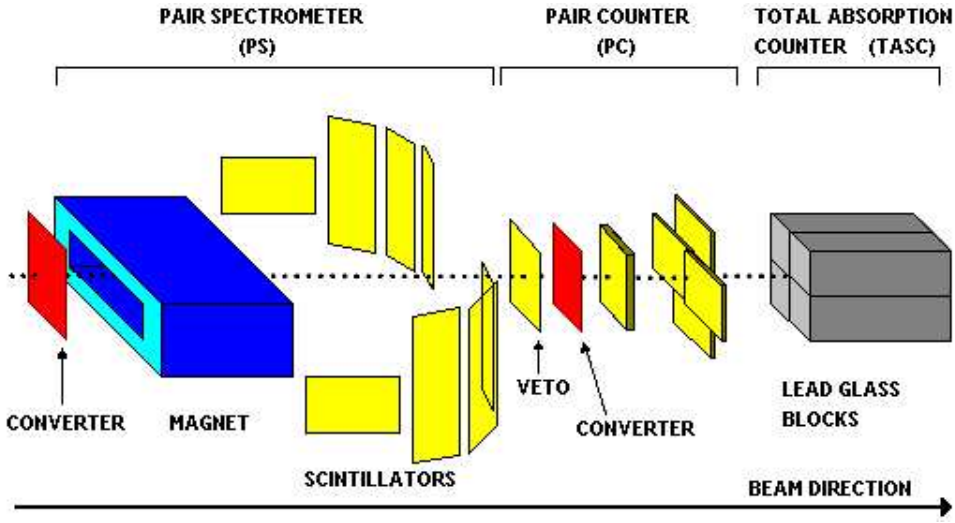

Figure 3.22: The Pair Spectrometer, Pair Counter, and the Total Absorption Shower Counter.

3.8 Trigger System

To obtain only events of interest while minimizing the detector deadtime, a dual level trigger system is employed for experiments in CLAS. The level 1 trigger processes only prompt PMT signals through a memory lookup table. The level 2 trigger looks for possible tracks in the detector, and issues the signal to end the current trigger. For the g8a experiment, our physics trigger required at least one positive charged particle to be detected.

3.8.1 Level 1 Trigger

The level 1 trigger [61] for the g8a run was formed by a coincidence of signals from the tagger master-OR (MOR), the start-counter, and the time-of-flight scintillator paddles. For each of the 61 T-counters in the photon tagger, a coincidence between the left and right PMTs and a possible matching E-counter are OR'ed

together, as shown in Fig. 3.23. There is also the option to prescale sections of the tagger, but this was not used for g8a. The signals from each side of a start-counter paddle are summed using a linear fan-in/out, and the signal is then passed into a discriminator. Logic signals from each pair are then OR'ed together to provide a signal for the start-counter trigger, as shown in Fig. 3.24. The tagger MOR and start-counter signals are plugged into a set of CAMAC units for two reasons: 1) To regenerate the degraded signals; 2) To be able to control the width of the logic pulses. The MOR width was set to 10 ns, and the start-counter width was set to 15 ns. For the time-of-flight trigger, each paddle's signals are first sent to a pre-trigger board. Paddles 1-16 and 17-48 for each sector have their own pre-trigger board, and each board sends an individual signal to the level 1 trigger. The width of the signals for the time-of-flight trigger was set to be 120 ns, and Fig. 3.25 shows the logic.

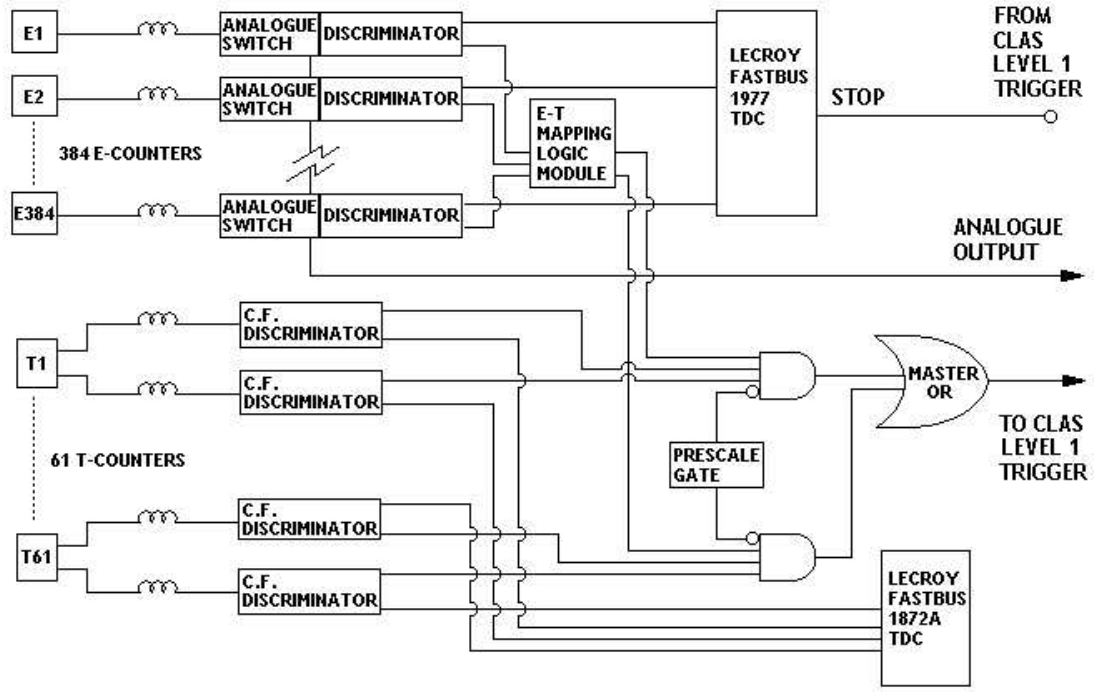

Figure 3.23: The tagger master-OR logic for level 1 trigger.

The signals from the time-of-flight pre-trigger boards provide inputs to the level 1 trigger. The level 1 hardware then compares the input pattern to a set of memory look-up tables. The memory lookup process has three stages. The first is to map the pre-trigger signals into four intermediate bits per sector. The second stage is to check combinations of these intermediate bits, called "sector events".

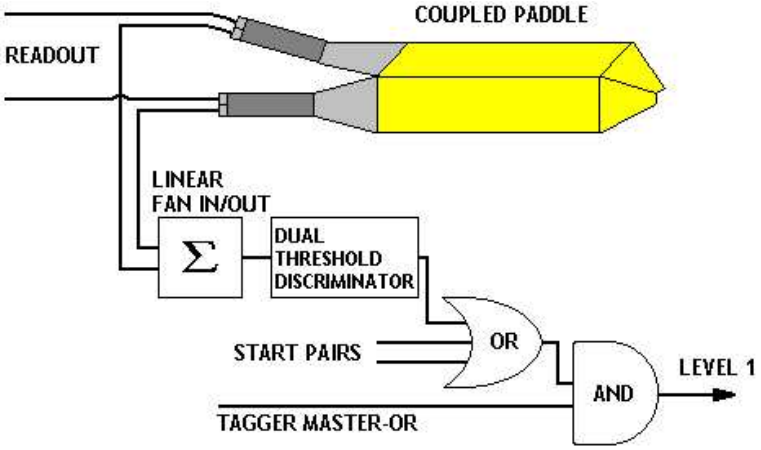

Figure 3.24: The start-counter logic for level 1 trigger.

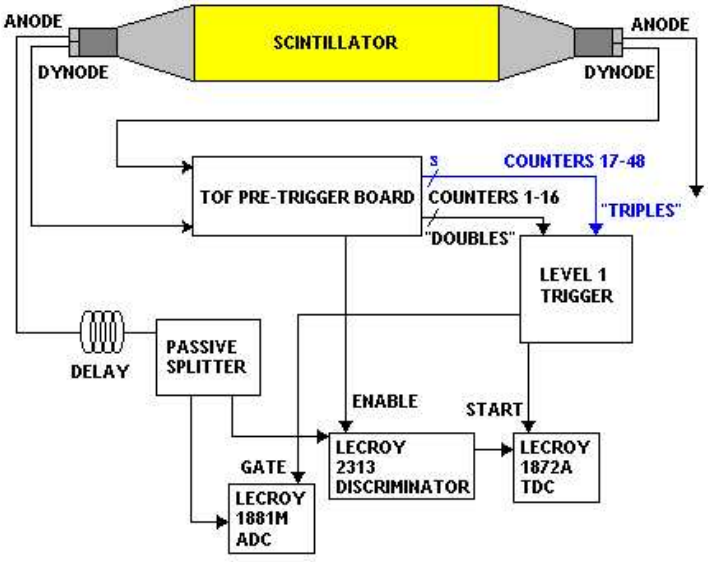

Figure 3.25: The time-of-flight logic for level 1 trigger.

The final stage is to correlate these sector events to apply geometrical constraints on multi-pronged events. It is at this third stage when the MOR-start-counter coincidence signal enters the level 1 trigger. The level 1 trigger signal is then passed to the trigger supervisor which is discussed in Chapter 3.8.3. A summary of the main features of the level 1 trigger is shown in Fig. 3.26.

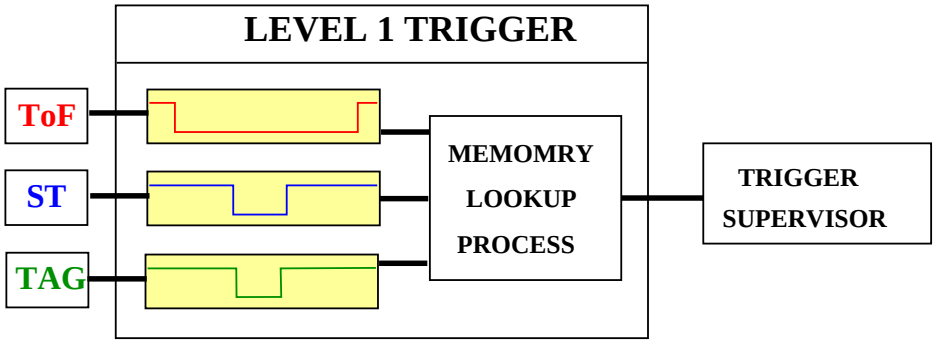

Figure 3.26: A summary of the main features of the level 1 trigger used in the g8a experiment.

3.8.2 Level 2 Trigger

The level 2 trigger is used to reject events with a level 1 trigger, but with no *likely tracks* detected in the drift chamber system. Such an event could be due to cosmic rays passing through CLAS. A likely track is one in which track segments in three superlayers of the drift chambers match some initial template. The level 2 trigger is satisfied with a logic OR for all six sector tracks, or if no track is matched for any sector, a *level 2 fail* signal rejects the event.

3.8.3 Trigger Supervisor

The trigger supervisor is the electronics board that recieves the level 1 and level 2 inputs. This board administers all common signals, busy gates, resets for detector electronics, and also the data readout. It is possible to program the trigger supervisor to require only a level 1 input, or to require both level 1 and level 2 inputs.

3.8.4 Data Acquisition

A diagram of the standard data acquisition system for CLAS data is shown in Fig. 3.27. FASTBUS crates read out data words for all detector analogue-to-digital converters and time-to-digital converters. If the required level of trigger is satisfied, these data words are converted into BOS [62, 63] format at the front end, and then transported via a fast ethernet connection to a Sun workstation. Each event is built in the BOS format, and then recorded to a RAID array of hard drives. An average event is typically $\sim$ 4 kbytes when in the raw data format. A fibre connection then transfers the data to the JLab computer center, where the data is stored on a tape silo. For g8a the event rate was typically $\sim$ 2.5 kHz. Allowing for beam trips and other downtime during experimental running $\sim$ 700 Gbytes of raw data were written to tape silo per day.

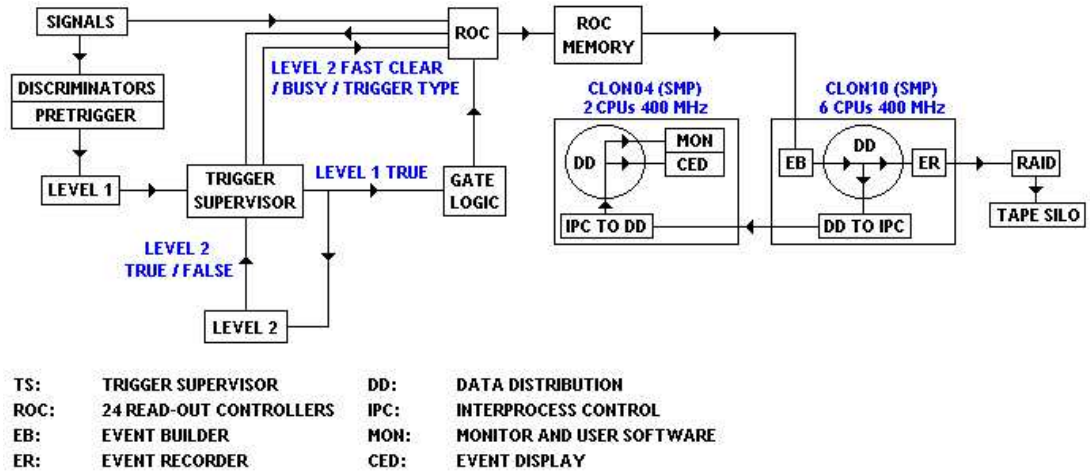

Figure 3.27: The data acquisition flow for CLAS.

3.9 Summary

The CLAS detector and the coherent bremsstrahlung facility have been described in this chapter along with a brief description of how the data is acquired and stored. The following chapter will describe how this data is prepared for physics analysis. To reach this stage the detector systems must go through a cycle of calibrations and data processing. Chapter 4 is a description on how to progress through this cycle.

Chapter 4

Calibration and Event Reconstruction

4.1 Introduction

The resolution of the coherent bremsstrahlung tagging system and the CLAS detectors are governed by the quality of their calibration. Several reference runs are used to obtain the appropriate calibration constants for each system. A *reference run* is one which is representative of a range of runs which had similar conditions during data acquisition. Each detector in CLAS has a dedicated software package to convert raw signals in its ADCs and TDCs to more meaningful information. These codes are written using mainly Fortran, C, and C++.

The output of the software packages is in a BOS format [62, 63]. BOS is a Fortran-77 based dynamic memory management system. Each package will produce at least one *bank*. A bank is a collection of data words attached to a *header*. The header contains information on the number of rows and columns of data in the bank, the bank's name, and the location of the next bank in memory. Information from each detector on an event by event basis is transferred between the detector packages via these banks.

Before data can be taken using linearly polarised photons, the polarised source of photons must be calibrated online. This is explained in Chapter 4.2. For the rest of the detectors default constants are used by the reconstruction packages before more accurate calibration constants are produced in the calibration of these detectors. The constants reside in a MySql [64] database. The process is carried out offline and is summarised in Fig. 4.1.

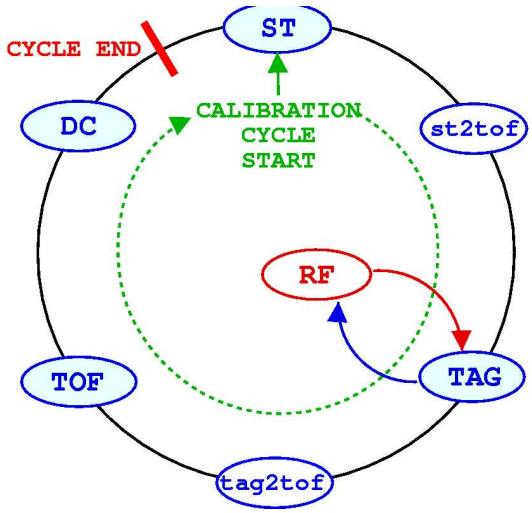

Figure 4.1: The offline calibration cycle. ST, TAG, TOF and DC represent the start-counter, photon tagger, time-of-flight and drift chamber systems respectively. RF is the accelerator machine time, while st2tof and tag2tof are constants which are used to align the systems in time. See the text for a more detailed description.

The first stage of the offline calibration process is to calibrate the start-counter. The start-counter is then aligned with the time-of-flight system using a time offset called "st2tof". Next, the photon tagger is calibrated and referenced to the machine RF time, which is the most accurate reference time available. The photon tagger is then aligned to the time-of-flight system using a time offset called "tag2tof". The time-of-flight system followed by the drift chambers are now calibrated. This marks the end of the the first calibration cycle. Many loops of the process are carried out until the constants converge to acceptable levels. After this point the electromagnetic calorimeters are now calibrated with respect to the time-of-flight system.

A time stamp was used at this point to ensure no changes to the constants would be picked up during pass 1 *cooking*. Cooking refers to the time and CPU intensive process of using the calibration constants to obtain the output used for physics analysis. *Pass 1* cooking is at the level when the calibrations constants are deemed to be final and correct. For g8a the a1c [65] package was used. This code calls all necessary reconstruction codes, and outputs the required result banks along with the raw data banks.

In the remainder of this chapter I will discuss my contribution to the calibration procedure carried out on the g8a data, focusing on start-counter, photon

tagger, and time-of-flight systems, for which I played a primary role. Brief reference will be given to the method and quality of the calibration of the remaining detector systems.

4.2 The Polarised Source

The production of linearly polarised photons using the coherent bremsstrahlung technique relies on being able to align the diamond radiator precisely at small angles ($\leq$1 mrad) with respect to the primary electron beam. In practice, this is achieved by first establishing the initial orientation relative to the beam, and then by carrying out some "calibration scans". These scans give the relationship between the crystal angle and the photon energy of the main coherent peak. A brief description of the technique and calibration procedure is given below.

4.2.1 Aligning the Radiator

The diamond radiator was aligned using the Stonehenge Technique [66]. This is a general technique for crystal alignment which was developed in Glasgow and has been used in Mainz, Bonn, and JLab. The diamond was mounted on a radiator ladder as described in Chapter 3.4.3. The ladder can rotate azimuthally(ϕ) inside a nested pair of frames, and also around the vertical and horizontal axes ($\theta_{\rm v}$ and $\theta_{\rm h}$). Fig. 4.2 shows a schematic of a mounted crystal on the goniometer. The (100) orientation of the diamond is commonly used for coherent bremsstrahlung production, and used as the basis of describing the technique. The diamond is aligned to produce coherent scattering from the sets of planes defined by the [022] and $\left[02\overline{2}\right]$ reciprocal lattice vectors.

The origin of the system is defined by $\theta_{\rm v} = \theta_{\rm h} = 0$, which ideally would coincide with the electron beam direction. However, in practice the beam will be offset by the small angles $\theta_{\rm vb}$ and $\theta_{\rm hb}$. The crystal axis (which is defined by the (100) direction in the diamonds unit cell) will also have polar and azimuthal offsets relative to the origin, represented by $\theta_{\rm t}$ and $\phi_{\rm t}$. With all the offsets (or a subset) measured, it is then possible to calculate the goniometer settings ($\theta_{\rm v}$, $\theta_{\rm h}$, ϕ) to obtain any orientation of the crystal wrt the electron beam, for any azimuthal orientation of the crystal.

The first stage of this process is to carry out a hv-scan. A *hv-scan* is when the (100) crystal axis is sweeped around in a cone of radius $\theta_{\rm s}$ by stepping sinusoidally

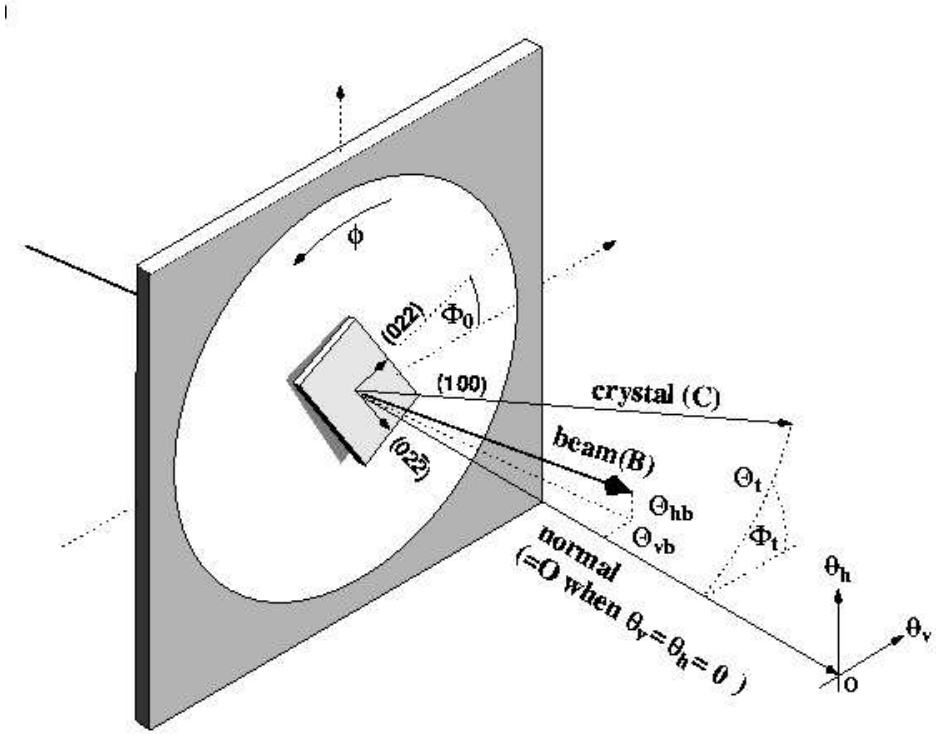

Figure 4.2: The diamond radiator mounted on a goniometer. Here $\theta_{\rm v}$ and $\theta_{\rm h}$ are vertical and horizontal axes of the pair of frames, ϕ is the azimuth of the inner plate, $\theta_{\rm hb}$ and $\theta_{\rm vb}$ are the offsets of the system wrt the electron beam direction, $\theta_{\rm t}$ and $\phi_{\rm t}$ are the polar and azimuth of the misalignment of the crystal lattice and origin of the system, and (xxx) represent the directions in the crystal unit cell.

on the $\theta_{\rm v}$ and $\theta_{\rm h}$ axes as follows:

$$\theta_{\rm v} \;=\; \theta_{\rm s}\cos(\phi) \quad \theta_{\rm h} = \theta_{\rm s}\sin(\phi) \quad \text{for}\, 0 \le \phi \le 2\pi \tag{4.1}$$

For each point in the scan, a photon energy spectrum is measured. Since the intensity is a function of E_γ, $\theta_{\rm v}$, $\theta_{\rm h}$, for a full representation of the measurement it is necessary to plot it on the surface of a cylinder. Fig. 4.3 shows a simulation of this using the anb code [48].

The regions of highest intensity form sets of curves. These arise from the coherent contributions from different sets of crystal planes as their angles change relative to the beam. The curves with the highest intensity are related to the sets of planes defined by the [022] and $\left[02\overline{2}\right]$ reciprocal lattice vectors. Vertical lines are drawn through the four points where these curves converge at $\mathrm{E}_\gamma = 0$, and a

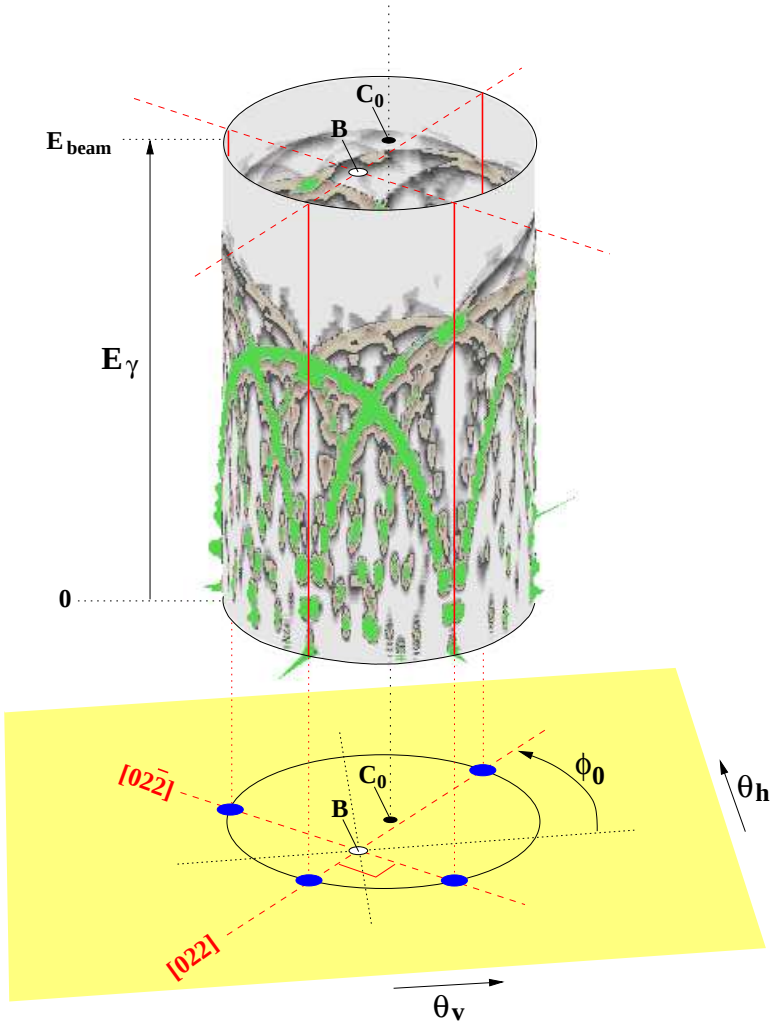

Figure 4.3: Simulation showing the construction of a Stonehenge plot from an hv-scan on a diamond crystal. Here B is the beam direction, C_0 is the direction of the (100) axis in the default position, and ϕ_0 is the default azimuthal angle of the (022) vector. All other variables are as described in the text.

Stonehenge plot is created by projecting this onto the perimeter of a circle with the photon energy increasing in the outward radial direction. An example of this is shown in Fig. 4.4. The Stonehenge plot allows the measurement of the angular offsets between the beam and the crystal, and the azimuthal orientation of the crystal lattice.

Fig. 4.5 shows two plots representing the effect of applying the technique during the g8a run. The top plot shows the 20 μm thick diamond crystal with an initial guess of the offsets. The photon tagger was in need of some maintenance work at this point in time, hence the poor resolution. A short time after this

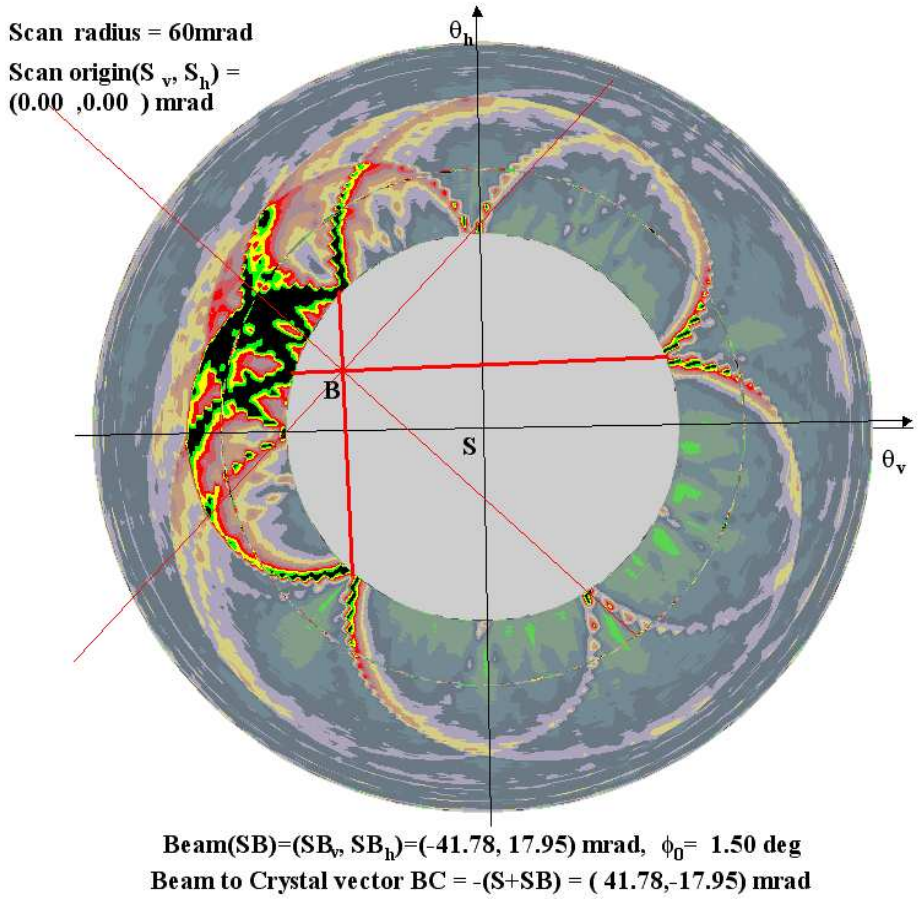

Figure 4.4: An example of a "Stonehenge plot". This is the projection of a photon energy spectrum from a hv-scan similar to that shown in Fig. 4.3 onto the perimeter of a circle.

work on the tagger another hv-scan was taken by rotating the (100) axis in ϕ increments of $\frac{2\pi}{180}$, and $\theta_s = 60$ mrad. This process was carried out until a pair of orthogonal lines was found to fit the four points where these curves converge at $E_\gamma = 0$. Further evidence that the correct points were chosen is given by the lines at 45^o to the main pair, which pass through the points corresponding to the [004] and [040] reciprocal lattice vectors. The azimuthal angle $\phi = 0^o$ is set and the crystal is then aligned with the electron beam. A further hv-scan provides a final check, and is shown at the bottom of Fig. 4.5, where it can be seen that there is a near perfect symmetry about the θ_v and θ_h axes.

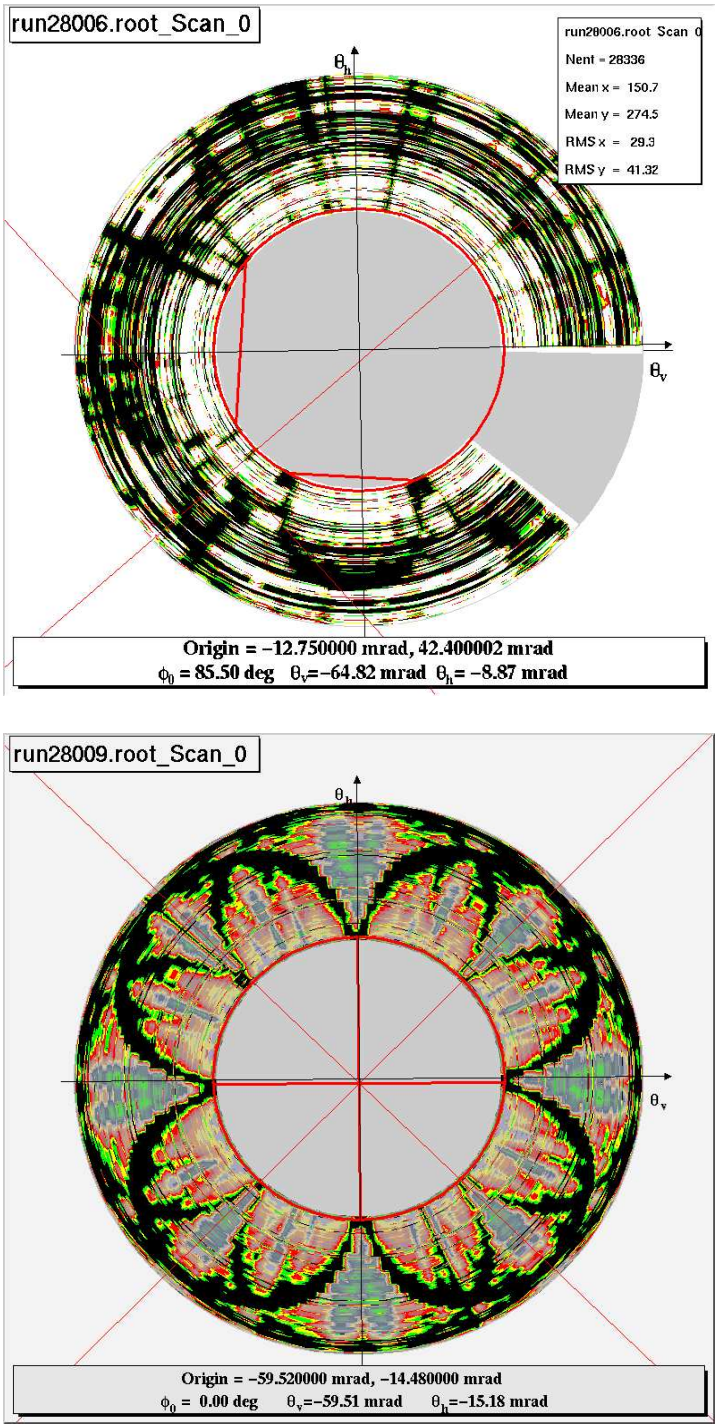

Figure 4.5: Top) A Stonehenge plot for the 20 μm thick diamond used in the g8a run while in the default position. Bottom) The same plot a short time later, after the offsets are installed. The near perfect symmetry shows the crystal is aligned well with the electron beam.

4.2.2 Calibration of the Polarised Source

Once the diamond has been been aligned for a chosen polarisation plane, on both the θ_{v} and θ_{h} axes an energy scan is carried out to produce a table of angle versus polarised photon energy. The method is described by Lothman [67]. An example of such a scan is shown in Fig. 4.6. From this it can be seen that the calibration is off by $\sim$ 2 mrad. From the table of goniometer angles, it is then possible to select the coherent edge to be at a specific photon energy. The photon energy spectrum for a particular slice of the scan is also shown in Fig. 4.6, where the coherent edge is set at $\sim$ 2 GeV. The calibration is only valid for the selected plane of polarisation, and must be repeated if this is changed. If the coherent peak drifts (e.g. due to drift in the electron beam) slightly during experimental running, the coherent angle can be adjusted to compensate for this.

4.3 Start Counter Calibration

As previously described in Chapter 3.6.2, the start-counter consists of three coupled-paddle plastic scintillator pairs. The first stage of the calibration process is to internally align each pair. This essentially means the two paddles that make a pair must be aligned with respect to each other in time. The second stage is to align the three pairs with each other. This chapter describes these two processes. I was a primary author for producing the standardised code [68] and method for this calibration, which is available to all CLAS users via the Concurrent Versions System (CVS) [69].

4.3.1 Internal Alignment

There are six Δt constants for the start-counter, each of which is associated with an individual paddle. These constants reside in the g8a database. The calibration code is run on raw data, and produces several histograms of interest. For this stage and for each of the pairs, the time difference of the TDCs of the two paddles is plotted against the time sum. Fig. 4.7 (left) shows this for one of the coupled-paddles. In this figure the real physical events correspond to the central dark region. This region is then projected onto the y-axis, as shown in Fig. 4.7 (right). By adjusting the Δt constant for each of the paddles one at a time, the main peak is then centred on zero. This is done for all three pairs.

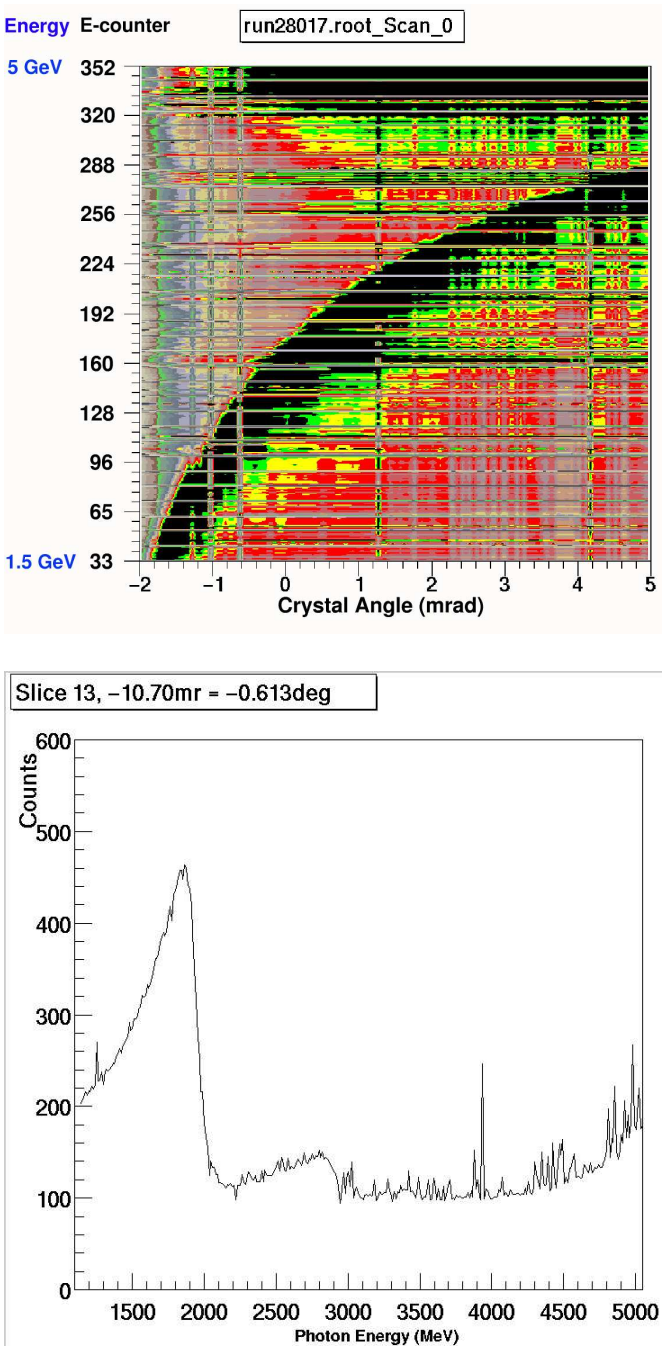

Figure 4.6: Top) A plot of photon energy versus crystal angle for the 20 μm thick diamond radiator used in the g8a run. The coherent edge is the dark line extending from the bottom left of the plot to the top right. A table of goniometer angles is produced to allow the coherent peak to be placed at a certain photon energy. Bottom) A slice of the energy calibration plot above. This is a typical photon energy spectrum that would be obtained from g8a data.

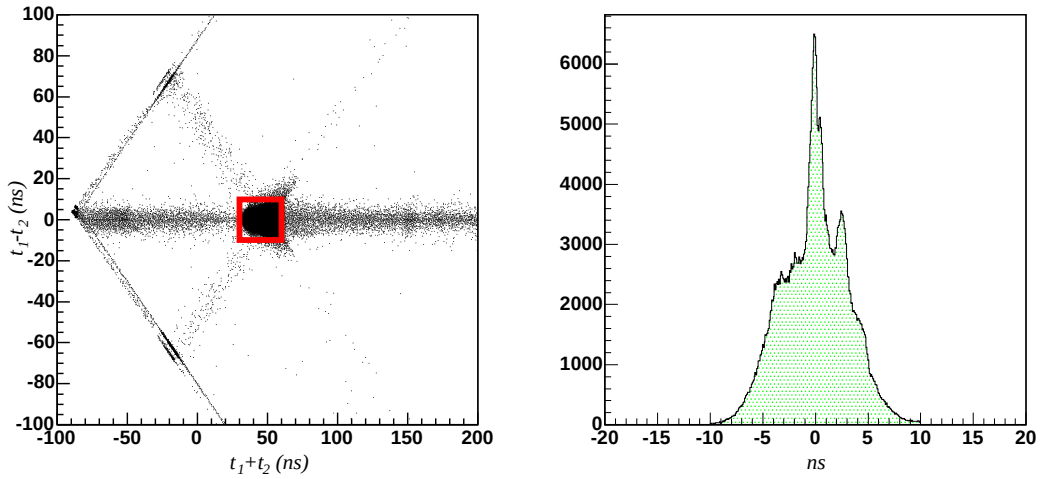

Figure 4.7: Left) An example of the time difference vs the time sum of the two paddles making up pair 1 of the start counter. The real physical events are highlighted by the red box. Right) The real events have been selected and projected onto the y-axis. The Δt constants for each paddle of pair 1 have been adjusted to centre the main peak on zero.

4.3.2 Alignment of the Coupled-Paddles

Once the peaks are aligned to zero for each pair, the alignment of the three pairs relative to each other is required. For polarised photon running we select a T-counter that is in the region of the coherent peak, as this will have the highest rate in the photon energy range of interest. The start-counter time for each pair is then subtracted from the time of the selected T-counter. An example of this for one of the pairs is shown in Fig. 4.8 (left). The Δt constants for both paddles of each pair are then changed by the same amount to align the main peak of this pair with the main peak of the other pairs. This has no effect on the internal alignment of the two paddles in each pair. Fig. 4.8 (right) shows that the coupled-paddles of the start-counter have been calibrated. It is noted that the alignment need not necessarily be to zero, as this is only an internal calibration of the detector. The uniform time for all sectors of the start counter will be referenced in the photon tagger and time-of-flight system calibrations, as discussed in the chapters below.

4.3.3 Alignment with the Time-of-Flight Paddles

In order to make an accurate time-of-flight measurement, the start-counter time must be aligned with respect to the time-of-flight counters. This is done by

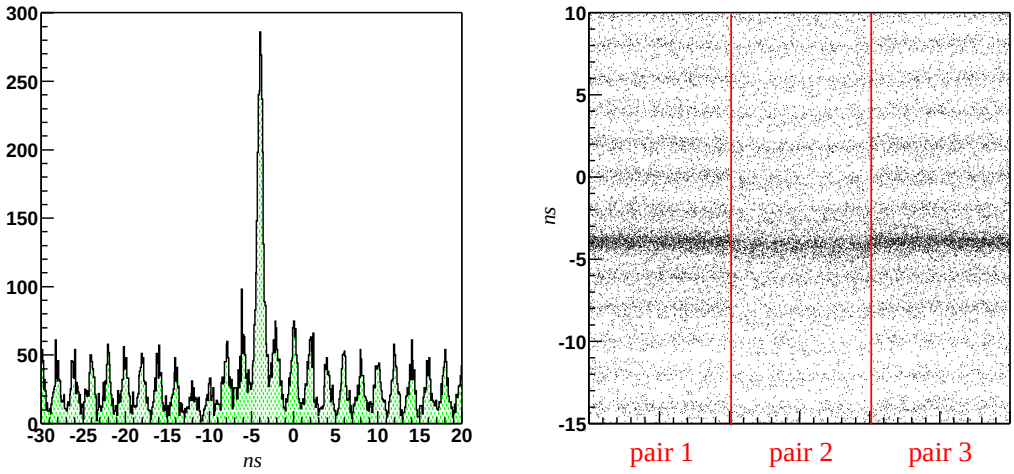

Figure 4.8: Left) A T-counter in the coherent peak minus the start counter time for pair 1. The real physical events are in the main peak. Right) The dark band through the centre of the plot shows that the three pairs are now aligned in time with each other.

looking at the vertex times as measured by the start-counter for all tracks, and then subtracting the vertex time as measured by the time-of-flight paddles for the corresponding tracks. The vertex time is obtained by projecting the track back along its trajectory to the beamline and reconstructing the time of the track at the point of intersection. The "st2tof" time offset is obtained from such a comparison as shown in Fig. 4.9. The initial calibration of the st2tof constant is rendered incorrect once the calibration of drift-chamber and time-of-flight systems is carried out. This must be altered on each loop of the calibration process to obtain the pass 1 standard of cooked data.

4.4 The Photon Tagger

The photon tagger reconstruction software [70] used by myself and others for the purpose of calibrating the g8a data uses five sets of constants. These constants must be calculated in a certain order, using the previous constants in the database to process the data in order to fit the new constants, and then using these new constants to process the data again for the next set of constants and so on. The order is as follows;

1. T-counter TDC slopes

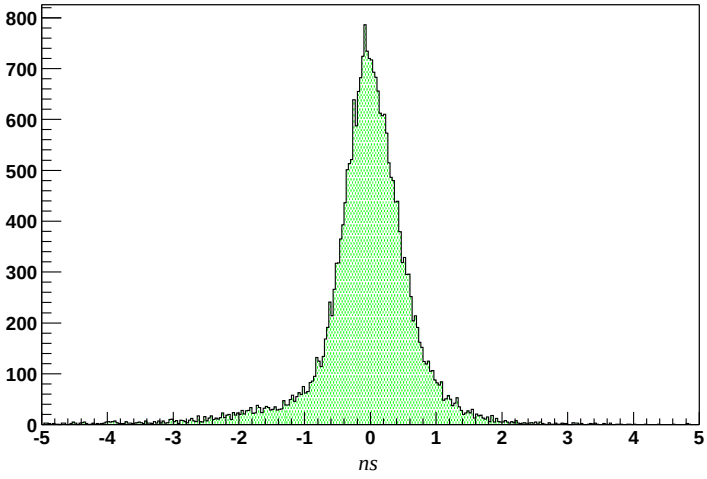

Figure 4.9: The vertex time of a track as seen by the start-counter is compared with the vertex time as seen by the time-of-flight counters. The st2tof offset is adjusted to align this difference to zero during the calibration stage. This is an example for sector 1 of CLAS. For a good calibration all sectors will have similar distributions to this.

2. Base peak calibration

3. C_i fine adjustment constants

4. Overall tagger time offset wrt ToF

5. T-counter multi-hit TDC constants

During pass 1 cooking, the tagger reconstruction package used all of these constants to provide an output bank called "TAGR". This contains time, energy, status, and T and E-counter information for every "good" hit in the focal plane on an event by event basis. Hits in the T-counter TDCs are converted to nanoseconds using the TDC slope for each channel, and then the base peak positions are subtracted. A similar method for the E-counter TDC time conversion is applied, but with the added restriction of the hits to be in channels 700-1200. The true E-T coincidences are found by geometric matching via a lookup table, and required to be within a time window of 20 ns. The T-counter times are then corrected to the nearest RF bucket with the C_i constants, and the time of the photon at the nominal centre of the target in CLAS obtained with a time offset added to this RF bucket time.

4.4.1 T-counter TDC Slope Calibration

There are two parts in the process of calibrating the T-counter TDC slopes, resulting in 61 constants for both the left and right TDCs. The first is to obtain the left-right slope balance. This is required to correct for the left-right dispersion of hits along the T-counter, as depending on the transversal position of a hit in the tagger the mean value of the left and right TDC times will differ slightly. The second is to obtain the T-counter absolute slope (the mean value of its left and right slopes). If this is not calibrated correctly, then the timing may be biased to other detectors or the RF. By measuring the slope $\beta_{R/L}$ of the drift of $\frac{<t_R - t_L>}{2}$ vs t^{mean}, and the slope β_{RF} of the drift of $< t^{mean} - t_{bucket} >$ vs t^{mean}, the correction to apply to the slopes previously used can be calculated. Here $t_{L/R}$ is the measured time for left/right TDCs, t^{mean} is the mean time for these TDCs, and t_{bucket} is the time of the electron bucket that created the photon. The new constants for the slopes can be shown to be given by Eqns. 4.2 and 4.3.

$$S_L = s_l \times \frac{1}{\left(1 - \beta_{R/L}\right) \times (1 - \beta_{RF})} \simeq \left(1 + \beta_{R/L}\right) \times (1 + \beta_{RF}) \tag{4.2}$$

$$S_R = s_r \times \frac{1}{\left(1 + \beta_{R/L}\right) \times (1 - \beta_{RF})} \simeq \left(1 - \beta_{R/L}\right) \times (1 + \beta_{RF}) \tag{4.3}$$

where $S_{L/R}$ are the new slopes for left/right TDCs, $s_{l/r}$ are the pre-calibration slopes for left/right TDCs, and other quantities are as defined previously. Fig. 4.10 shows the effect of this calibration for a typical reference run.

4.4.2 Base Peak Calibration

When looking at the T-counter TDC spectra, a peak can be clearly seen sitting on top of a background continuum. The peak for both cases corresponds to self triggered hits, while the background arises when other T-counters give the trigger. Since the T-counters are double ended, the time has a width corresponding to the transversal dispersion of the hit along the scintillator, as shown in Fig. 4.11. The 61 constants for both the left and right T-counter TDCs are obtained from fitting the left and right TDC peaks, and for each T-counter T_i, i=1,..61, comparing the delays as shown in Eqns. 4.4 and 4.5.

$$< \text{Peak(L)}_i > = < \text{TDC(L)}_i > - < \text{T(L/R)}_i > \tag{4.4}$$

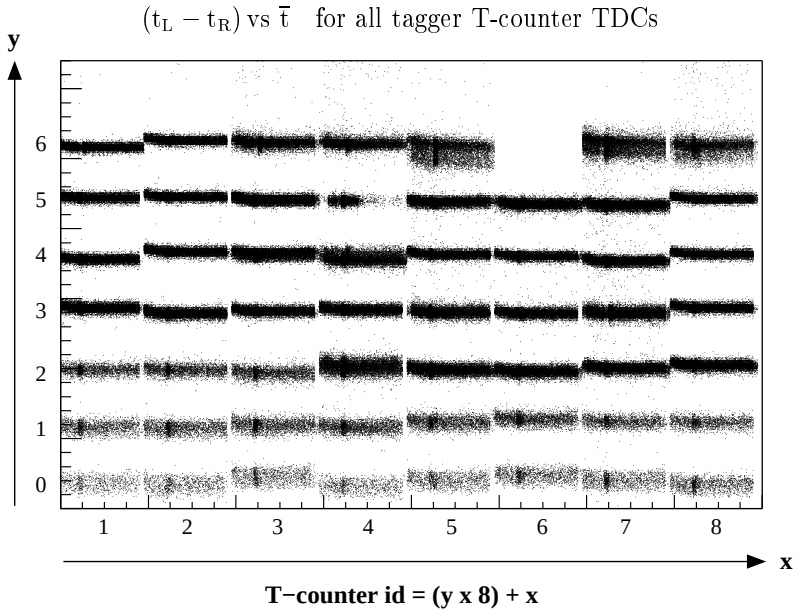

Figure 4.10: An example of the T-counter TDC slope calibration results. An arbitrary scale is used to represent all 61 T-counters, with T1 shown in the bottom left corner and increasing by one moving to the right. It can be seen that T54 is dead for this run.

$$< \mathrm{Peak(R)_i} >=< \mathrm{TDC(R)_i} > - < \mathrm{T(R/L)_i} > \tag{4.5}$$

where $\mathrm{Peak(L)_i}$ is the new constant for the T-counter TDC, $\mathrm{TDC(L)_i}$ is the delay for the discriminator output signals to stop the left TDC, $\mathrm{T(L/R)_i}$ is the left TDC delay for the discriminator output signals to trigger the acquisition divided by the same delay for the right TDC. Similar definitions apply for the right TDC constants. The time recorded by the T-counter TDCs is the TDC channel converted to time, and then the corresponding base peak constant is subtracted from this value. These constants provide a timing alignment which cannot be better than the hardware alignment of the T-counters signal at the trigger level. This misalignment is taken account of with the C_i constants as discussed below, which enable a timing alignment of better than 1 ns independent of the quality of the alignment of the signal at trigger level.

The E-counter TDC spectra also have a peak arising from self triggered hits. However, the widths are larger due to the trigger timing being given by the corresponding T-counter. The width is the sum of the jitter in the trigger resulting from the transversal dispersion of hits along the T-counter, the intrinsic resolution of the E-counter, and also from the case where a given E-counter coincides

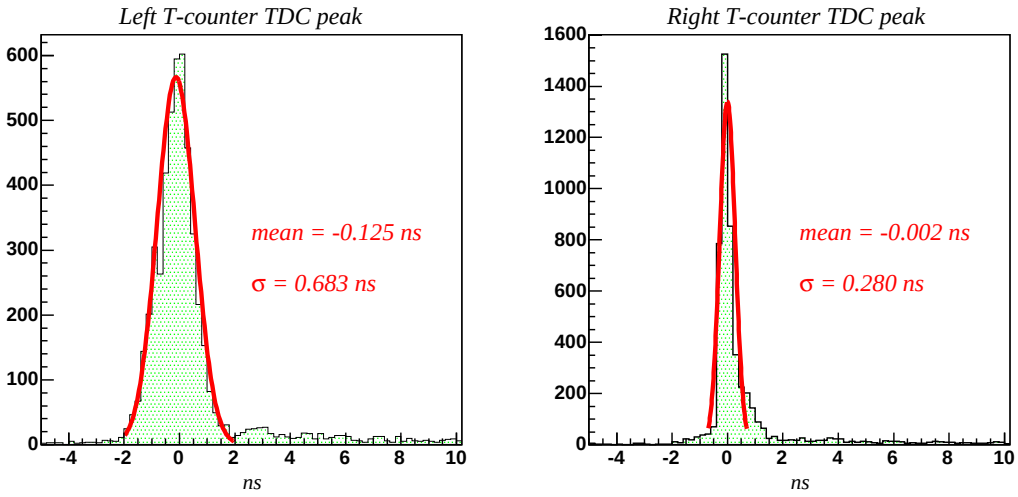

Figure 4.11: Left and right T-counter TDC peaks for T counter 21, from g8a production run29510. For this T-counter the timing was usually given by the right TDC, thus giving a narrow peak. The wider peak for the left TDC is due to transversal dispersion of the electron hits on the scintillator.

with multiple T-counters giving different trigger timing. The dominant factor in determining the width of the peak is the misalignment of the T-counters at the trigger level. The 384 constants for the E-counters are obtained by fitting the self triggered peaks, and this is subtracted from the E-counter TDC time in coincidence with a T-counter.

4.4.3 C_i Calibration

At this stage the aim of the tagger calibration is to identify the correct RF bucket that produced the reconstructed hit. The RF time is reconstructed in the CLO1 package, which provides one RF time relative to the trigger, t_{RF}. This is actually the time of an undetermined RF bucket, giving information on the phase shift between the RF machine time (period 2.004 ns) and the trigger. The bucket offset, k_{event}, between the time of the tagged photon, t_{tpho}, and the time of the RF is different for each event. The relation is shown in Eqn. 4.6.

$$t_{RF} = t_{tpho} + k_{event} \times 2.004 \tag{4.6}$$

The tagged photon is looked at via the start-counter, which is the first detector system in CLAS that will see charged particles from a hadronic reaction produced

by the photon. This is the typical choice of "reference detector" for photon running at CLAS, other possibilities being the time-of-flight paddles, pair spectrometer, total absorption counter, or electromagnetic calorimeter detectors. Using this reference detector time, t^{ref}, the misalignment of the T-counter signals at the trigger level can be found. For the T-counters, this jitter can be corrected with the constants obtained from the distribution of $t^{mean} - t^{ref}$ for each of the 121 T counter bins, (see Fig. 4.12 (left) for a particular T-counter bin). Eqns. 4.7 and 4.8 show two representations of this.

$$C_i^{ref} =< t_i^{mean} - t^{ref} > \quad \text{for i} = 1, ...121 \tag{4.7}$$

$$C_i^{ref} = (< D_i > + < T_i >) - < D_{ref} > \tag{4.8}$$

where D_i is the delay when a tagged photon is produced in the radiator for the corresponding logical signal to be output from the T-counter discriminator, T_i is the delay for the discriminator output signal to trigger the acquisition, and D_{ref} is the electronic delay between the time the tagged photon is produced and the time the corresponding signal(s) stop the TDC(s).

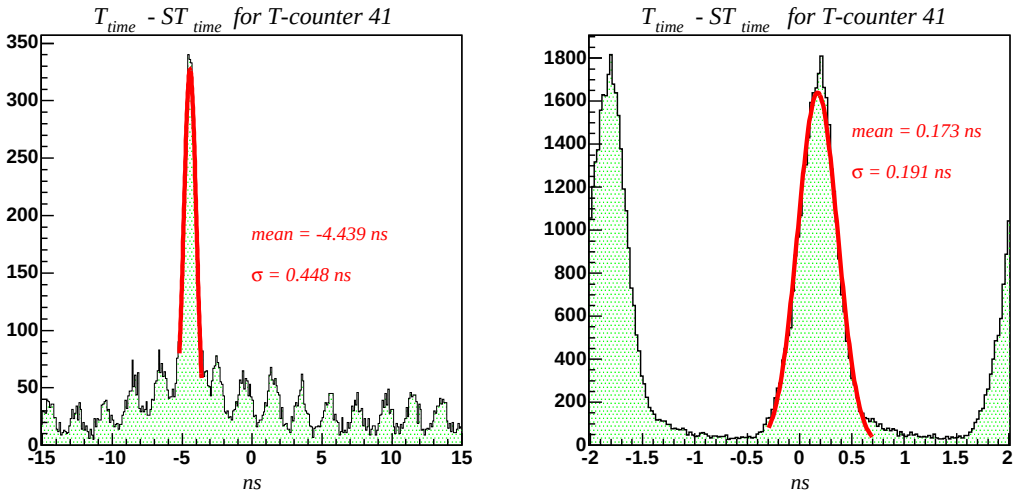

Figure 4.12: Left) T time - ST time for T-counter bin 41 for a typical g8a run. Right) T time - RF time for the same T-counter bin.

The most accurate reference signal is the RF time, which has a resolution of $\sim$ 80 ps. The problem is the uncertainty in knowing what the bucket offset between the bucket corresponding to the RF time and the bucket that corresponds

to the tagged photon is. The RF phase shifts for the T-counters can be measured using Eqn. 4.9. Fig. 4.12 (right) shows an example of the plot to calculate the C_i^{RF} offset for a particular T-counter.

$$C_i^{RF} =< D_i > + < T_i > - < t_{bucket} > + k_i \times 2.004 \tag{4.9}$$

where k_i is an integer value that can be different for each T-counter, and all other variables are as defined above. The two constants, C_i^{ref} and C_i^{RF}, are then compared to determine k_i which allows the determination of the exact C_i constant for each T counter. These relationships are shown in Eqns. 4.10 to 4.12.

$$C_i^{ref} - C_i^{RF} =< D_{ref} > + < t_{bucket} > - k_i \times 2.004 \tag{4.10}$$

$$C_i =< D_i > + < T_i > - < t_{bucket} > \tag{4.11}$$

$$C_i = C_i^{RF} - k_i \times 2.004 \tag{4.12}$$

After calculating the C_i constants, it is then possible to produce a final time of the tagger reconstruction on an event by event basis, t_{tag_0}. This is equal to the time of the bucket plus some T-counter jitter, which can then be compared to the RF time. For the best time resolution, the tagger output bank also provides the real time of the RF bucket, t_{tpho_0}. Both of these times are calculated as shown in Eqns. 4.13 and 4.14.

$$t_i^{tag_0} = t_i^{mean} - C_i \tag{4.13}$$

$$t_{tpho_0} = t^{RF} - k_i \times 2.004 \tag{4.14}$$

4.4.4 Tagger to Time-of-Flight Offset

With the RF bucket now determined independently of the T counter giving the signal, a remaining offset between the RF bucket and CLAS detectors has to be found. The convention used is that the tagger time given should be, relative to the CLAS detectors timing, the time of the tagged photon when it reached the centre of the CLAS target. During the time-of-flight calibration, highly relativistic pions are identified by $\frac{dE}{dx}$ in the time-of-flight paddles, and the time-of-flight reconstructed using the drift-chambers measurement of the particle track length. The time of vertex interaction is reconstructed, and this vertex interaction time is

included in the time from the tagger by adding an additional constant, "tag2tof", to the reconstructed time t_{tpho_0}. The tag2tof constant is changed to align the central peak of the tagger time minus the pion vertex time to zero, as shown in Fig. 4.13. The two time entries given in the TAGR bank are calculated in Eqns. 4.15 and 4.16.

$$t_{tag} = t_{tag_0} + \text{tag2tof} \tag{4.15}$$

$$t_{tpho} = t_{tpho_0} + \text{tag2tof} \tag{4.16}$$

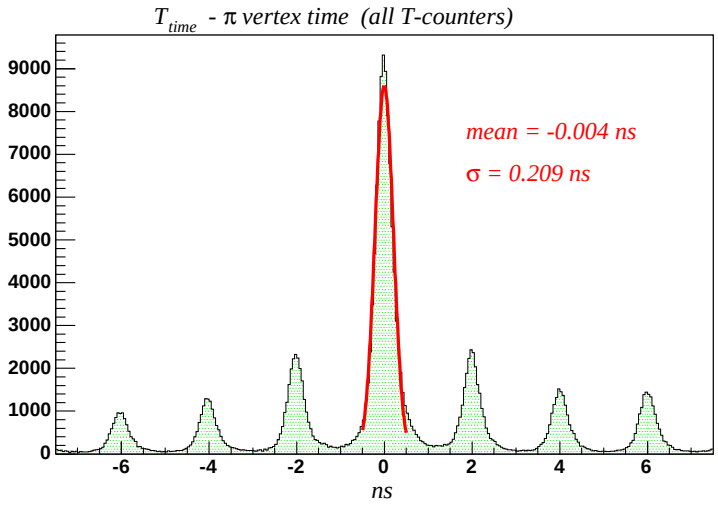

Figure 4.13: Tagger time minus pion vertex time. The value of tag2tof is chosen to align this to zero during the calibration process.

4.4.5 T-Counter Multi-Hit TDCs

The T-counter signals are also passed into a multi-hit TDC board. As mentioned previously, the resolution of these TDCs is 500 ps/ch. There are 61 constants obtained from fitting the self triggered peaks for each TDC, and a single constant obtained from a fit of the T-counter time minus the E-counter time after re-binning, geometric matching, and time matching within the E-T coincidence window. The effect of good calibration constants can be seen in Fig. 4.14. The T-counter multi-hit TDC information is taken to assist in the normalisation of the data.

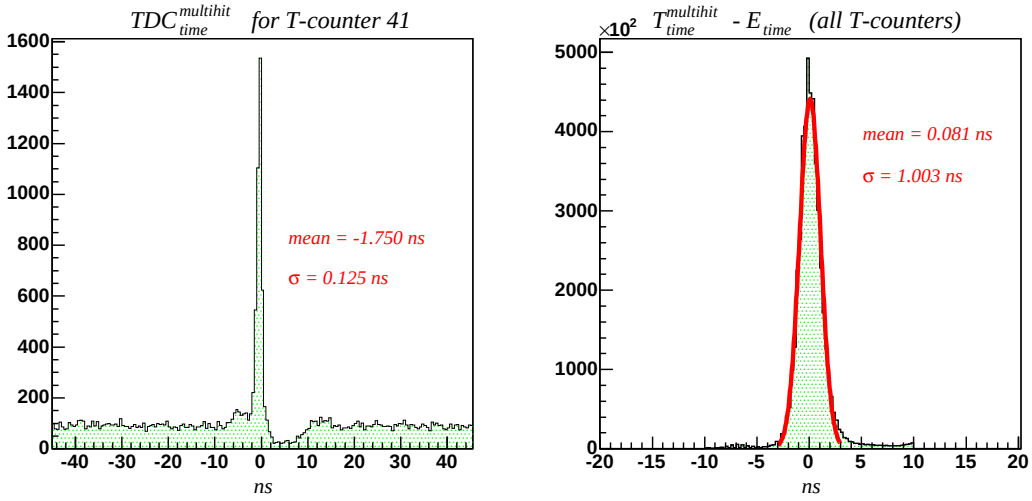

Figure 4.14: Left) Calibration of a particular T-counter multi-hit TDC. Right) Calibration of the T-counter multi-hit TDCs to the E-counter TDCs.

4.5 Calibration of the Time-of-Flight System

For photoproduction running the time-of-flight scintillators are used with the start-counter and tracking information to distinguish between different types of charged particles in CLAS. It is this step of the calibration process in which the start-counter, photon tagger, and time-of-flight systems are all aligned in time relative to one other. The mass resolution of charged particles is largely determined by the quality of calibration constants from this stage, so much care is taken to achieve the best possible results on each pass of calibrations.

The calibration of the time-of-flight for photon running in CLAS can be broken down into 9 stages, as listed in Table. 4.1. The calibration method is described fully in Ref. [71]. Each stage builds upon the information gained from the previous stage, and may also require dedicated data to obtain those particular calibration constants. Each stage is briefly described below, and where appropriate, plots are shown to represent the quality of the calibration.

4.5.1 Status

The most useful information can be obtained if it is known whether one side of a scintillator is dead or not. This information is then read into subsequent reconstruction packages, and the effect is accounted for during those particular stages. The occupancy of the left and right ADC and TDC channels are plotted

CALIBRATION STEP	REQUIREMENTS
1. Status	any raw data
2. Pedestals	pulser data
3. TDC calibration	pulser data
4. Time-walk correction	laser data
5. Left-right adjustment	any raw data
6. Energy loss	left-right time alignment at SC level
7. Attenuation length	left-right time alignment at SC level
8. Effective velocity	good TBT and all above
9. Paddle-to-paddle delays	good TBT and all above

Table 4.1: The order and requirements for the calibration of the time-of-flight system. RF is accelerator radio frequency, TBT is time-based tracking, SC is the time-of-flight BOS bank.

against the counter number to ascertain the flag to be entered in the database. The flag follows the convention shown in Table. 4.2.

FLAG NUMBER	DESCRIPTION
1	no ADC
2	no TDC
3	no ADC or TDC (PMT is dead)
5	any other reconstruction problem

Table 4.2: The counter status flag convention used in the MYSQL database.

4.5.2 Pedestals

The pedestal corresponds to the ADC channel where no data is present. For each scintillator the pedestal is measured with dedicated data using a pulser-trigger. This data is analysed online and the pedestal positions are written to the database.

4.5.3 TDC Calibration

The channel-to-time calibration of the time-of-flight TDCs is performed using a special pulser run. In this run all TDC channels are sent a group of 50 pulses simultaneously, with a fixed delay time between the TDC start and stop signal. The TDC response is then read, and the delay time is increased by 2 ns, and

the procedure is repeated. This process is repeated 200 times, and the calibration constants are calculated by fitting the channel vs time distribution with a quadratic function as shown in Eqn. 4.17.

$$t = c_0 + c_1 T + c_2 T^2 \tag{4.17}$$

where c_0, c_1, c_2 are the calibration constants, T is the raw time in units of TDC channels, and t is the converted time in ns.

4.5.4 Time-Walk Correction

Time-walk is an instrumental shift in the measured time of a TDC using a leading-edge discriminator. It is due to the finite rise time of the analogue pulse. Corrections as a function of pulse height are obtained for each PMT using special laser data. These software corrections are of the form given in Eqn. 4.18.

$$t_w = t - f_w\left(\frac{A - P}{Th}\right) + f_w\left(\frac{600}{Th}\right) \tag{4.18}$$

where Th is the channel corresponding to the leading-edge discriminator threshold, A is the value of the ADC in channels, P is the pedestal, and f_w is the time-walk correction function given in Eqns. 4.19 and 4.20.

$$f_w(x) = \frac{w_2}{x^{w_3}} \text{ if } x < w_0 \tag{4.19}$$

$$f_w(x) = \frac{w_2}{w_0^{w_3}}(1 + w_3) - \frac{w_2 w_3}{w_0^{w_3 - 1}} x \text{ if } x > w_0 \tag{4.20}$$

where w_0, w_2, w_3 are fit parameters. This parameterisation gives $t = t_w$ for minimum ionising pulses which are set to be in ADC channel 600.

4.5.5 Left-Right PMT Time Alignment

Good left-right time offsets are required to establish the hit position in the scintillator paddle. The software does not require any reconstruction, and is run on raw data. The scintillator paddle versus position of the hit is plotted for each sector, and should be a distribution that is symmetric around zero. The value of the left-right offset for each paddle is determined with Eqn. 4.21.

$$\Delta t = (P_L + P_R)/v_{eff} \tag{4.21}$$

where P_L and P_R are the left and right edges of the x-projection for each paddle number, and v_{eff} is the effective velocity in the scintillator material. The nominal value of 16 cm/ns is used in the first calibration of these offsets. In subsequent passes when more accurate cooked data is available, the more accurate measurements from Chapter 4.5.7 are used. Fig. 4.15 shows an example of correctly calibrated left-right time offsets for a g8a reference run.

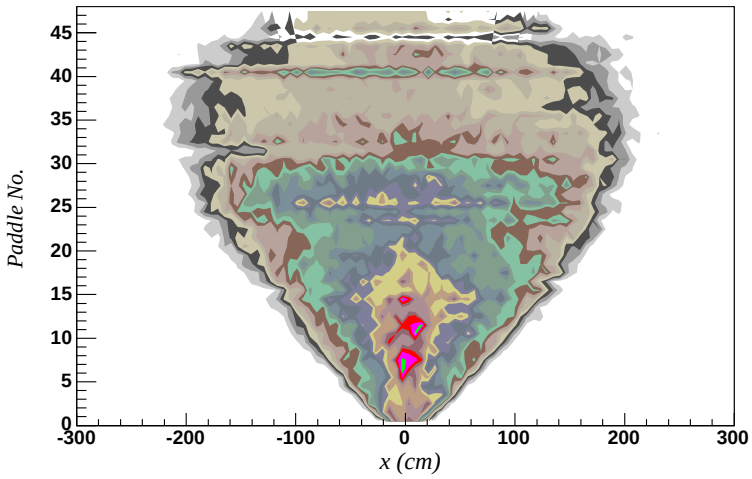

Figure 4.15: An example of left-right aligned time-of-flight paddles in sector 1.

4.5.6 Energy Loss and Attenuation Length Calibration

The separation of pions from protons without relying on timing information is possible by measuring the energy deposited in the scintillators, and also the attenuation length for each scintillator. Before these steps can be carried out the geometric mean of the minimum ionising particle (MIP) position is measured for each counter. This is done with loose timing cuts to select pions which are used for the energy loss calibration. An example of a fitted geometric mean is shown in Fig. 4.16. The energy loss and attenuation length of each counter are then obtained from the following equations;

$$E_L = \frac{k\,(A - P)}{M0_L} \quad E_R = \frac{k\,(A - P)}{M0_R} \quad E = \sqrt{E_L . E_R} \tag{4.22}$$

$$A_L - P = \frac{M0_L}{k} E_L e^{-\frac{y}{\lambda}} \quad A_R - P = \frac{M0_R}{k} E_R e^{\frac{y}{\lambda}} \tag{4.23}$$

where E_L and E_R are the normalised pulse heights of the left and right PMTs respectively, $M0_L$ and $M0_R$ are the peak heights of MIPs normally incident at the centre of the counter for left and right PMTs respectively, E is a position-independent measure of the energy deposited in the scintillator, y is the position of the hit with respect to the centre of the scintillator, λ is the measured attenuation length of the scintillator, and A and P are as described previously. The normalised pulse heights are determined so that normally incident particles at the centre of each scintillator give $E_{L,R} = k = 10\,\text{MeV}$. A correctly calibrated energy loss and attenuation length for a particular paddle is shown in Fig. 4.17, and the energy loss versus particle momenta is shown in Fig. 4.18. Proton and pion bands can be clearly distinguished in the latter plot.

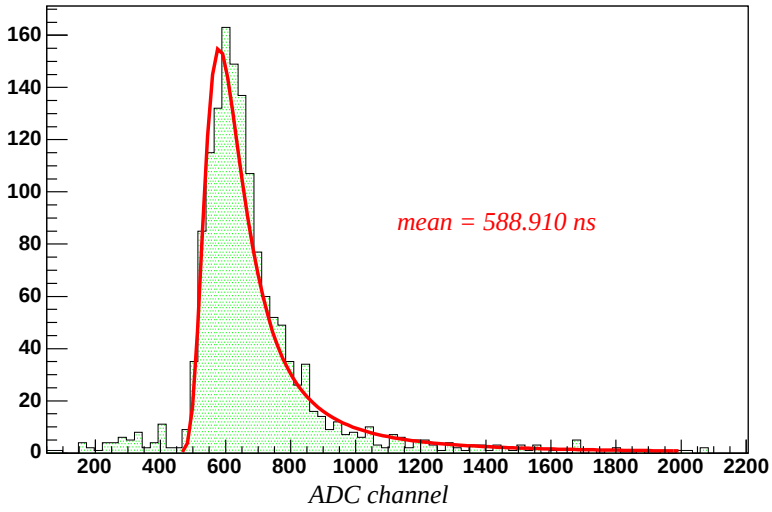

Figure 4.16: The geometric mean of a MIP position for counter 15 in sector 1.

4.5.7 Effective Velocity Calibration

The position of a hit with respect to the centre of the scintillator, y, can be determined accurately from the timing information from both ends of the counter. Using this with tracking information the time difference between the left and right PMTs versus y can be used to find the effective velocity, v_{eff}, of the scintillation light in the scintillator. The constant is measured as shown below;

$$t_L = t_0 + \frac{y}{v_{eff}} \qquad t_R = t_0 - \frac{y}{v_{eff}} \tag{4.24}$$

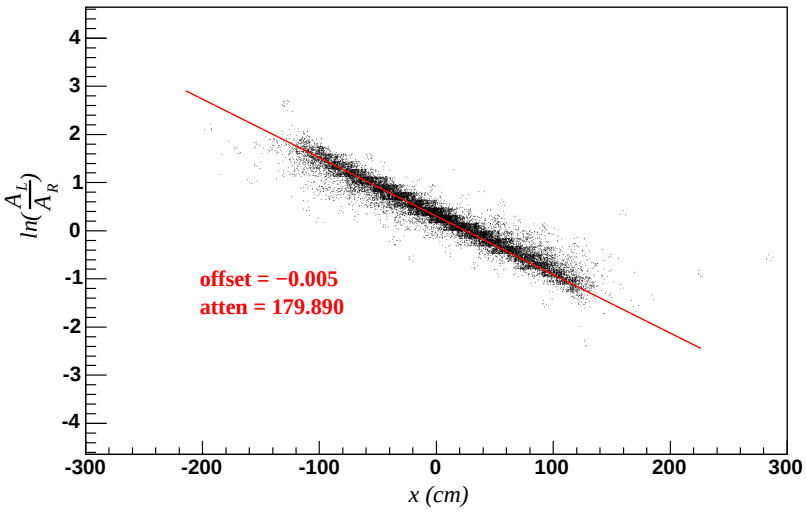

Figure 4.17: An example of a correctly calibrated energy loss and attenuation length.

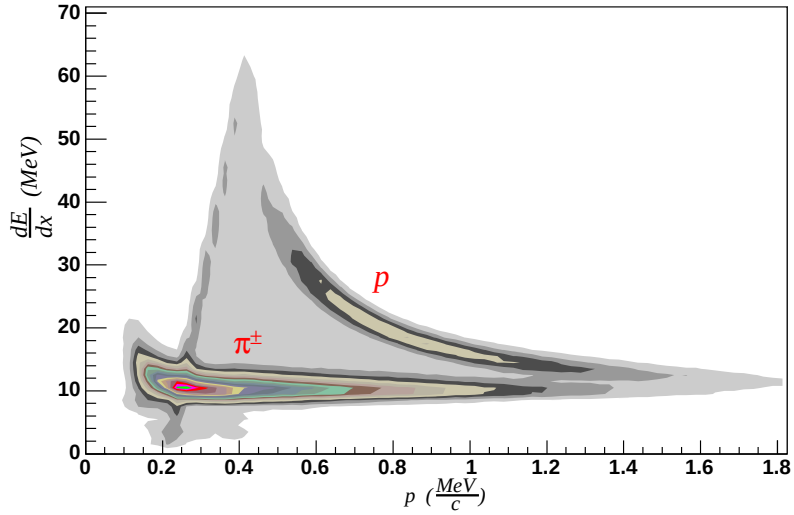

Figure 4.18: Energy loss in scintillator material versus particle momenta. The pion and proton bands are clearly distinguishable.

where t_L and t_R are the adjusted times of the left and right PMTs respectively, and all other constants are as defined previously. Fig. 4.19 shows an example of the fit used to obtain v_{eff} for a particular counter.

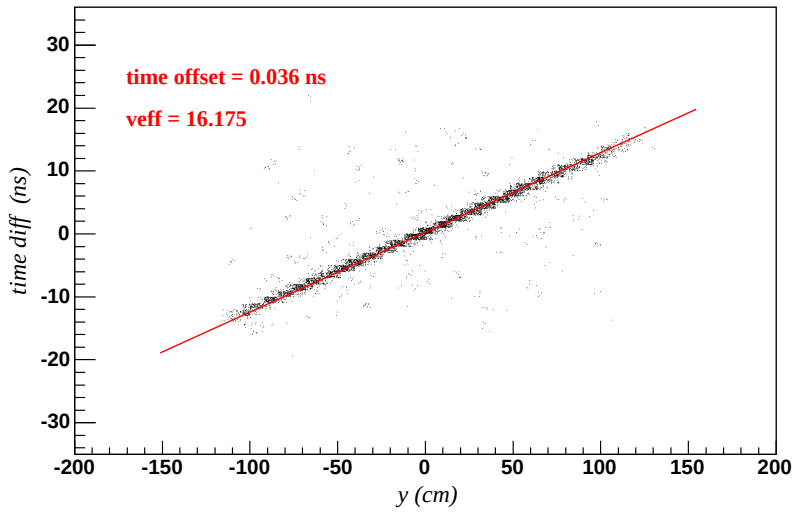

Figure 4.19: An example of a correctly calibrated effective velocity for counter 15 in sector 1.

4.5.8 Counter-to-Counter Delay Calibration

Each of the 288 counters all require to be individually aligned in time with the start-counter/tagger. The offsets are found by calculating the energy deposited in the scintillators, selecting pions by cutting on the band shown in Fig. 4.18, and then comparing the pion vertex time from the time-of-flight with the vertex time as calculated with the start-counter/tagger. An example of such a fit representing the first 39 counters in each sector is shown in Fig. 4.20. The calibration of the final nine counters is complicated by the fact that these are each made up of two adjoining scintillators and a single TDC. A correction is performed to align the relative times of the scintillators, which in hardware is the wire length from the scintillator to the TDC. After this relative adjustment, the counter can be treated just as the first 39 in each sector. Fig. 4.20 shows an example of two mis-aligned paddles that make up one of the backward angle counters.

4.6 Calibration of the Drift Chambers

There are two levels of the reconstruction of the momentum and angles of a track in the drift chambers of CLAS. The first method is with a least squares fit of the track to hit-wire positions only. This is known as "hit-based tracking" (HBT).

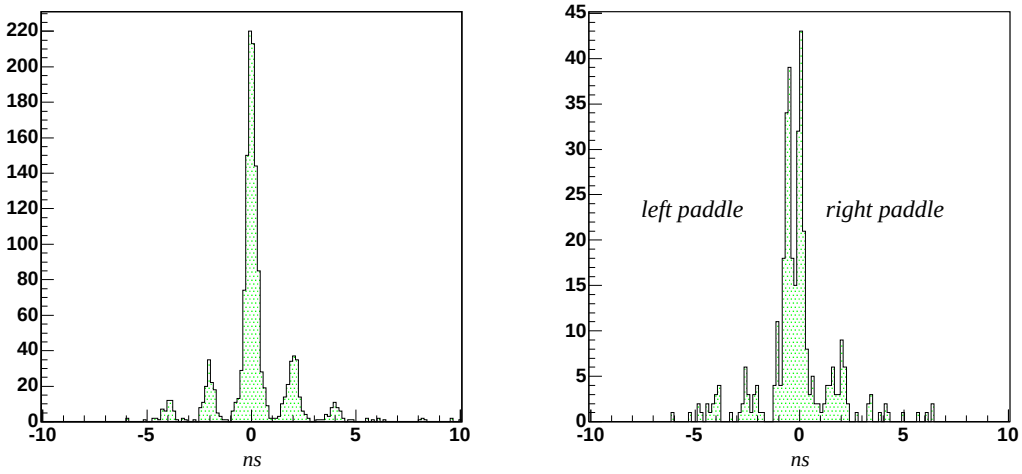

Figure 4.20: Left) Counter-to-counter delay calibration for the first 39 scintillators in each sector of the time-of-flight. Right) The mis-alignment of two paddles making up a backward angle counter. A correction must be carried out to align both of the paddles timing distributions, and then the backward angle counter can be treated just as the forward angle counters are.

The widths of the drift cells[1] and the 34 wire layers[2] limit the resolution of the track momentum for a 1 GeV/c particle with HBT to $\sim \frac{\delta p}{p} \leq 3 - 5\%$ [57].

The second method requires the measurement of the "drift-time" between the charged particle crossing the cell, and when the electron avalanche is detected on the sense wire. This information is used to localise the particle trajectory within the cells, and improves the momentum resolution for a 1 GeV/c particle to $\sim \frac{\delta p}{p} \leq$ 0.5%. The drift-time is corrected with flight-time information from the target to time-of-flight scintillators. A pre-determined look-up table is then used to convert the corrected drift times to drift distances. This is known as "time-based" tracking (TBT). Table 4.3 shows the quality of the drift chamber calibration procedure [72] for a g8a reference run. The quality exceeds the recommended values of more than 29 hits per TBT, average tracking χ^2 per degree of freedom less than 3, and a TBT/HBT ratio of greater than 0.70.

[1]The diameter of the hexagonal cells increases radially, 15 to 17 mm for R1, 26 to 29 mm for R2, and 40 to 45 mm for R3.

[2]The first super-layer has four layers of wires due to spacial constraints, whereas the remaining five super-layers have six layers each.

Sector Number	No. hits / TBT	TBT / HBT	χ^2 / DoF	Residual σ (microns)
1	30.264	0.860	1.560	317.660
2	29.547	0.828	1.540	303.898
3	31.336	0.844	1.549	319.130
4	31.961	0.851	1.573	300.455
5	30.022	0.853	1.672	316.343
6	27.944	0.859	1.535	293.042
AVERAGE	30.179	0.849	1.571	308.420

Table 4.3: A summary of drift chamber properties after calibration for a g8a reference run.

4.7 The Electromagnetic Calorimeters

As mentioned in Chapter 3.6.6, there are forward angle electromagnetic calorimeters in all sectors of CLAS, but only large angle calorimeters in the first two sectors. These detectors are used to enable the discrimination between neutrons and photons, and also to calculate the kinetic energy of neutrons. The calibration technique [73] employed by g8a for the forward electromagnetic calorimeter is based on events where the two photon decay of neutral charged pions are detected. The vertex time of a track as seen by the forward electromagnetic calorimeter system is then compared to the vertex time of the track as seen by the time-of-flight system. A good calibration will select constants that centre this distribution around zero. A similar technique is employed for the large angle calorimeter. Fig. 4.21 shows how the timing of the electromagnetic calorimeters look for a correctly calibrated g8a reference run.

4.8 The Active Collimator

The active collimator contains four radially mounted scintillators whose PMTs allow six asymmetries to be measured. During the g8a run there were two beam position monitors (BPMs), BPM21X, and BPM21Y, which are positioned upstream of the photon tagger. The BPMs monitor the electron beam quality and stability, but offer no information on the quality of the photon beam passing through the collimator. In the calibration technique for the collimator [74] each of the asymmetries are plotted against the output of the BPMs. Constants relating the BPM information to the asymmetries measured from the collimator

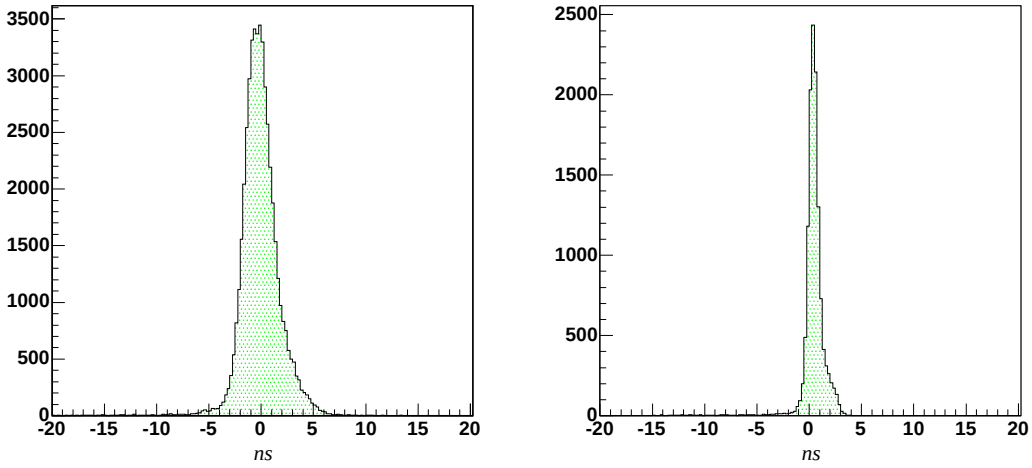

Figure 4.21: The vertex times of tracks as seen by the electromagnetic calorimeter (left), and large angle electromagnetic calorimeter (right), with respect to the vertex times measured by the time-of-flight counters.

PMTs are obtained by fitting a straight line to these plots as shown in Fig. 4.22. With the BPM and the PMT information the position of the photon beam passing through the collimator after this calibration can be measured to an accuracy of ~ 20 μm [74]. Events can then be rejected when the photon beam strays too close to the collimator wall as the level of background entering the CLAS detector would be undesirable and make physics analysis of the data more complicated.

4.9 Summary

The calibration procedures of the detectors used in linear polarised photon beam experiments at JLab have been described in this chapter. Results which are representative of the output of these procedures for the g8a data set have also been presented. It is hoped that this description will be of help to new members of the CLAS collaboration when embarking on similar experimental running. The following chapter will describe the method of particle identification in the CLAS detector system and also the corrections applied to the measured four-momenta of reconstructed tracks.

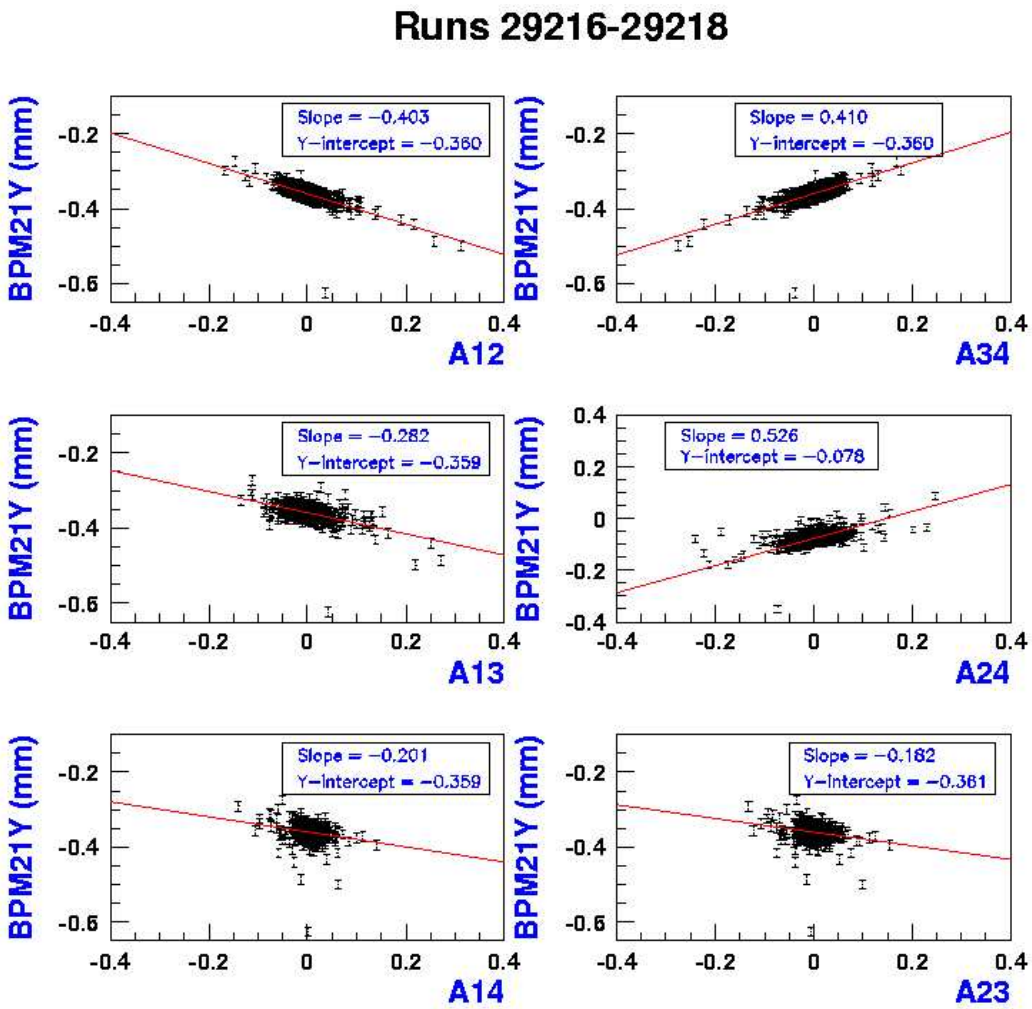

Figure 4.22: The six possible asymmetries from the PMTs of the active collimator are plotted against one of the BPMs upstream of the collimator. The calibration process involves fitting these distributions to obtain constants that relate the BPM and PMT readings to one another. This enables the monitoring of the position of the photon beam as it passes through the collimator.

Chapter 5

Particle Identification and Event Selection

5.1 Introduction

For this analysis on the ρ^0 meson, the exclusive $\overrightarrow{\gamma}\mathrm{p} \rightarrow \mathrm{p}\pi^+\pi^-$ reaction is used. This requires the detection of all three outgoing particles in the CLAS system. The identification of any charged particle in CLAS is achieved using information from the start-counter, time-of-flight counters, and drift chambers. The detection of neutral particles is not discussed in this chapter as it is not required in the physics analysis of this work. The particle momentum is measured in the drift chambers, and by measuring the path lengh and time from the target to both the start-counter and time-of-flight planes, the mass and velocity of the particle can be calculated as given in Eqns. 5.1 and 5.2.

$$\beta = \frac{\mathrm{d_{sc}} - \mathrm{d_{st}}}{\mathrm{c}\,(\mathrm{t_{sc}} - \mathrm{t_{st}})} \tag{5.1}$$

$$\mathrm{m} = \frac{\mathrm{p}}{\gamma\beta} \tag{5.2}$$

where β is the particle velocity, $\mathrm{d_{st}}$, $\mathrm{d_{sc}}$ and $\mathrm{t_{st}}$, $\mathrm{t_{sc}}$ are the path length and time from the target to the start-counter and scintillators respectively, c is the speed of light, m is the mass of the particle, p is the measured momentum of the particle, and $\gamma = (1 - \beta^2)^{-\frac{1}{2}}$. Figs. 5.1 and 5.2 show the β vs momentum and mass distributions for positively charged hadrons respectively. The band structure in Fig. 5.1 for each particle is a result of the loose timing cuts made in measuring

the momenta of the tracks. This is clearly inadequate, and is improved upon by the method described below.

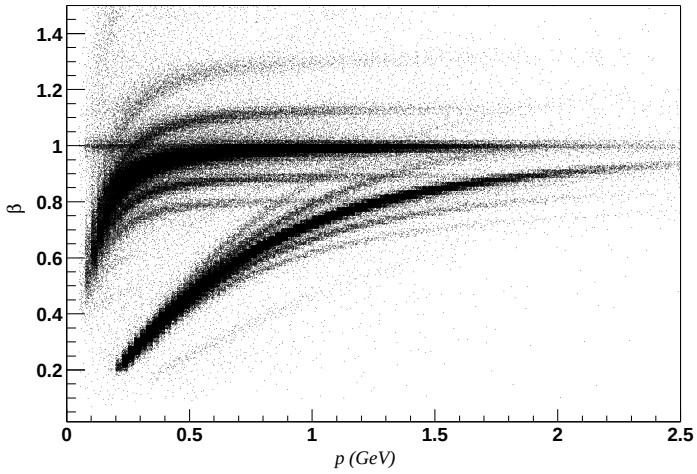

Figure 5.1: β versus momentum for positively charged hadrons. The over-lapping bands result from loose timing cuts in measuring the momenta of the tracks.

5.1.1 The GPID Scheme

To establish the correct particle type, the γ-particle-identification-scheme (GPID) [75] was followed in this analysis. The philosophy of this scheme was to bring together the many ideas previously employed in particle identification (PID) in photoproduction experiments in CLAS, and thus create a standard for each experimental run to adhere to. A previous scheme, PART, simply made cuts on the mass plots shown in Fig. 5.2 to determine each particle type. Tracks lying outwith the shaded regions on this plot are classified as unknown. This method is clearly inadequate and leaves many tracks to be analysed in more depth by the individual as they see fit. GPID uses information from the reconstructed banks of the photon tagger, time-of-flight scintillators, time-based tracking, and PART scheme to improve the PID in a systematic manner.

For each charged particle track the particle velocity (β_{m}) is calculated from the measured time-of-flight between the start-counter and time-of-flight counters. A new particle velocity is then calculated (β_{c}) using the measured momentum of the track and assuming that the particle is a pion. The energy of the particle is then re-calculated using the nominal mass of a charged pion and the difference

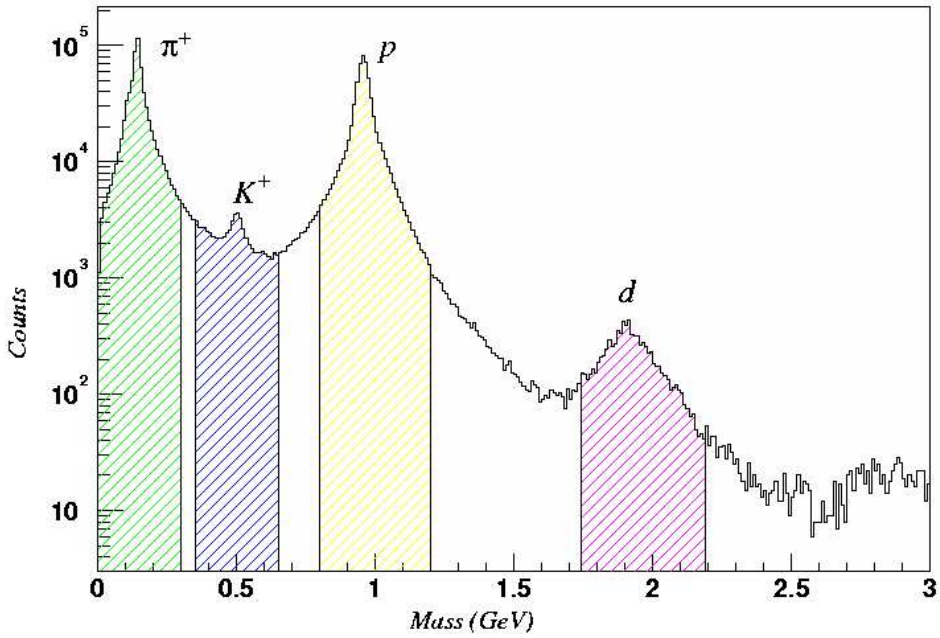

Figure 5.2: The mass distribution for positively charged hadrons shown on a log scale to emphasise the kaon and deuteron peaks. The shaded areas represent the cuts used by the PART method of particle identification, as discussed in Chapter 5.1.1.

between β_c and β_m calculated. This process is repeated using the nominal masses of the charged kaon, proton, deuteron, and triton. The nominal mass providing the minimum difference between β_c and β_m then provides the PID.

The corresponding photon that created the hadronic event in CLAS is then found by looping over the reconstructed tagger bank. The time for each good photon in this bank is relative to the centre of the target in CLAS for the g8a run. A correction to this time is applied to take into account the position along the target which the event originated, and then this is compared with start-counter vertex time. The photon whose corrected time is closest to the start-counter vertex time is taken to be the "good" photon.

The benefit of using the GPID scheme can be seen from the plots in Fig. 5.3. These represent a sample of data in which at least one kaon candidate is detected. This is done to highlight the improvement of this PID scheme in correctly identifying kaons, which the PART method using only invariant mass cuts does not perform adequately. The overlap of the distribution of each positive hadron results in the invariant mass cuts misidentifying many K^+ candidates as π^+ or protons (see top left plot in Fig. 5.3), so an improvement in kaon identification is also an improvement in pion and proton identification which is essential to this work. A look at the comparison of the measured masses for positive hadrons identified with both the PART and GPID methods (top right and bottom plots in Fig. 5.3) shows the improvement in further detail. Table 5.1 details the difference in numbers of the most common particle types detected for both methods. The particles are given the nominal mass of the particle type as identified by the GPID method and a plot of beta vs momentum in Fig. 5.4 shows the pion, kaon, and proton bands are now clearly observable. The background outwith the bands is discussed in Chapter 5.3.

Particle Type	No. PART	No. GPID	Diff (%)
p	8932	9880	+10.6
π^+	8189	12664	+54.6
π^-	4394	6054	+37.8
K^+	14386	11248	-21.8
K^-	3128	1766	-43.5
d	124	113	-9.1
t	0	51	nan
unknown	2581	0	nan

Table 5.1: The numerical difference in PID using the PART and GPID schemes.

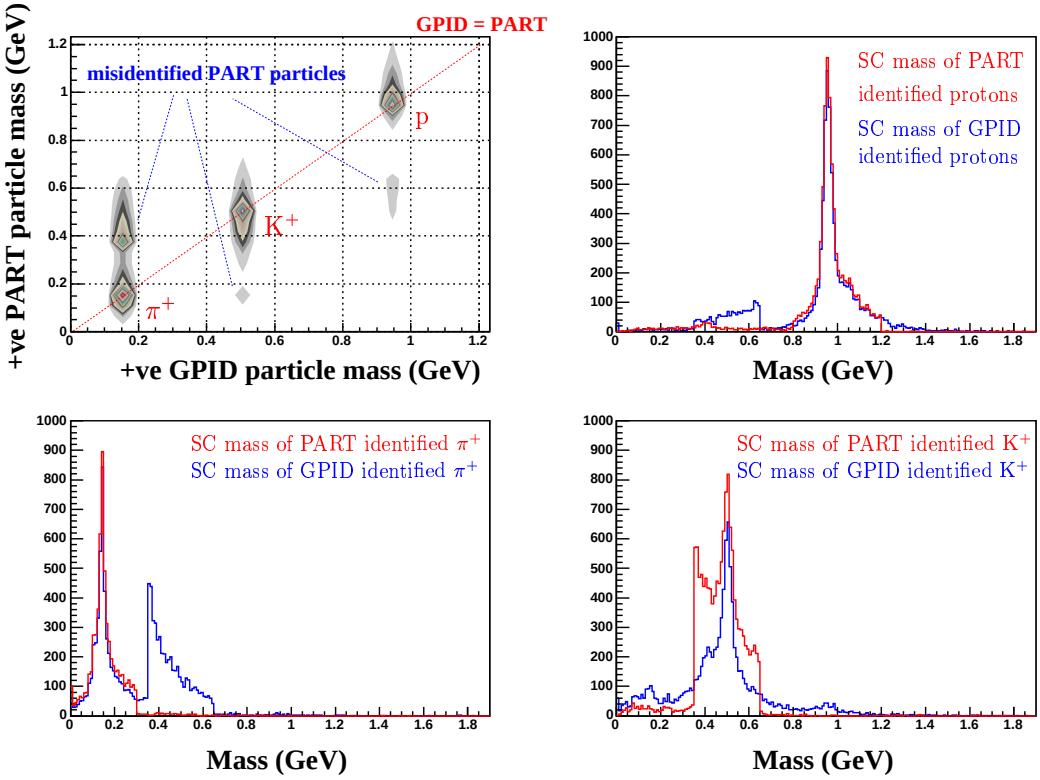

Figure 5.3: Top left) The measured invariant mass for positive hadrons identified using the PART method of PID is plotted against the nominal mass of the same particles using the GPID scheme. The diagonal line shows the agreement in the PID of both schemes and misidentified particles using the PART method show up as enhancements off this line. The other three plots show a comparison of the measured mass for the proton, π^+ and K^+particles identified using both the PART and GPID schemes. These highlight the problem of identifying K^+using only the SC mass in the PART method. In the GPID scheme many of the K^+ are assigned the PID of a π^+, and a smaller amount of K^+ assigned the PID of a proton.

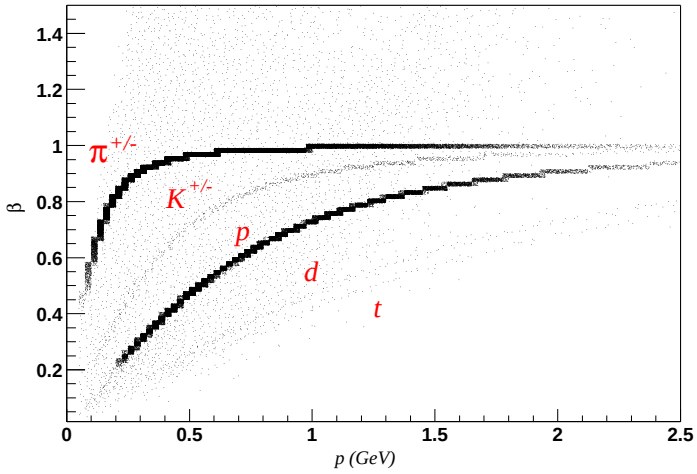

Figure 5.4: Once the GPID scheme has been carried out, the β vs momentum plot becomes a lot clearer. The correctly identified charged hadrons are seen in clear bands. The background is discussed in Chapter 5.3.

5.2 Exclusive $p\pi^+\pi^-$ Event Selection

During the g8a experiment data was taken with the torus magnet set to positive polarity. This bends the positively charged particles away from the beamline to give the maximum possible acceptance for these particles. However, this reduces the acceptance for negatively charged particles, as many of the forward going negatively charged particles are bent down the beamline, and therefore go undetected. The choice of analysing an exclusive reaction with a negatively charged particle will therefore reduce the number of suitable events, but the ambiguities associated with reconstructing particles using the missing mass technique are now avoided.

To select an exclusive $p\pi^+\pi^-$ event the following selection process is followed. First of all, only events with one of each particle type are considered. Next, the four momentum of the incident photon and target are added together, and then the four momentum of each outgoing particle is subtracted. A missing four momentum is then available to check that only these three outgoing particles were produced in the hadronic reaction in CLAS. Fig. 5.5 shows the missing $mass^2$, missing energy, missing longitudinal momentum, and also the missing transverse momentum. All of these show a peak centred close to zero, but some empirical corrections have to be applied to the four momenta of the particles before defining

the final cuts to be made. These corrections are discussed in Section 5.2.1.

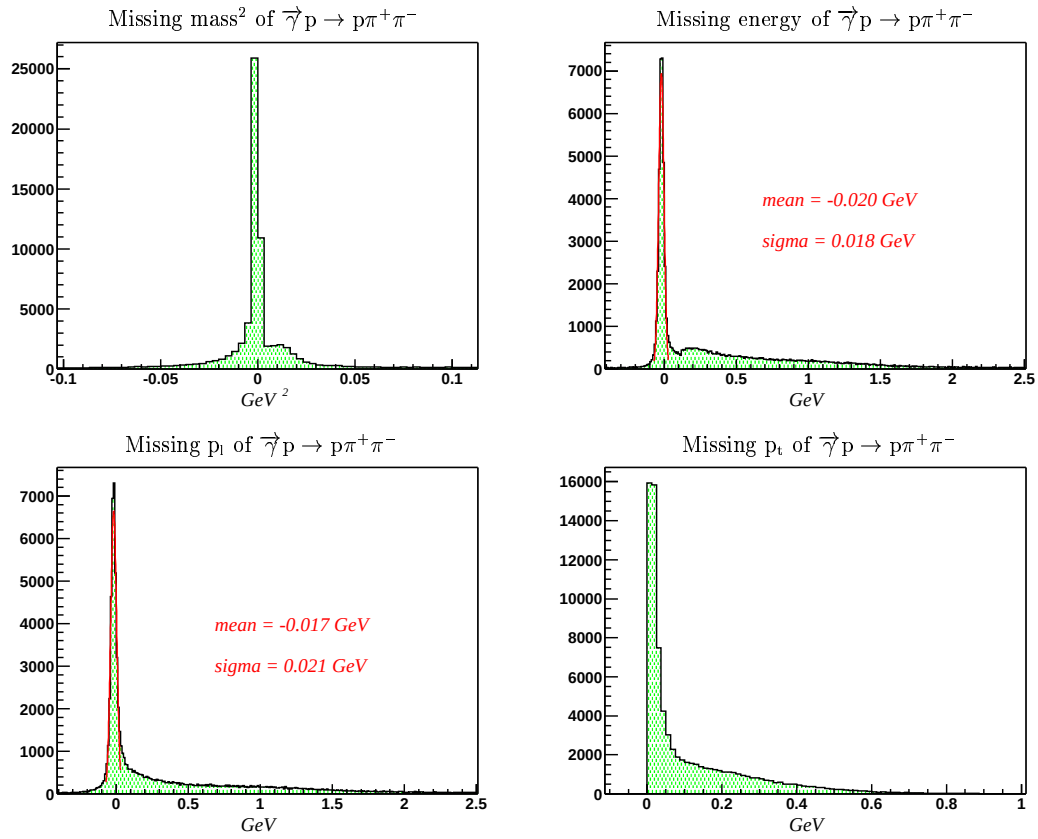

Figure 5.5: The missing mass^2, missing energy, missing longitudinal momentum, and missing transverse momentum distributions for the exclusive $\vec{\gamma}p \to p\pi^+\pi^-$ reaction before energy loss and momentum corrections.

5.2.1 Energy Loss and Momentum Corrections

From the fits to the missing energy and missing momentum in Fig. 5.5, it can be seen that the peaks are not centred exactly on zero. This is because a charged particle will deposit energy in the target material, target walls, the beam pipe, and also in the start-counter. This energy loss results in the measured momentum in the drift chambers being less than the original momentum of the particle when it was produced at the vertex. It is calculated by passing the 4-momentum of the charged particle, the target geometry, and the vertex information into the standard CLAS energy loss routine [76], which itself is a set of subroutines. This can be applied to any particle that has a charge of ± 1, and which is heavier than an electron. For such a particle with a mass m, momentum p, the routine is valid

for the range $0.05 < \frac{p}{m} < 50$. The distributions of the energy correction applied to all three particles of interest are shown in Fig. 5.6.

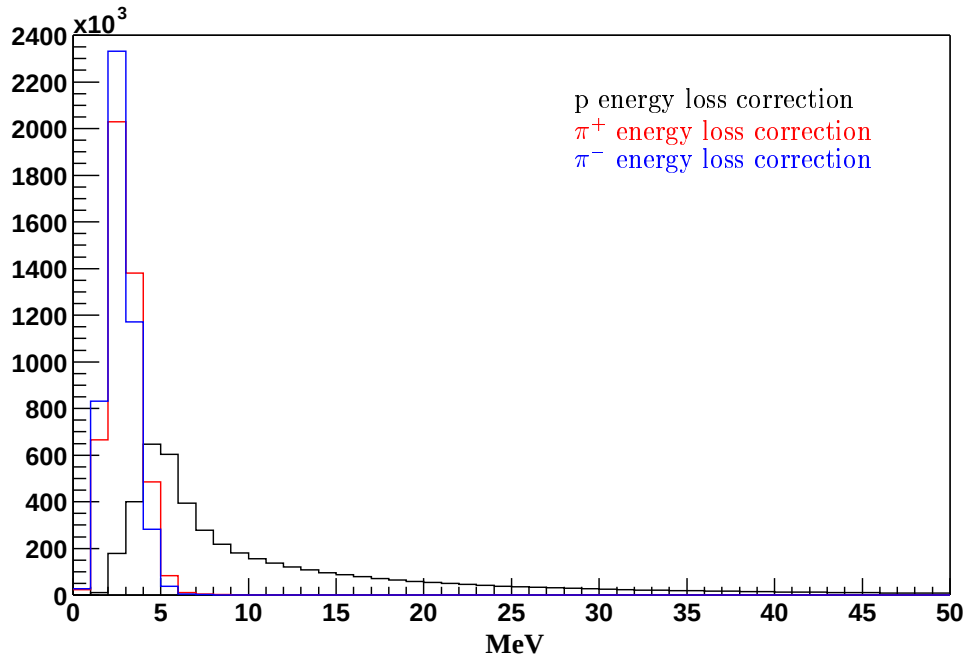

Figure 5.6: The distribution of the energy correction applied to the proton (black), π^+ (red), and π^- (blue) particles.

As well as the energy loss correction for each particle of interest, the particle's momentum has to be corrected to account for the difference between the theoretical magnetic field in CLAS, and the actual magnetic field used during the experiment. The method employed was developed by the g6c experimental run [77], which ran directly after g8a. In this method relatively pure $\vec{\gamma}p \to \pi^+\pi^-\pi^0 p$ events are selected. Looking at the missing mass of the proton a clear ω peak is seen ($\omega \to \pi^+\pi^-\pi^0$ with a branching ratio$\sim$ 89%, $\Gamma = 8.4$ MeV).

It is assumed that the errors are all from the 3-momentum of the proton, which is equivalent to saying that CLAS measures all the angles correctly. In principle, the difference between the measured and the calculated values of magnitude of the proton's momentum (p) is a function of (p, $\cos\theta$, ϕ), where θ and ϕ are the polar and azimuthal angles of the proton in the laboratory frame. Previous investigations have found the ϕ-dependence is weak in all six sectors and so the momentum correction is binned as a funtion of ($|p|$, $\cos\theta$). For each of these bins the omega peak is moved to the accepted mass of 780 MeV [19] by changing

the measured momentum of the particles using the parameterisation shown in Eqn. 5.3.

$$dp = F_0\,[s] + F_1\,[s]\cos(\theta) + F_2\,[s]\,p + F_3\,[s]\cos^2(\theta) + F_4\,[s]\,p^2 + F_5\,[s]\,p\cos(\theta) \tag{5.3}$$

where F_x are fit parameters for each sector s and all other variables are as described above. To obtain constants for the π^+ and π^- particles a similar method is applied using the proton corrections already found with another reaction channel, $\overrightarrow{\gamma}p \rightarrow p\pi^+\pi^-$. Again relatively pure events are selected but this time it is assumed the errors occur entirely from the π^+ now. The missing mass of the $p\pi^+$ then reveals a slightly shifted π^- peak which is corrected with a similar parameterisation. The π^+ corrections are then applied along with the p corrections and the missing mass of the $p\pi^-$ is used to correct the π^- in a similar manner. This *bootstrapping* method was applied to the g8a data set to establish the 108 fit parameters required for the three particles and a function is then called during the physics analysis to apply these parameters to correct the 3-momentum for each particle;

$$\Delta p = p - dp \tag{5.4}$$

$$p_x^{cor} = \Delta p \sin(\theta)\cos(\phi) \tag{5.5}$$

$$p_y^{cor} = \Delta p \sin(\theta)\sin(\phi) \tag{5.6}$$

$$p_z^{cor} = \Delta p \cos(\theta) \tag{5.7}$$

$$E^{cor} = \sqrt{\left(m^2 + (p_x^{cor})^2 + \left(p_y^{cor}\right)^2 + (p_z^{cor})^2\right)} \tag{5.8}$$

where m is the particle mass. The effect of applying both the energy loss and momentum corrections to the three outgoing particles is shown in Fig. 5.7. The following cuts are now applied to choose exclusive $p\pi^+\pi^-$ events from the g8a data set;

$$|\text{missing mass}^2| \leq 0.004\,\text{GeV}$$

$$|\text{missing longitudinal/transverse momentum}| \leq 0.04\,\text{GeV}$$

$$|\text{missing energy}| \leq 0.04\,\text{GeV}$$

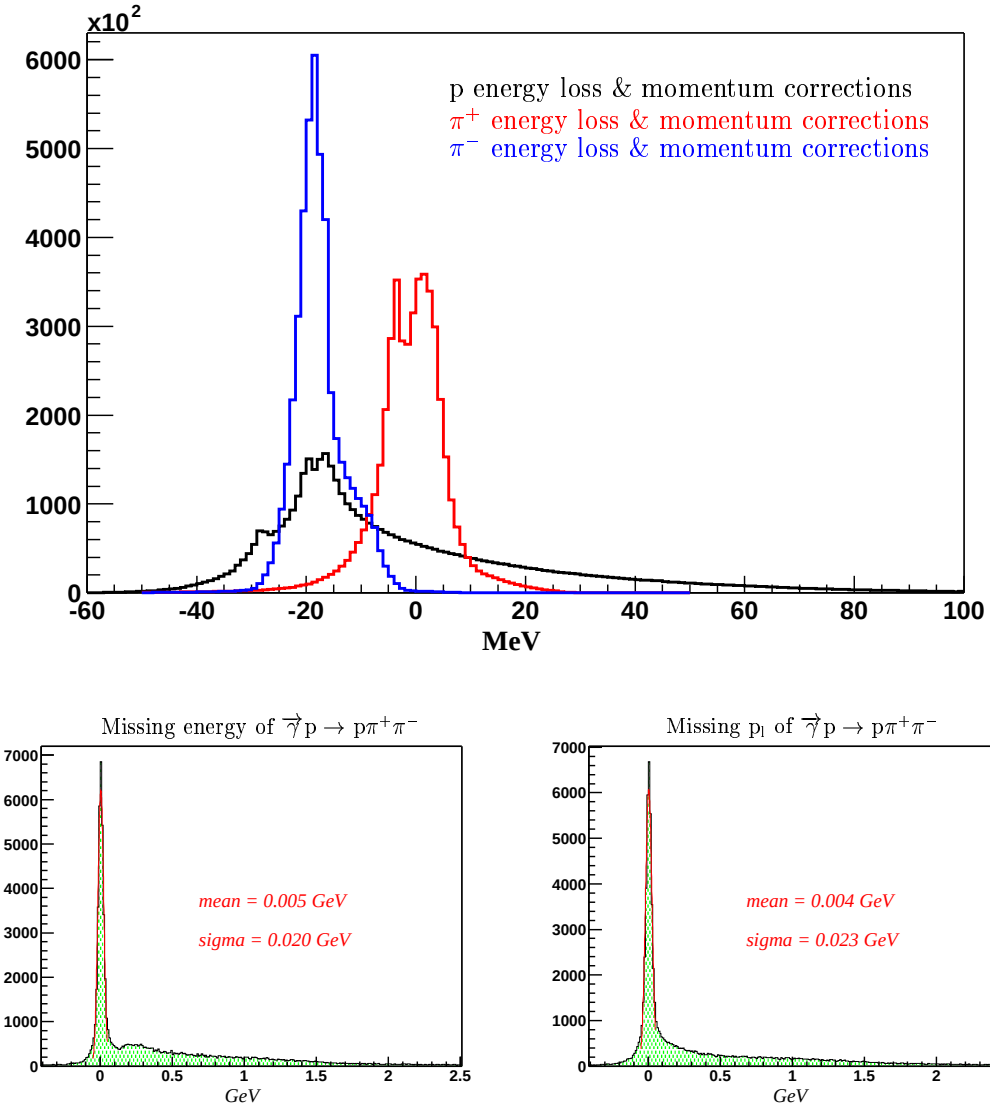

Figure 5.7: Top) The distribution of the energy loss and momentum corrections applied to the proton (black), π^+ (red), and π^- (blue) particles. Bottom) The missing energy (longitudinal momentum) for the exclusive $\overrightarrow{\gamma}p \to p\pi^+\pi^-$ reaction is now centred on ∼5 MeV (∼4 MeV), when before the energy loss and momentum corrections were applied the peak was centred on ∼-20 MeV (∼-17 MeV).

5.3 The Effect of GPID Failure

The GPID scheme is successful in identifying the correct particle type most of the time, but there are occasions where it fails. This is due to the reconstructed track in CLAS having either a bad start-counter time, a bad time-of-flight time, or both. A result of this failing is the background lying outside the clear bands in the beta versus momentum plots for charged particles, as shown previously in Fig. 5.4. The major concern arising from this plot is whether or not exclusive events which have one or more mis-identified particle are being analysed further?

In Fig. 5.8, a similar plot to Fig. 5.4 is made, but only after the selection of exclusive $p\pi^+\pi^-$ events. The two clear bands corresponding to the proton and pions are the only significant features in this plot. The curves are set to place boundaries on the PID. For the event selection being analysed, on average the GPID scheme will result in particles of interest lying outwith these boundaries $\sim 0.2\%$ of the time. For events where there is an occurance of this failure for one or more particles, the event is rejected. In summary, the effect of mis-identified particles following the GPID scheme will contribute almost zero effect to the analysis of this channel.

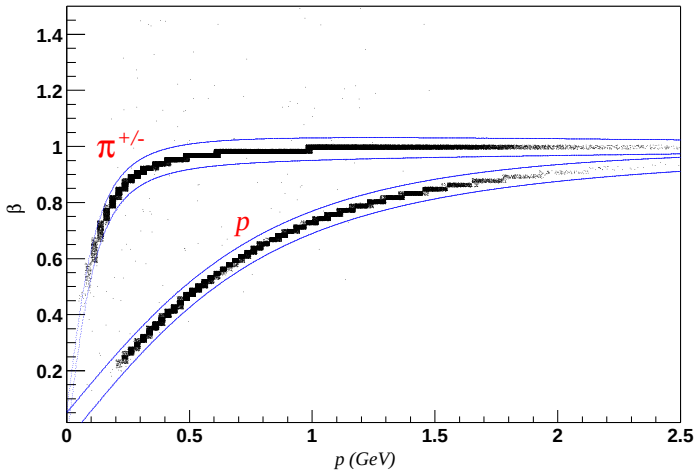

Figure 5.8: After applying the cuts to select exclusive $p\pi^+\pi^-$ events, the distribution of protons and pions is significantly cleaned up. The boundaries for each particle are used to reject events from further analysis when the GPID scheme fails for any of the particles.

Chapter 6

Data Analysis

6.1 Extraction of the ρ^0 Signal

For analysis of the ρ^0 signal, the first step after selecting exclusive $\overrightarrow{\gamma}p \rightarrow p\pi^+\pi^-$ events is to look at the invariant mass spectrum of the $\pi^+\pi^-$ detected within the full angular coverage of CLAS, as shown in Fig. 6.1. The CERN Particle Data Group [19] state the mass of the ρ^0 to be 769.3 ± 0.8 MeV, and the full width $\Gamma = 150.2 \pm 0.8$ MeV. The measured values from fitting a gaussian to the distribution in Fig. 6.1 of m $\sim 753.0 \pm 0.1$ MeV and $\Gamma \sim 160$ MeV are consistent with these values. However, the shoulders either side of the ρ^0 peak result in the peak being of a non-gaussian form. The reasons and limitations imposed by this observation are discussed below.

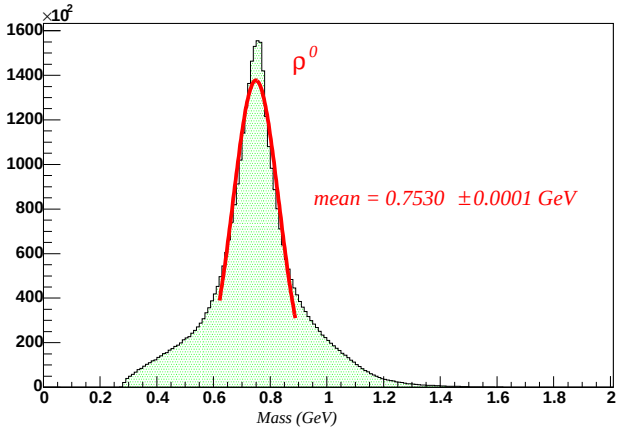

Figure 6.1: The invariant mass spectrum of the $\pi^+\pi^-$ detected in CLAS from exclusive $\overrightarrow{\gamma}p \rightarrow p\pi^+\pi^-$ events.

For an exclusive event selection with three detected particles, we are left with three possible permutations from which the detected particles were produced. One of these has already been stated previously, i.e. the $\pi^+\pi^-$ and the proton. The two alternative permutations are therefore $p\pi^+$ and π^-, and $p\pi^-$ and π^+. The invariant mass of the $p\pi^+$ and $p\pi^-$ pairs are shown in Figs. 6.2 and 6.3. There is clear structure in the invariant mass of the $p\pi^+$ and $p\pi^-$ pairs, and it is the presence of these structures which result in the shoulders of the ρ^0 peak appearing when looking at the invariant mass spectrum of the $\pi^+\pi^-$.

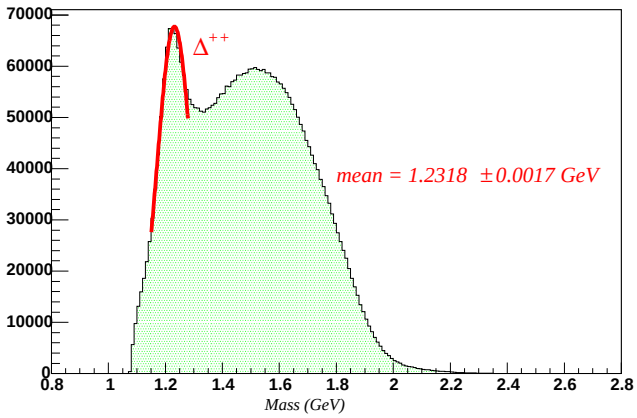

Figure 6.2: The invariant mass spectrum of the $p\pi^+$ detected in CLAS from exclusive $\overrightarrow{\gamma}p \rightarrow p\pi^+\pi^-$ events.

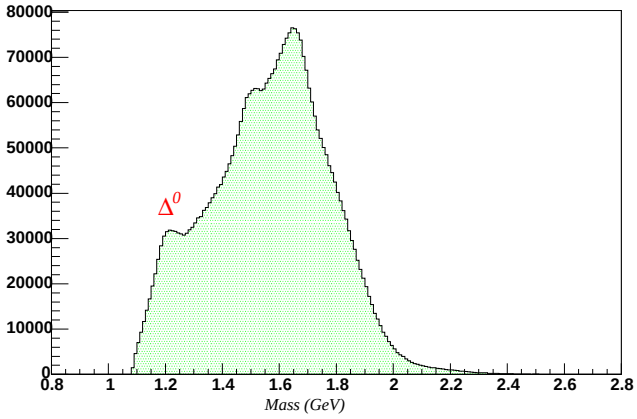

Figure 6.3: The invariant mass spectrum of the $p\pi^-$ detected in CLAS from exclusive $\overrightarrow{\gamma}p \rightarrow p\pi^+\pi^-$ events.

To understand the extent of this problem it is helpful to look at Dalitz[1] plots for the channel $\overrightarrow{\gamma}p \to p\pi^+\pi^-$, as shown in Fig. 6.4. On both of these plots the red vertical band at $m^2_{\pi^+\pi^-} \sim 0.6\,GeV^2$ corresponds to the ρ^0. On the left plot there are at least three horizontal bands on the $m^2_{p\pi^-}$ axis which are interfering with the ρ^0 signal. On the right plot the main horizontal band at $m^2_{p\pi^+} \sim 1.5\,GeV^2$ corresponds to Δ^{++} interference.

The polar distribution of $\pi^+\pi^-$ pair in the $(\overrightarrow{\gamma}, p)$ c.m. system is shown in Fig. 6.4. The evolution of the contamination of the ρ^0 signal can be observed by examining invariant mass and Dalitz plots as a function of this angle. Figs. 6.5, 6.6, and 6.7 show the invariant mass distributions of the $\pi^+\pi^-$, $p\pi^+$, and $p\pi^-$ pairs respectively. Figs. 6.8 and 6.9 show the Dalitz plots with the same binning. In the invariant mass plots the blue shaded distributions represent the effects cutting on the invariant masses of the three pairs to emphasise the ρ^0 signal. The cuts employed are stated below and are represented by the red lines in the plot at the top of Fig. 6.4.

$$0.35 \leq m_{\pi^+\pi^-} \leq 0.82\ GeV^2$$
$$m_{p\pi^\pm} \geq 1.60\,GeV^2$$

The application of these invariant mass cuts results in the ratio of events passing the cuts to those without cuts imposed to experience an initial sharp fall. The trend of this ratio versus the polar angle of the $\pi^+\pi^-$pair is compared to the polar distribution of the $\pi^+\pi^-$pair in Fig. 6.10. In this comparison it is apparent that the cuts have a pronounced effect at forward angles with the ratio mimicking the forward diffractive peak of the polar distribution of the $\pi^+\pi^-$pair. This behaviour settles down to become relatively constant from $\theta_{c.m.} \sim 60 - 70^\circ$ onwards.

From the invariant mass distributions in Fig. 6.5 it is clear that the ρ^0 signal is progressively swamped by background and other processes as $\theta_{c.m.}$ increases. Beyond the hump in the polar angle distribution of the $\pi^+\pi^-$ pair at $\theta_{c.m.} \sim 60 - 70^\circ$ a more vigorous approach than invariant mass cuts based on the Dalitz plots is required. A full partial-wave analysis (PWA) will be required to extract the strengths of all processes contributing to these distributions, which is outwith the time constraints of this first analysis of the g8a data.

However, at lower values of $\theta_{c.m.}$ it is meaningful and reasonable to assume the invariant mass cuts enhance the ρ^0 signal and for the first time there are a

[1]The Dalitz plot [78] is a way to represent the entire phase space of any three-body final state in a scatter plot or 2-D histogram.

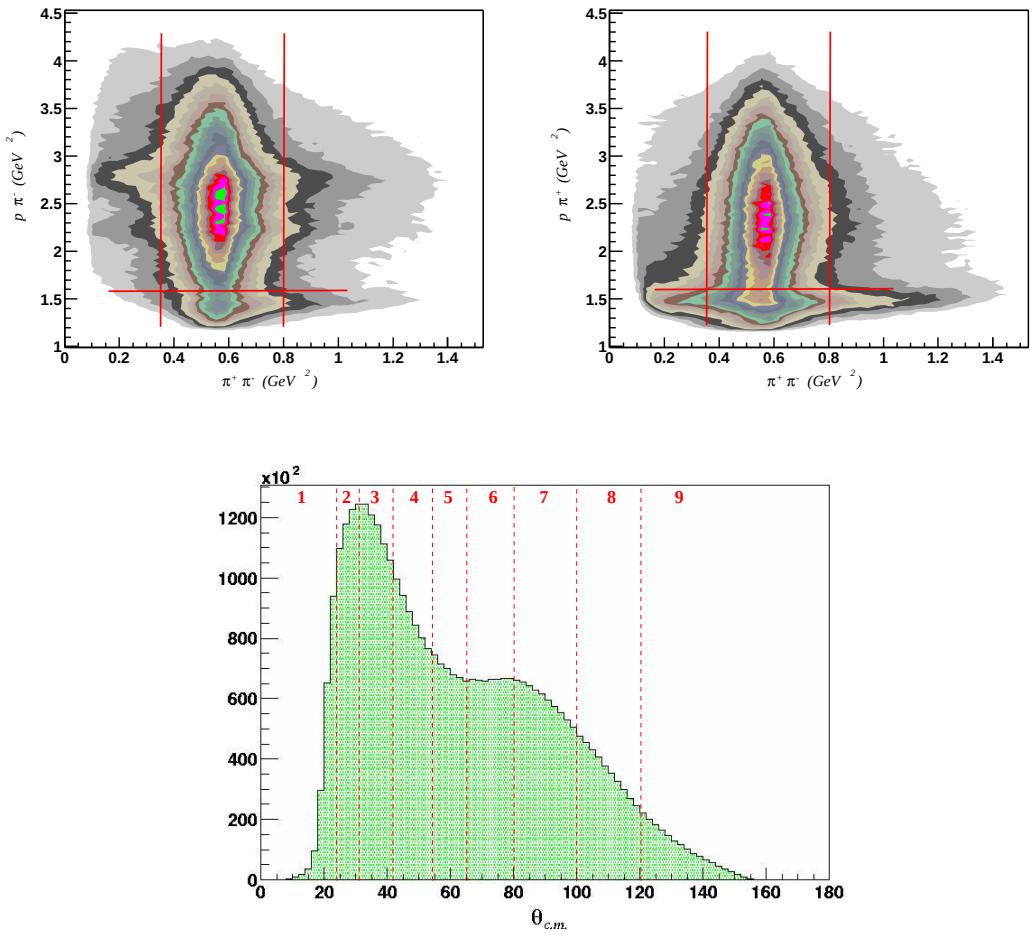

Figure 6.4: Top) Dalitz plot distributions for the channel $\overrightarrow{\gamma}p \to p\pi^+\pi^-$. On the left, the $m^2_{p\pi^-}$ is plotted against the $m^2_{\pi^+\pi^-}$. The red vertical band at $m^2_{\pi^+\pi^-} \sim 0.6\,\mathrm{GeV}^2$ corresponds to the ρ^0, while the horizontal bands correspond to multiple interfering resonances. On the right, the $m^2_{p\pi^+}$ is plotted against the $m^2_{\pi^+\pi^-}$. Once again the red vertical band at $m^2_{\pi^+\pi^-} \sim 0.6\,\mathrm{GeV}^2$ corresponds to the ρ^0, while the main horizontal band at $m^2_{p\pi^+} \sim 1.5\,\mathrm{GeV}^2$ corresponds to Δ^{++} interference. The red lines indicate the cuts used to enhance the ρ^0 signal. Bottom) The polar distribution of the $\pi^+\pi^-$ pair in the $(\overrightarrow{\gamma}, p)$ c.m. system. The red lines indicate the binning used in this analysis, see Table 6.1 for more detail.

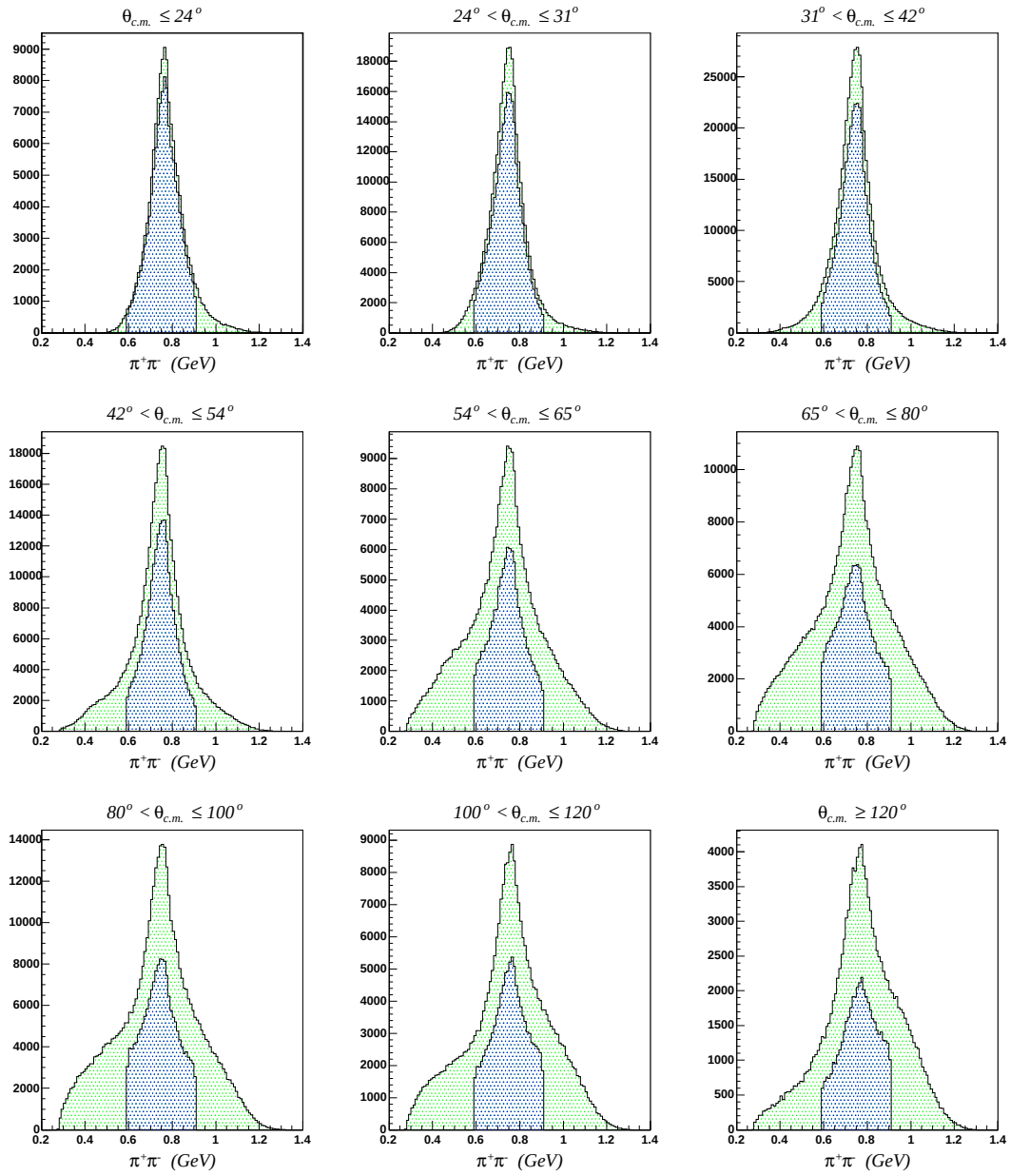

Figure 6.5: The invariant mass spectrum of the $\pi^+\pi^-$pair binned in polar angle of the pair in the $(\overrightarrow{\gamma}, \mathrm{p})$ c.m. system. The blue shaded distributions represent the effects cutting on the invariant masses of the $\pi^+\pi^-$, $\mathrm{p}\pi^+$, and $\mathrm{p}\pi^-$ pairs to emphasise the ρ^0 signal.

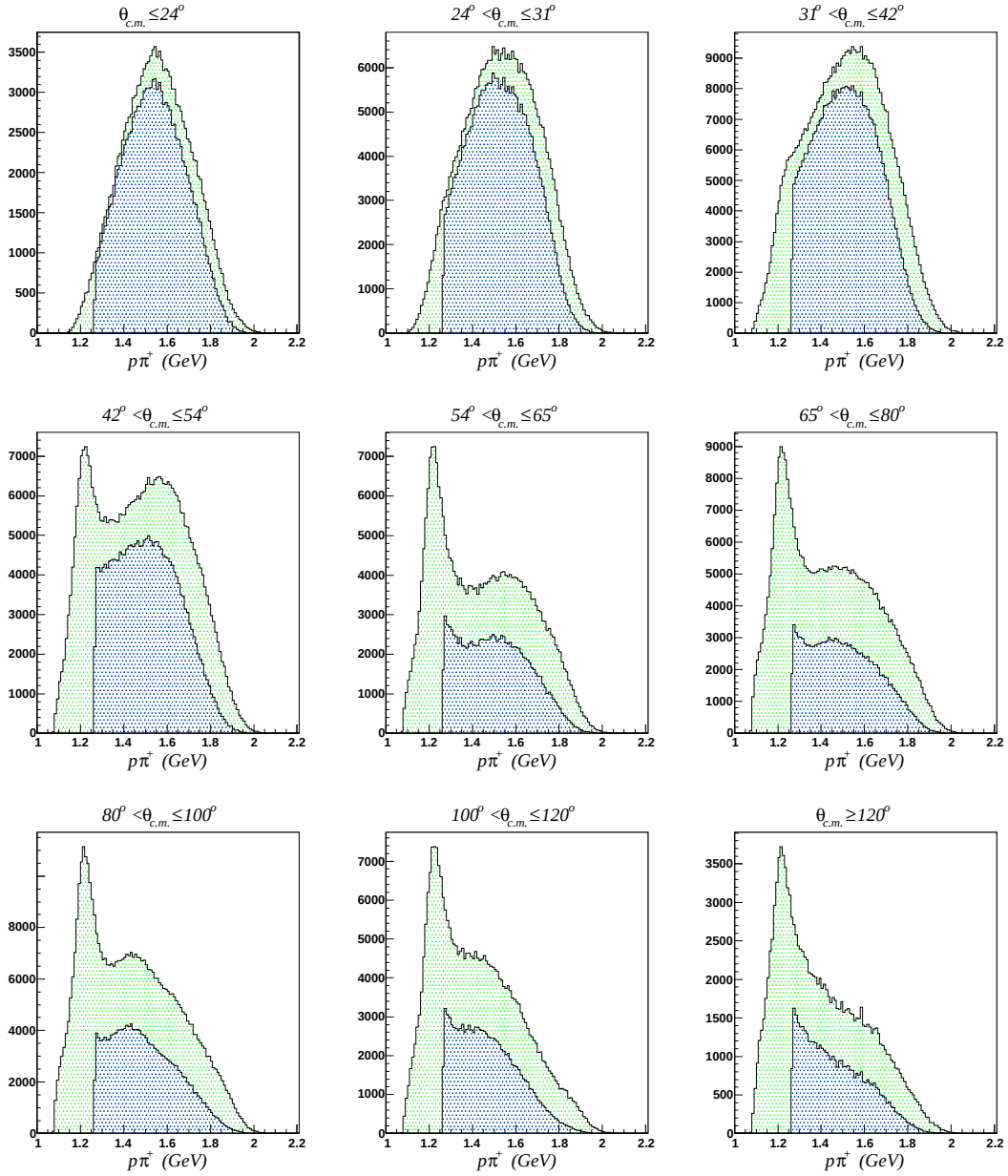

Figure 6.6: The invariant mass spectrum of the $p\pi^+$ pair for the same $\pi^+\pi^-$pair polar angle bins as shown in Fig. 6.5. The blue shaded distributions represent the effects cutting on the invariant masses of the $\pi^+\pi^-$, $p\pi^+$, and $p\pi^-$ pairs to emphasise the ρ^0 signal.

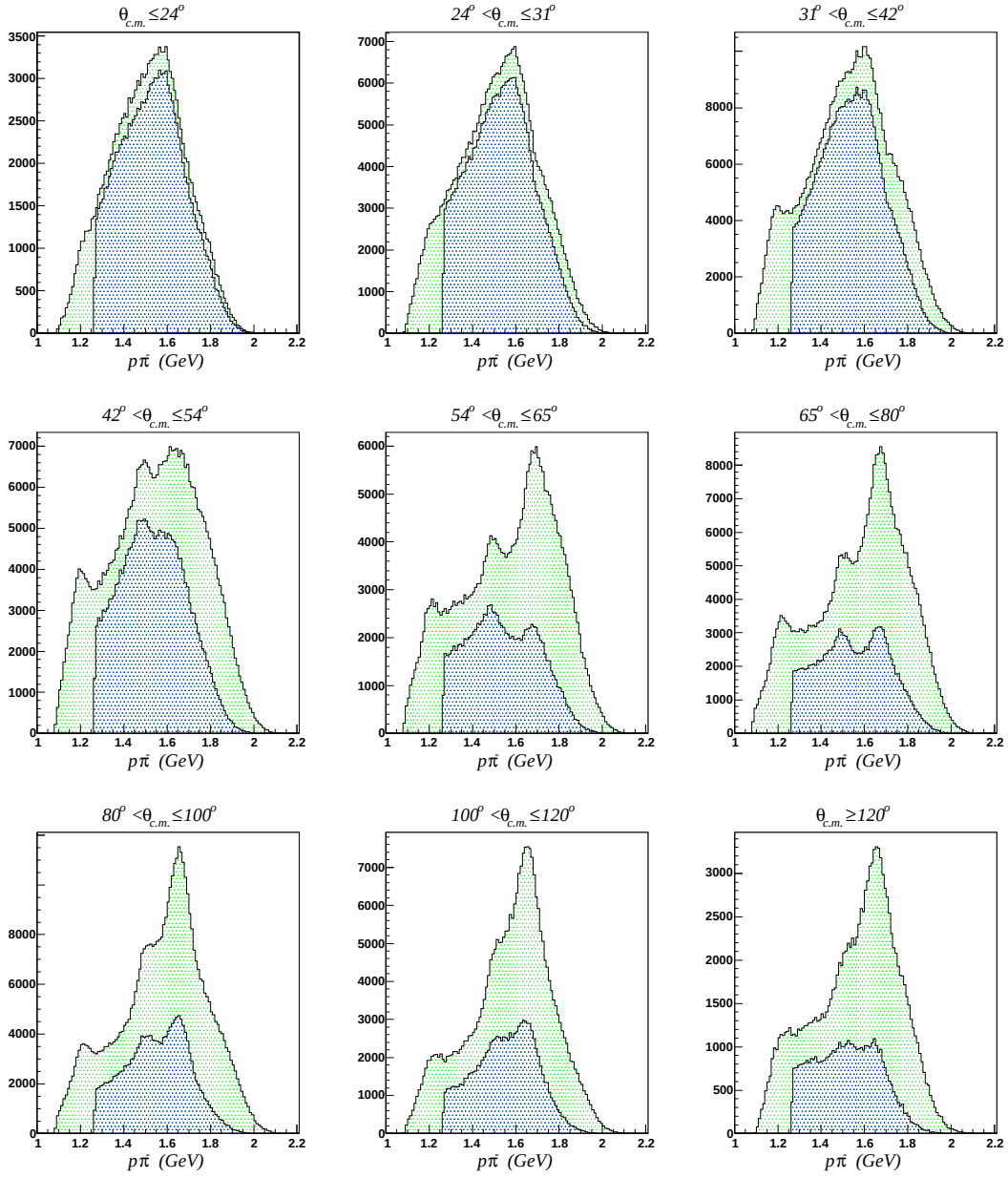

Figure 6.7: The invariant mass spectrum of the $p\pi^-$ pair for the same $\pi^+\pi^-$pair polar angle bins as shown in Fig. 6.5. The blue shaded distributions represent the effects cutting on the invariant masses of the $\pi^+\pi^-$, $p\pi^+$, and $p\pi^-$ pairs to emphasise the ρ^0 signal.

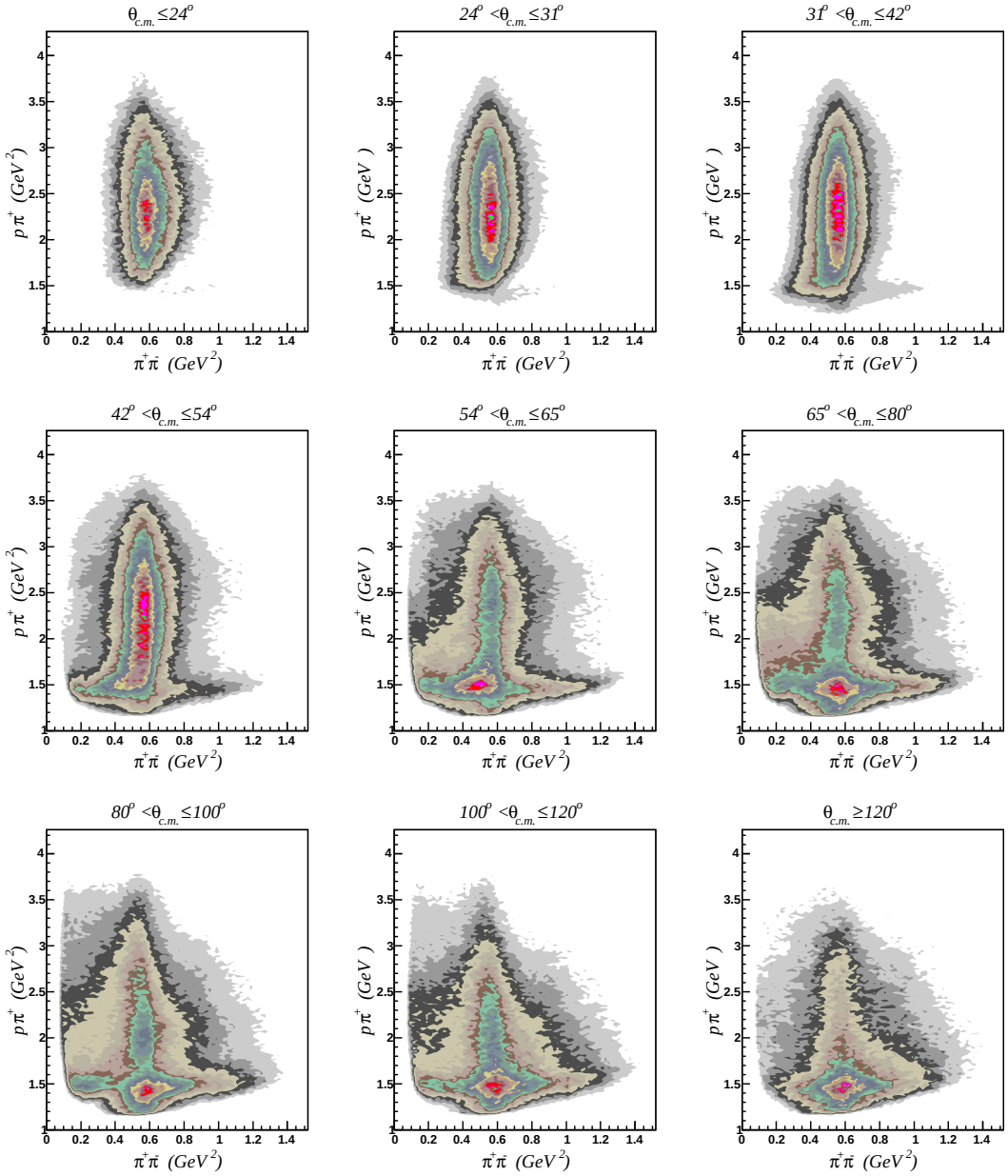

Figure 6.8: Dalitz plots of the $p\pi^+$ and $\pi^+\pi^-$ combinations for the same $\pi^+\pi^-$ pair polar angle bins as shown in Fig. 6.5.

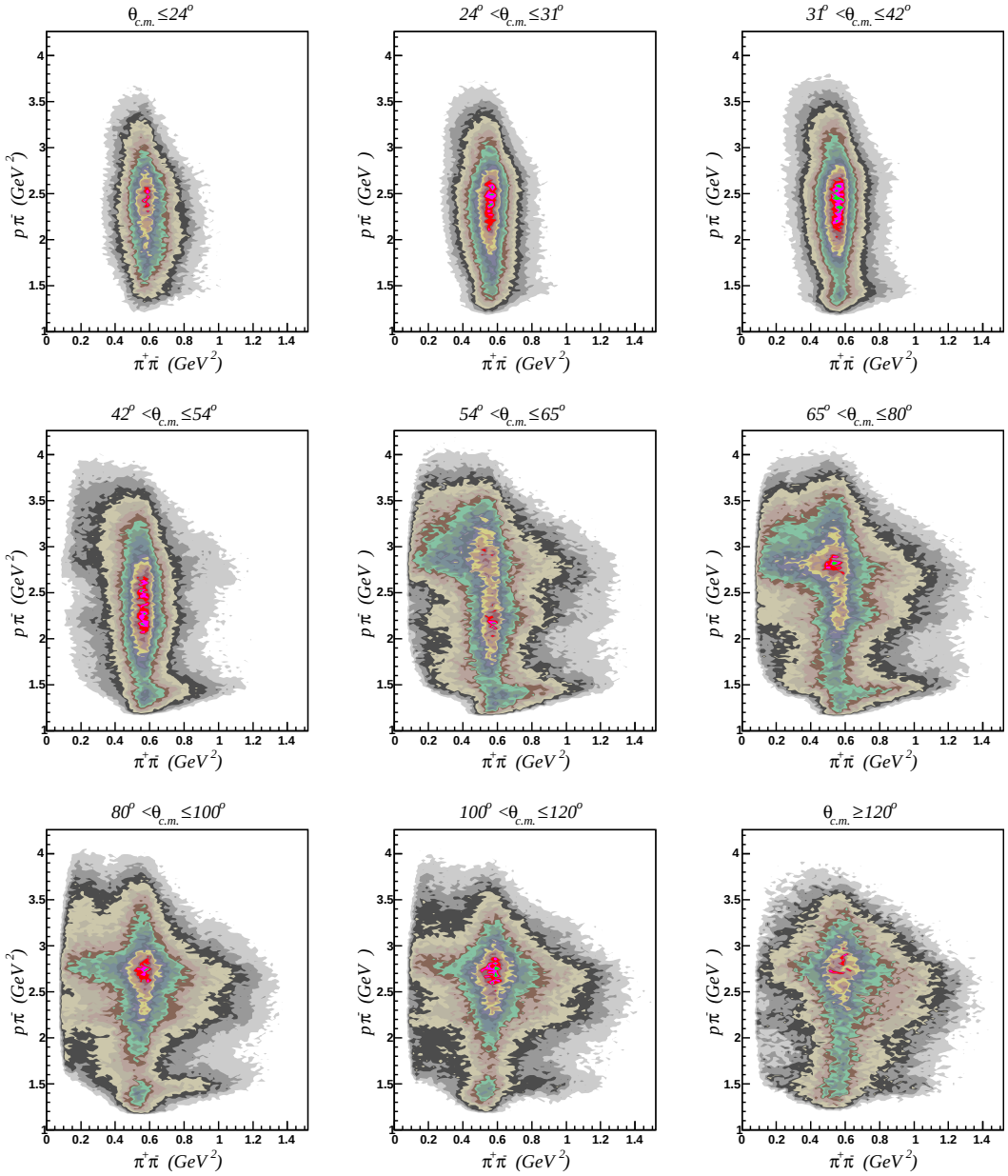

Figure 6.9: Dalitz plots of the $p\pi^-$ and $\pi^+\pi^-$ combinations pair for the same $\pi^+\pi^-$pair polar angle bins as shown in Fig. 6.5.

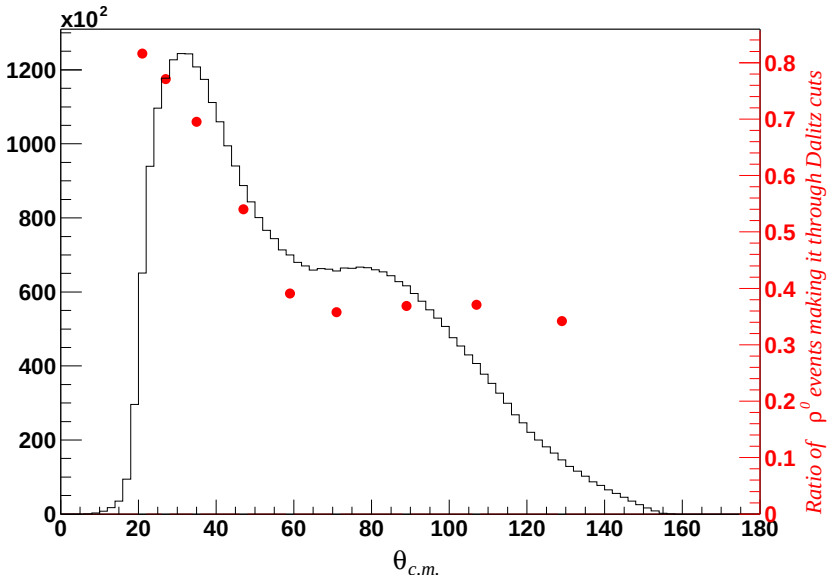

Figure 6.10: The red markers represent the ratio of events surviving the invariant mass cuts (based on Dalitz plots in Fig. 6.4) versus the polar angle of the $\pi^+\pi^-$ pair in the $(\overrightarrow{\gamma}, \mathrm{p})$ c.m. system. The black line is the actual polar distribution of the $\pi^+\pi^-$ pair as shown previously in Fig. 6.4.

sufficient number of events to enable the measurement of the photon asymmetry parameter (Σ) for the $\overrightarrow{\gamma}\mathrm{p} \to \rho^0\mathrm{p}$ channel. The five ranges in $\theta_{\mathrm{c.m.}}$ for which Σ is measured in this study are given in Table 6.1. The remaining four ranges were found to show no sinusoidal behaviour that could be fit using a reasonable parameterisation. This is indicative of other processes interfering with the ρ^0 signal hence the exclusion of these. Also given in this table are the mean values of $\theta_{\mathrm{c.m.}}$ and the corresponding mean values of the momentum transfer to the proton, t.

Bin No.	Range in $\theta_{\mathrm{c.m.}}$ (°)	$\overline{\theta}_{\mathrm{c.m}}$(°)	$\overline{\lvert t \rvert}$ (GeV^2)
1	$\theta_{\mathrm{c.m.}} \leq 24$	21	0.12
2	$24 < \theta_{\mathrm{c.m.}} \leq 31$	27	0.15
3	$31 < \theta_{\mathrm{c.m.}} \leq 42$	36	0.23
4	$42 < \theta_{\mathrm{c.m.}} \leq 54$	47	0.36
5	$54 < \theta_{\mathrm{c.m.}} \leq 65$	59	0.52

Table 6.1: The five bins for which the photon asymmetry is measured in this work. The mean value of the polar angle of the $\pi^+\pi^-$ pair and the mean value of the momentum transfer to the proton are also given for each bin.

6.2 The Acceptance Correction and Detector Stability

In order to extract the effects of the linear polarisation of the photon beam in the $W(\Phi)$ distributions the acceptance and detector efficiencies of the CLAS system must be corrected for. This is the main factor which will limit the accuracy of the measurement of the photon asymmetry as any fit to a *normalised* $W(\Phi)$ distribution will be affected by major fluctuations in the detector systems during data collection, as well as poor statistics. The normalisation process is described in Chapter 2.5. A fit of the form of Eqn. 2.6 in conjunction with knowledge of the average degree of linear polarisation thus enables the photon asymmetry to be determined.

To measure the validity of this method and gain an insight into the systematic effects introduced by CLAS the following investigation has been carried out. The first run-number of the amorphous data set is used as a reference run for which all amorphous data is then compared. For this reference run (run number 29227) a plot of the azimuthal distribution of the detected π^+ for events of interest is obtained. For each successive amorphous run number the same distribution is obtained and then scaled to the number of entries in the reference distribution. This scaled version is then divided through by the reference distribution.

If the detection of π^+ remains constant then a straight line fit to the normalised distribution should cross the y-axis at one. Any major deviation from this would indicate this method of correcting for acceptance is unsuitable. If this were the case then a full simulation using the GSIM [79] package which uses the GEANT [80] routines from the CERN libraries as a framework for a Monte Carlo simulation of the CLAS detector would be necessary. With the large amount of time and expertise required for the GSIM method to be completed successfully it is unfortunately beyond the reach of this work. However, an example of the normalisation method for run number 29545 is shown in Fig. 6.11. This data was taken 21 days after the reference data. It can be seen that the acceptance for π^+ particles has changed very little over this period of time. Similar results are to be found for the proton and π^- particles and so it can be said that this method has been proved valid.

The particle acceptance study as described above has been repeated for the two sets of polarised data being analysed, the set where the coherent edge was set to 2.0 GeV (reference run number is 29256), and the set where the coherent

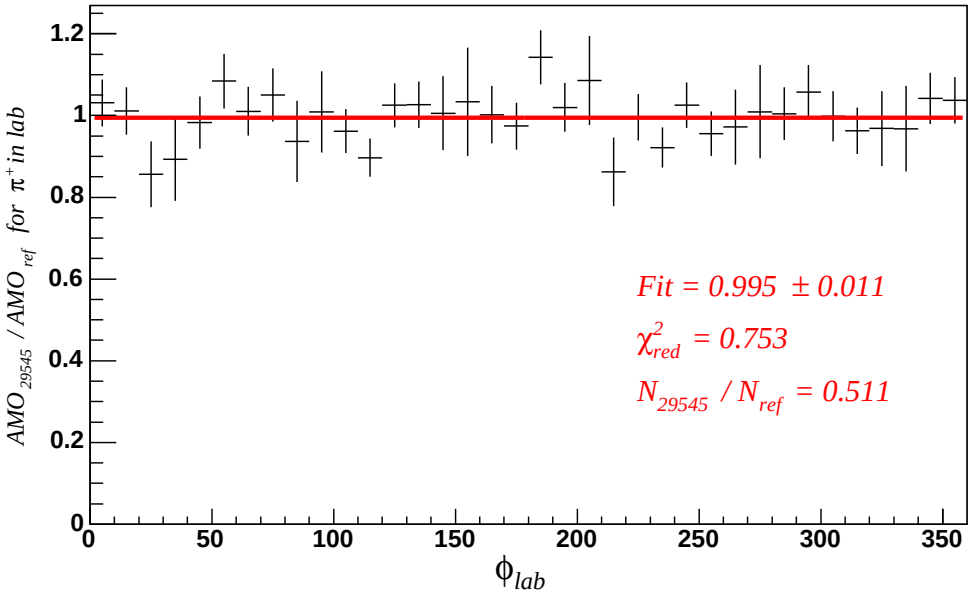

Figure 6.11: The azimuthal distribution in the lab frame of the π^+ particles from events of interest only is obtained from run 29545, then normalised to the same distribution obtained from a reference run. The reference data was taken 21 days previously and the straight line fit shows that the CLAS acceptance for π^+ particles can be considered constant. The larger error bars at $30-40^\circ$ (and then $90-100^\circ$ etc...) are due to areas of no acceptance in the CLAS detector due to the position of the torus coils.

edge was set to 2.2 GeV (reference run number is 29467). A representation of the information obtained for all three data sets is shown in Fig. 6.12. It can be seen that on average the acceptance remains stable with respect to the appropriate reference run to better than 2%. The most obvious frailties of the method are as follows;

1. The ratio of amorphous data to polarised data is approximately 1 : 17.5 (based only on the number of runs this becomes 1 : 6, but this does not take into account the amount of data read out for each run). The statistical errors in the measurent of Σ will therefore be dominated by the amorphous data W (Φ) distributions used in the normalisation process.

2. The amorphous data was taken infrequently over the whole g8a run period. This is not ideal as many short term changes in detector efficiencies may translate into deviations in the sinusoidal behaviour of the normalised W (Φ) distributions.

As this was the commissioning experiment of the linearly polarised beamline in Hall B these points must be noted for future experimental runs. In Chapter 7.2 I discuss the lessons learned from the g8a experiment in more detail. For the analysis on the ρ^0 channel in this thesis however this normalisation method is deemed the most appropriate method applicable within the available time frame.

6.3 Determining the Degree of Photon Polarisation

The degree of linear polarisation of the photon beam is obtained from a set of look-up tables on an event-by-event basis. Although the experiment was set-up to aquire data with the coherent edge at two positions (2.0 and 2.2 GeV), instabilities in the quality and position of the incident electron beam enable the position of the coherent edge to fluctuate. For this reason the first step in producing the look-up tables is to skim through the entire polarised data set, fitting the photon tagger scaler distributions each time an EPICs[2] event has been read-out. An EPICs event typically occurs once every 2000 events and contains scaler, goniometer,

[2]The Experimental Physics and Industrial Control System, EPICS [81], is a set of software tools, libraries and applications used to create the slow control systems for various electronics of the CLAS detector.

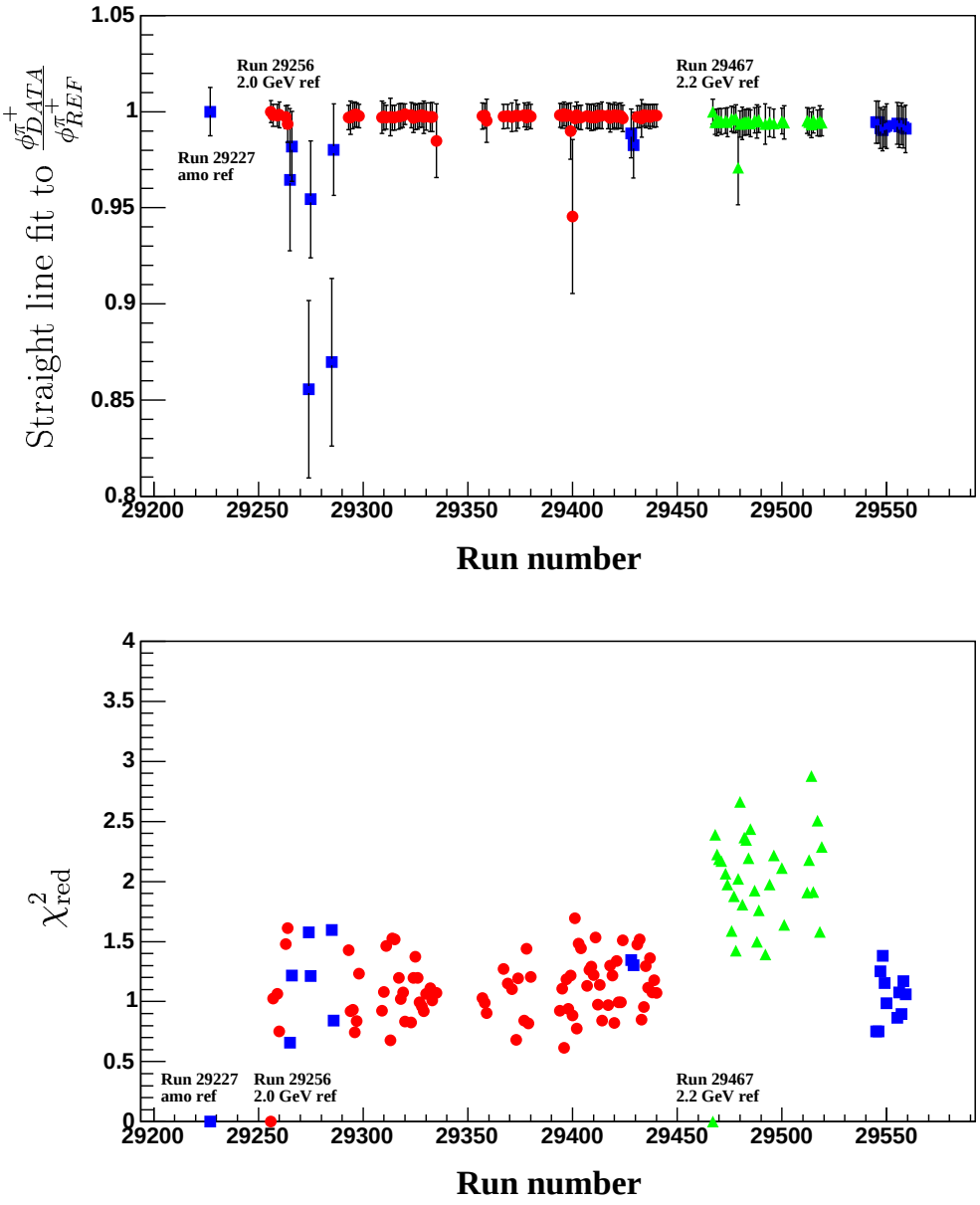

Figure 6.12: As a measure of the stability of π^+ acceptance for all data analysed (see text for a description of the method). Blue points correspond to amorphous data (reference run 29227), red to polarised data with the coherent edge at 2.0 GeV (reference run 29256), and green with the coherent edge at 2.2 GeV (reference run 29467). Top: Straight line fit to normalised azimuthal distribution of π^+ in the lab. The data points which show significant deviation from the norm are a statistical effect due to the very small number of events taken in those runs. Bottom: Reduced χ^2 of fit.

active collimator, and coherent edge information that is not available in the events used for physics analysis. For each run a table of coherent edge position on the T-plane of the tagger versus event number is created to be referenced in the next stage of the procedure. It is assumed that the coherent edge position represents the most accurate value to be used for all physics events leading up to the next EPICs event.

For each coherent edge position a comparison of data for an event with the coherent edge in this position and the anb [48] calculation is made by eye. The anb code is an analytical calculation of bremsstrahlung spectra. The calculation applies an approximate treatment of beam divergence and beam spot size. It also provides the ability to fix several other key parameters which are listed in Table 6.2, along with the typical values used in the calculations for the g8a data.

To begin with many of the initial parameters are known approximately and are used for a first comparison with data. The data comes from two sources, the photon tagger scalers and the TDCs of the photon tagger T-counters. The photon tagger scalers count the number of hits in the E-counter plane for all events originating from the radiator. The scaler distributions for polarised data are divided through by the nearest amorphous data and normalised to make the baseline 100. The plot at the top of Fig. 6.13 shows an example of this.

It should be noted that in order to obtain the agreement in the scaler plot a scaling parameter of ~ 1.5 on the incoherent contribution was required in the anb calculation to give the same amplitude as the scaler data. This is in effect artificially increasing the yield of unpolarised photons tagged by the photon tagger scalers, so although the shape of the spectra agree well the raw amplitudes are different. One possible explanation for this is considered to be that the scalers did not perform to the same level for unpolarised and polarised photon beam running during g8a. For the polarised runs the count rate in the tagger was greater than the during the unpolarised runs. Typically ~ 7.3 hits are reconstructed in the TAGR bank for each event during polarised running, while for unpolarised running this value is ~ 4.7. However, the true reason for this is still unknown and further studies must be carried out into the beam conditions used in the g8a experiment, as well as further assessment of the limitations of the anb calculation.

The second comparison is with the TDC spectra of the T-counters. In this case the photons must have passed through the collimator in order to produce a photon time in conjunction with the CLAS detector system. A random background subtraction is applied to both the polarised and amorphous distributions

Parameter	**Explanation**	**Typical Value for g8a**
Beam energy	Mean energy of the incident beam of electrons, E_γ in MeV.	$E_\gamma = 5734.0\,\mathrm{MeV}$
Energy spread	Width(s) of the beam energy distribution.	0
Crystal orientation	Three crystal angles, θ_c, α_c, and ϕ_c in milliradians.	θ_c and α_c are calculated from the position of the goniometer, $\phi_c = 0.785398\,\mathrm{mrad}$
Beam spot size	Horizontal and vertical beam spot, $Cx_{BeamSize}$ and $Cy_{BeamSize}$ in millimetres.	$Cx_{BeamSize} = 0.045\,\mathrm{mm}$ $Cy_{BeamSize} = 0.045\,\mathrm{mm}$
Beam divergence	Horizontal and vertical beam divergence at the radiator, $Cx_{BeamDiv}$ and $Cy_{BeamDiv}$ in milliradians.	$Cx_{BeamSize} = 0.040\,\mathrm{mrad}$ $Cy_{BeamDiv} = 0.038\,\mathrm{mrad}$
Thickness of radiator	Thickness of the crystal/amorphous radiator, $C_{Thickness}$ in millimetres.	$C_{Thickness} = 0.05\,\mathrm{mm}$
Geometry of collimator	Radiator-to-collimator distance, $C_{ColliDist}$ and the collimator length, $C_{ColliLen}$ both in metres, and the collimator radius $C_{ColliRad}$ in millimetres.	$C_{ColliDist} = 22.9\,\mathrm{m}$ $C_{ColliLen} = 0.30\,\mathrm{m}$ $C_{ColliRad} = 0.7\,\mathrm{mm}$
Incoherent type	The mode of calculating the incoherent intensity (0: Bethe Heitler. 1: Hubbell cross section.	1
Number of lattice vectors	The number of lattice vectors to be used for the calculation.	10
Z of radiators	The charge number of the crystal/amorphous radiator nuclei.	6

Table 6.2: A description of the parameters used by the anb code [48] to carry out an analytical calculation of bremsstrahlung spectra. The typical values used for the calculations with the g8a data are also given.

to subtract those hits on the tagger focal plane which occurred while the timing gate was open, but were not associated with photons which caused a trigger. In this subtraction *real* photons are selected with a fixed timing window on the prompt timing peak. The *random* photons are selected from a window of the same fixed width, but beyond the prompt timing peak.

The random subtracted distribution for the polarised data is then divided through by the random subtracted distribution for the amorphous data, then normalised to make the baseline 100. This distribution is then reproduced with the anb calculation to obtain a linear polarisation versus photon energy map for this particular coherent edge position. The resulting spectra for the collimated beam is narrower as the ratio of coherently scattered photons is increased as can be seen in the middle plot of Fig. 6.13. Unlike the tagger scaler method, when using this method there is no need to use any extra scaling of the incoherent contribution beyond the calculation to obtain a good comparison between the TDC spectra and the anb calculation.

As the coherent edge will move along the T-counter plane during data aquisition, the parameters are altered systematically to obtain the best comparison with the TDC spectra and the anb calculation for each T-counter channel the peak may lie in. A plot of the resulting degree of linear polarisation versus photon energy is then produced for each T-counter channel as shown at the bottom of Fig. 6.13. This distribution is transformed into a polarisation table which can be referenced when applicable with the appropriate function.

As each physics event is analysed the HEAD[3] bank is examined to find out the current run number and the event number within this run. Using this information the tables mapping the history of the coherent edge position then return the value of the coherent edge for this event. The appropriate polarisation table is then opened and a polarisation value is returned which is dependent on the energy of the photon.

6.3.1 Error Estimation for the Polarisation Calculation

Ideally the degree of linear polarisation would be measured by a polarimeter. However, as such a device was unavailable for the g8a run the degree of po-

[3]Every event whether it is an EPICS, physics, or of any other type has a HEAD bank as its first bank (see Chapter 4.1 for the description of a bank). This contains information on the run number, the event number, the event time and type, the read-out-crate (ROC) synchronisation status, the event classification, and the trigger used in aquiring the event.

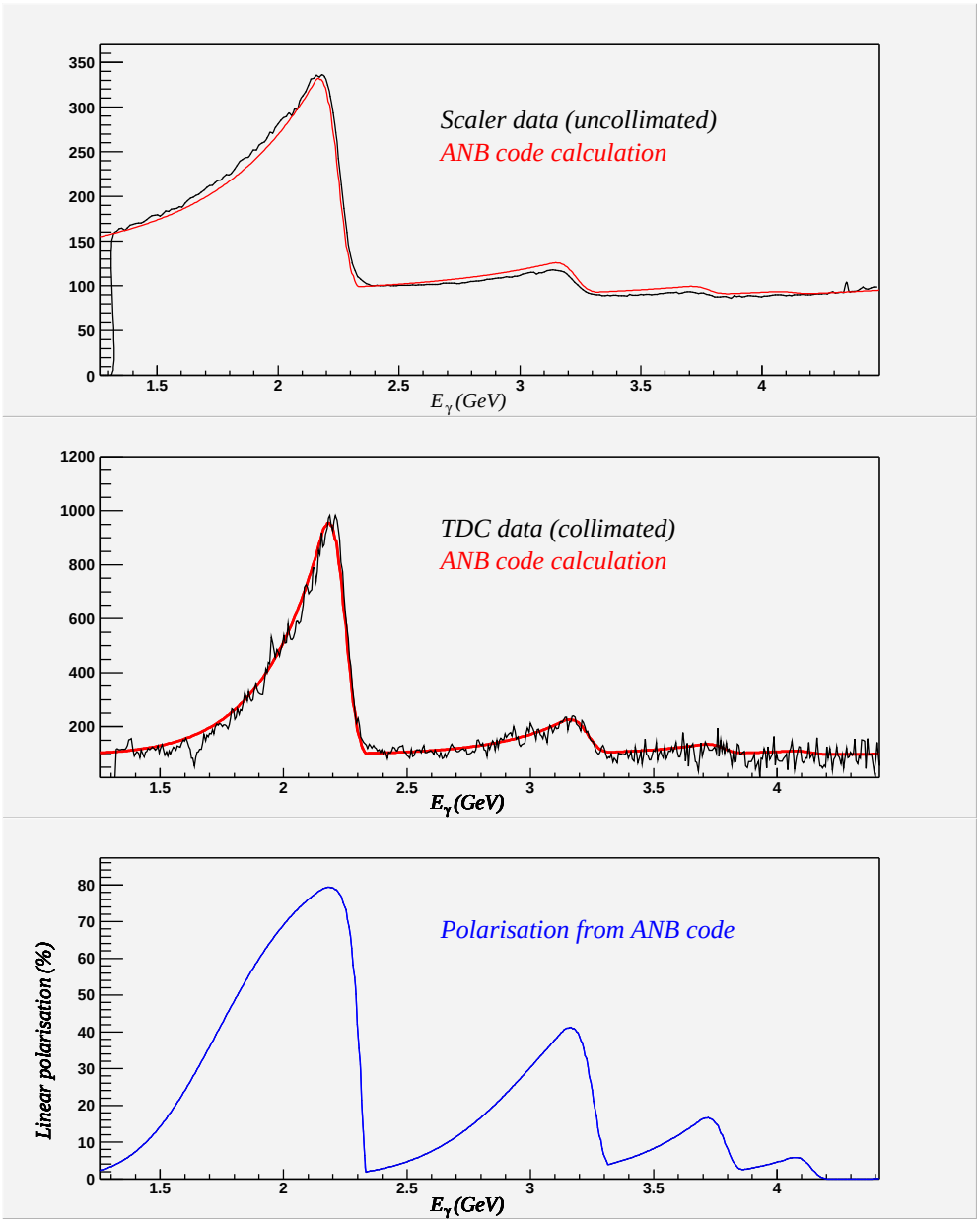

Figure 6.13: An example of how a polarisation table is made for the coherent edge lying at a particular position. Top) Uncollimated tagger scaler data compared with the anb [48] calculation; Middle) Collimated tagger TDC data compare with same calculation method; Bottom) The calculated polarisation versus photon energy distribution.

larisation was obtained using the method as described above. This method of calculating the polarisation introduces a greater degree of uncertainty than using a polarimeter. Using an automated procedure to achieve a good comparison of the anb calculation with the tagger TDC spectra is desirable, but the complexity of the task is such that it has been difficult to implement such a procedure successfully. By choosing an example of a TDC spectrum for each coherent edge position as determined by the initial automated fits of the tagger scalers and then comparing the anb calculation to this by eye, there are several areas where inaccuracies can enter the polarisation tables. These are split into four areas below in order to estimate how accurate the mean polarisation values which are used to calculate the photon asymmetry may be considered.

Dependence on Photon Tagger E-plane

For each event passing all cuts and lying within the photon energy range $1.6 \leq E_\gamma \leq 2.3\,\mathrm{GeV}$, a distribution of the polarisation values for the *best photon* is made for a representative data sample. The best photon is the one which is considered to have caused the hadronic interaction in CLAS. In Fig. 6.14 the mean of this polarisation distribution is shown to be 71 %. Distributions of what the polarisation would be if the true photon lay in several different E-bins before and after the best photon are filled at the same time as for the best photon case. The mean values of these distributions are also plotted in Fig. 6.14.

A clear trend is observed over the range of E-bins studied. It is noted that the maximum appears nearly two E-bins after the best photon. This artefact is thought to be a result of the procedure of comparing the TDC spectra and anb calculation by eye when making the polarisation tables. On average, more than 6 E-bins are associated with each T-bin for which the polarisation tables are constructed. When using a polarisation table for any particular T-bin we consider the maximum amount the coherent edge could actually have been away from the true position at any time is ± 1 T-bin. From looking at the difference between the mean polarisation at the maxima in Fig. 6.14 and ± 1 T-bin away, the maximum uncertainty introduced from this effect is estimated to be $\sim 1.5\%$.

Theoretical and Data Comparison Limits

When comparing the anb calculation to the TDC data for any T-id there is usually a range of parameters which will result in equally good comparisons using the

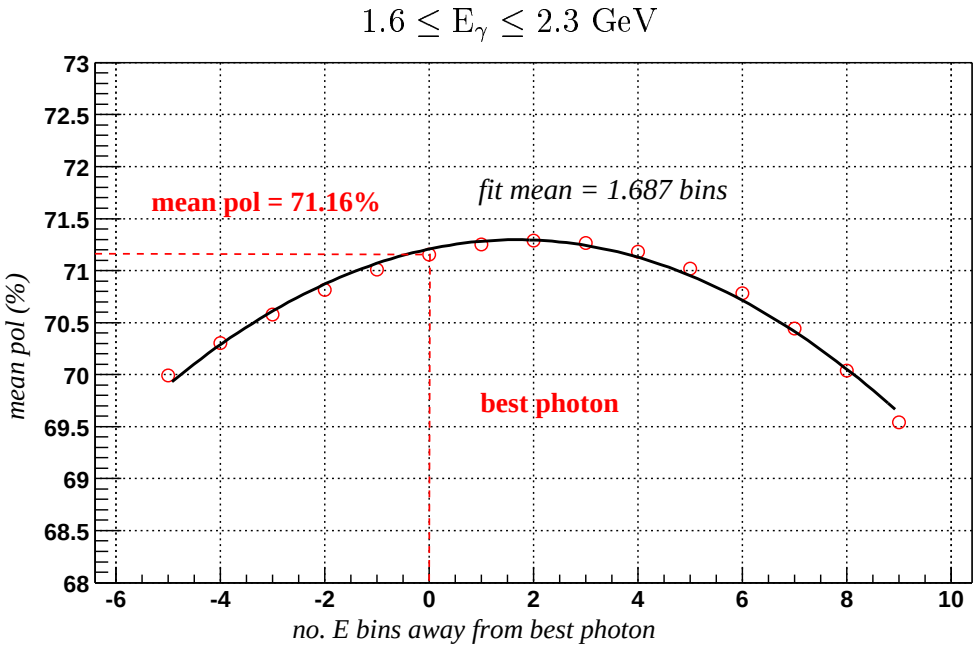

Figure 6.14: A study of the energy dependence of the mean polarisation obtained for events passing through all cuts. For this data sample the "best photon" has a mean polarisation of 71.16 %. The mean polarisation obtained using photons of lower and higher energies is also shown, see text for a more in depth description.

naked eye. This is mainly due to poor statistics for the unpolarised TDC spectra which are used to normalise the polarised TDC spectra. In order to quantify what effect this might have on the uncertainty in the polarisation a T-id is chosen for a particular run and upper and lower limits for acceptable comparisons are obtained. The top and middle plots in Fig. 6.15 show an example of this. The effect is for the polarisation distribution for the lower limit to be slightly broader and to have slightly lower maximum polarisation values in the discrete peak structure.

Over the photon energy range analysed in this work the difference in polarisation is shown to be close to zero for this example as can be seen in the bottom left plot of Fig. 6.15. However, if the range of photon energies for events where the coherent edge position is at one T-id position only is weighted by this difference, then the net effect is considerably larger as can be seen in the bottom right plot of Fig. 6.15. As these limits represent the extreme case of parameter choice to obtain the best comparisons by eye, the average effect of this uncertainty is estimated to be $\sim 2.3\%$.

Varying Height of the Coherent Peak

For an event in any given run the position of the coherent edge on the T-plane of the tagger is obtained from a look-up table and the corresponding polarisation table is then referenced. However, due to instabilities in the position of the electron beam the height of the coherent peak can vary, and hence the polarisation of photons under the peak will change. In Fig. 6.16 the tagger TDC spectra are shown for all runs where the coherent peak has been determined by the fit procedure used during the initial skim of the entire data set to lie at T-id=95. In can be seen that for run 29501 the coherent peak is of poor quality. Events in this case will still pass through the analysis using a polarisation table which was most likely to have been produced using a higher quality spectrum. As all of the polarisation tables were created using better quality TDC spectra than the example shown for run 29501, the polarisation value of the photons for such cases can be seen to be overestimated by a maximum of $\sim 5.0\%$.

Uncertainty from TDC Spectra Normalisation

The TDC spectra which are compared to the anb calculation are normalised in such a way that the baseline is set to be equal to 100. A region of photon

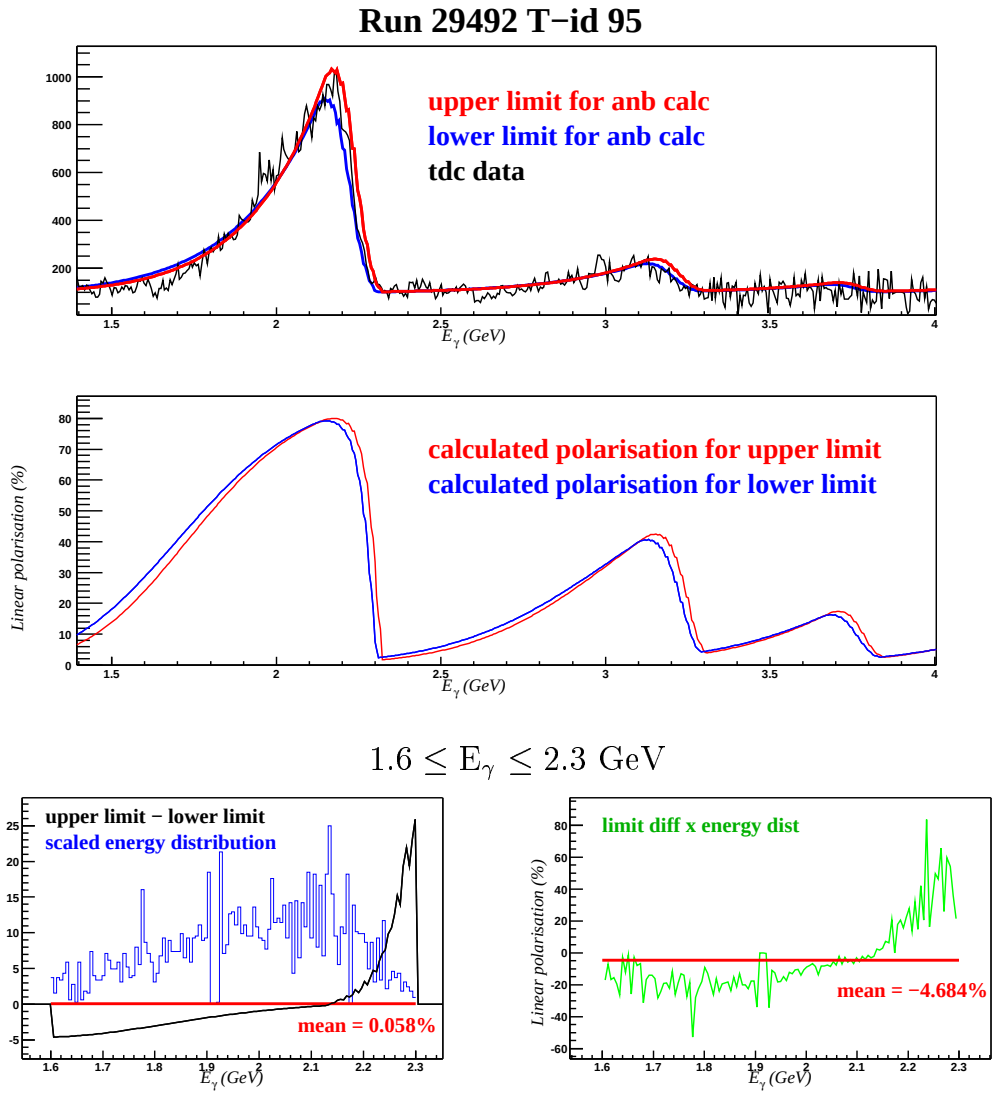

Figure 6.15: Top) The tagger TDC data (black) the upper and lower limits (red and blue respectively) which might be used in constructing a polarisation table for T-id 95. Middle) The polarisation tables obtained from the anb code for the upper and lower limits. Bottom left) The difference between the polarisation for both limits (black) and a scaled energy distribution for events where the coherent edge is at T-id=95 (blue). Bottom right) The polarisation difference multiplied by the scaled energy distribution.

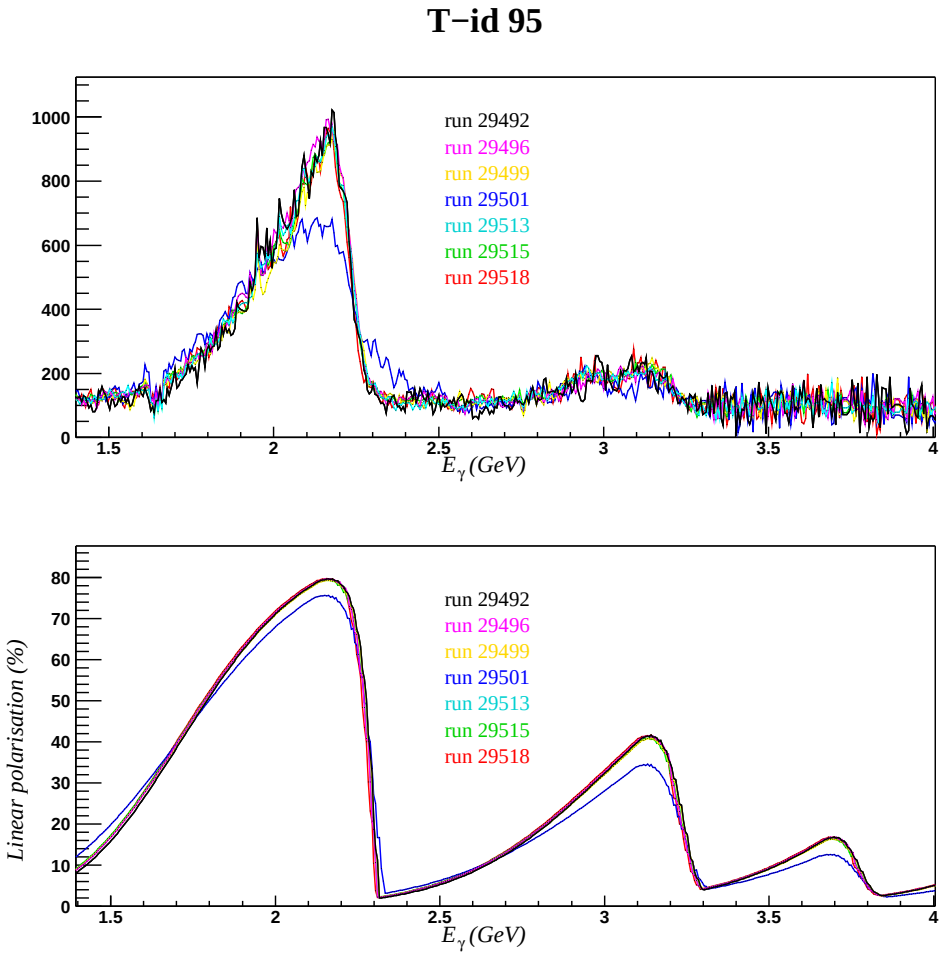

Figure 6.16: Top) The tagger TDC spectra for all runs with the coherent edge positioned at T-id=95. Bottom) The corresponding polarisation from the fits of the above TDC spectra.

energies is chosen where there should be no coherent enhancement. An average count for this region is then obtained and from this the scaling parameter to set the average to be 100 is obtained. Due to the spikiness of the TDC spectra this scaling procedure can produce different normalised spectra depending on which energy region is selected to calculate the average.

Fig. 6.17 shows an example of two different photon energy regions used to calculate the scaling parameter. It can be seen that the plot using the higher energy range ($\sim$ 100 channels after the fourth coherent peak) results in a greater peak to baseline ratio than the one with the lower energy range ($\sim$ 40 channels just after the first coherent peak). However, the relative shape of the spectrum remains almost identical and hence the polarisation tables created from each method do not vary to any great degree. The spectra which were compared to the anb calculations were obtained from using the upper photon energy range. From looking at the difference between the two polarisation tables over the photon energy range of interest, the maximum potential error from this choice is estimated to be $\sim 0.5\%$.

Conclusion

The effect of the varying height of the coherent peak can only reduce the average degree of linear polarisation which is used to calculate the photon asymmetry. The measured asymmetries as calculated from the fitting procedure (described in Chapter 6.4) can therefore be corrected for this effect. It is estimated that the case where the coherent peak has a lower height occurs 10% of the time throughout the data set. Using this with the previously stated value of the maximum overestimation of 5% the correction is carried out as shown in Eqn. 6.1.

$$\Sigma_{\mathrm{cor}} = \Sigma_{\mathrm{calc}} \left(1 + (0.1 \,\mathrm{x}\, 0.05)\right) \tag{6.1}$$

The errors for the three other effects are added linearly to give an overall estimate for the systematic error associated with the calculation of the polarisation to be $\pm 4.3\%$.

6.4 The Photon Asymmetry

The photon asymmetry (Σ) for the ρ^0 is measured here for the ranges in $\theta_{\mathrm{c.m.}}$ of the $\pi^+\pi^-$ pair in the $(\overrightarrow{\gamma}, \mathrm{p})$ c.m. system as stated in Table 6.1. All of the polarised data taken with the coherent edge positioned at 2.0 and 2.2 GeV are merged

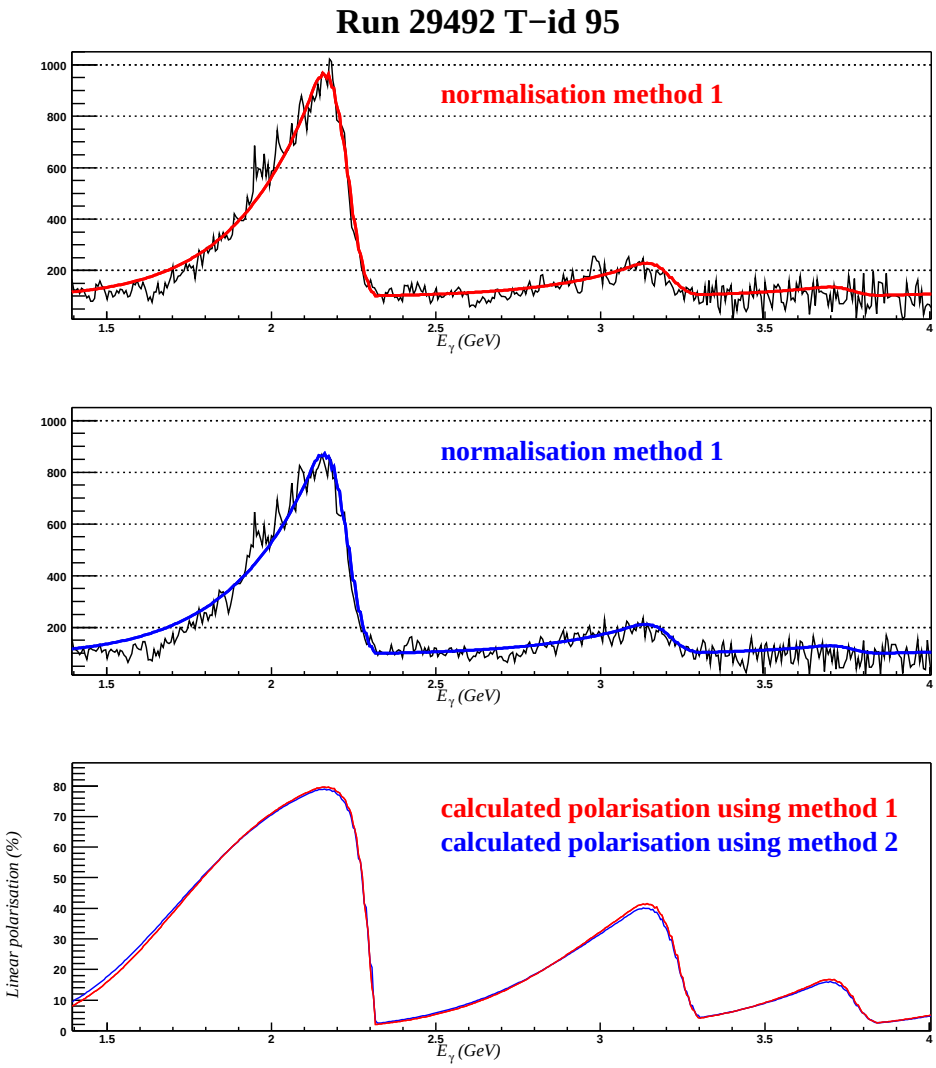

Figure 6.17: Top) A normalised tagger TDC spectrum using the 100 channels after the fourth coherent peak to find the scaling parameter to make the baseline equal to 100. Bottom) A normalised tagger TDC spectrum using the 40 channels after the first coherent peak to find the scaling parameter to make the baseline equal to 100.

into one data set and normalised as described previously using the complete set of unpolarised data. Only events lying in the photon energy range $1.6 \leq E_\gamma \leq 2.3\,\text{GeV}$ are used for both the polarised and unpolarised data. For the polarised data an additional limit on the degree of linear polarisation is imposed such that $\gamma_{\text{pol}} \geq 10\%$.

The distributions of both $\overline{E_\gamma}$ and $\overline{\gamma_{\text{pol}}}$ for all events making it through the cuts for the five $\theta_{\text{c.m.}}$ ranges analysed are shown in Figs. 6.18 and 6.19. As explained in the last paragraphs of Chapter 6.1, the remaining four ranges were found to show no sinusoidal behaviour that could be fit using a reasonable parameterisation. For the ranges analysed the mean photon energy for the sum of these is $\overline{E_\gamma} = 1.90\,\text{GeV}$, and the mean polarisation for the sum is $\overline{\gamma_{\text{pol}}} \simeq 71.38\%$. The $W(\Phi)$ distributions are shown in Figs. 6.20 to 6.24 and fitted using the parameterisation shown in Eqn. 6.2.

$$W(\Phi) = a\left(1 - \frac{b}{a}\cos 2(\Phi + \alpha)\right) \tag{6.2}$$

where a represents the baseline of the distribution (which should be equal one), $b = P_\gamma \Sigma$, and α is a constant which reflects the offset between the goniometer coordinate system and the CLAS coordinate system. A summary of the results are shown in Tables 6.3 and 6.4. These have provided the first measurements [82] of Σ for the ρ^0 in the range $\theta_{\text{c.m.}} \leq 65°$. The measurements are compared with the predictions of the quark model of Zhao in Chapter 7 of this thesis.

Bin No.	Range in $\theta_{\text{c.m.}}$ (°)	N_{pol}	N_{unpol}	$\overline{P_\gamma}$ (%)	$\Sigma^* \pm \sigma_{\text{stat}} \pm \sigma_{\text{sys}}$
1	$\theta_{\text{c.m.}} \leq 24$	108,746	4,602	72.08	$0.096 \pm 0.027 \pm 0.004$
2	$24 < \theta_{\text{c.m.}} \leq 31$	210,611	9,136	71.46	$0.289 \pm 0.020 \pm 0.012$
3	$31 < \theta_{\text{c.m.}} \leq 42$	294,546	12,795	71.31	$0.354 \pm 0.017 \pm 0.015$
4	$42 < \theta_{\text{c.m.}} \leq 54$	183,882	8,048	71.07	$0.339 \pm 0.021 \pm 0.015$
5	$54 < \theta_{\text{c.m.}} \leq 65$	95,363	4,339	71.17	$0.182 \pm 0.027 \pm 0.008$
6	$65 < \theta_{\text{c.m.}} \leq 80$	114,708	5,073	-	-
7	$80 < \theta_{\text{c.m.}} \leq 100$	144,104	6,601	-	-
8	$100 < \theta_{\text{c.m.}} \leq 120$	86,398	4,086	-	-
9	$\theta_{\text{c.m.}} > 120$	34,308	1,552	-	-
Total	-	1,272,666	56,232	-	-

Table 6.3: Summary of results. Σ^* is the corrected value of the asymmetry as described in Chapter 6.3.1. The systematic error is $\pm 4.3\%$ which is purely associated with the calculation of the polarisation. All other systematics are assumed to cancel during the normalisation procedure.

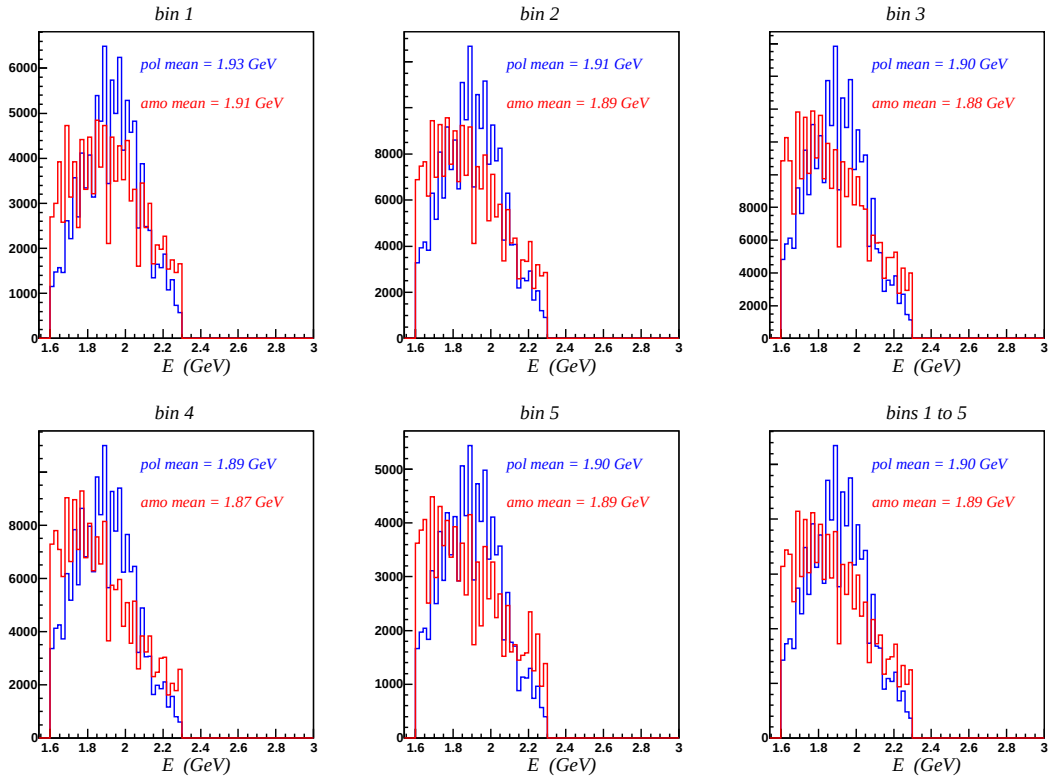

Figure 6.18: The mean photon energy distributions for the polarised and unpolarised data (blue and red respectively) for each of the five $\theta_{\mathrm{c.m.}}$ ranges analysed in this work. The bottom right plot shows the sum of these.

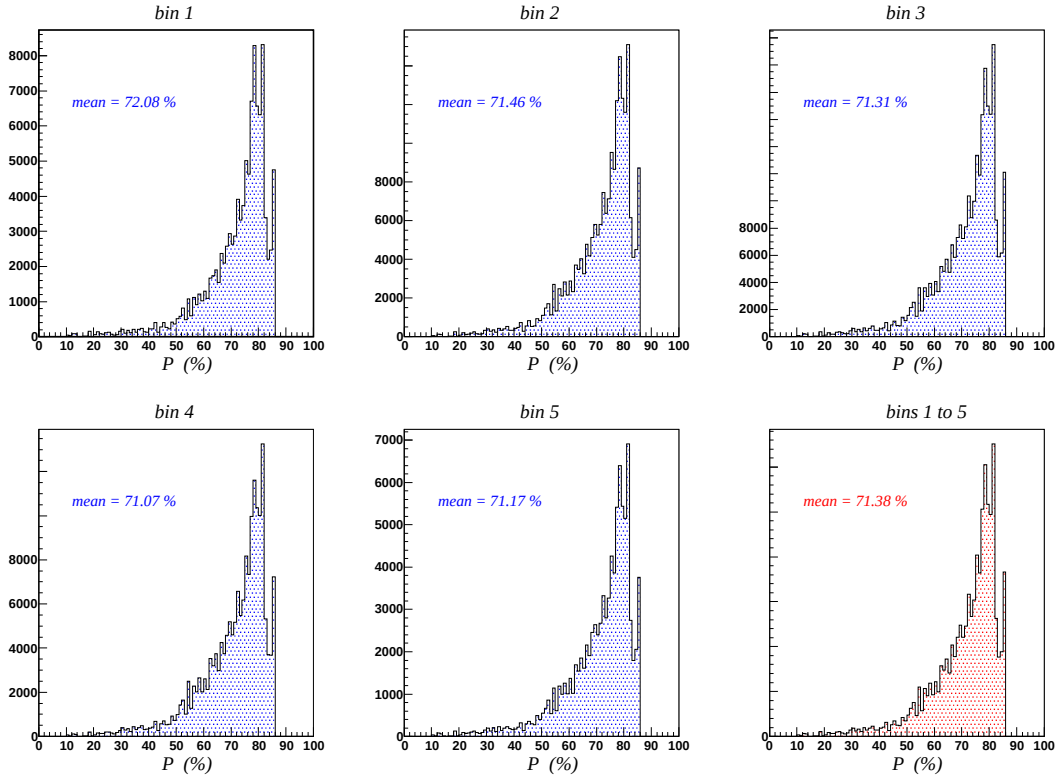

Figure 6.19: The mean photon polarisation distributions for each of the five $\theta_{\mathrm{c.m.}}$ ranges analysed in this work. The bottom right plot shows the sum of these.

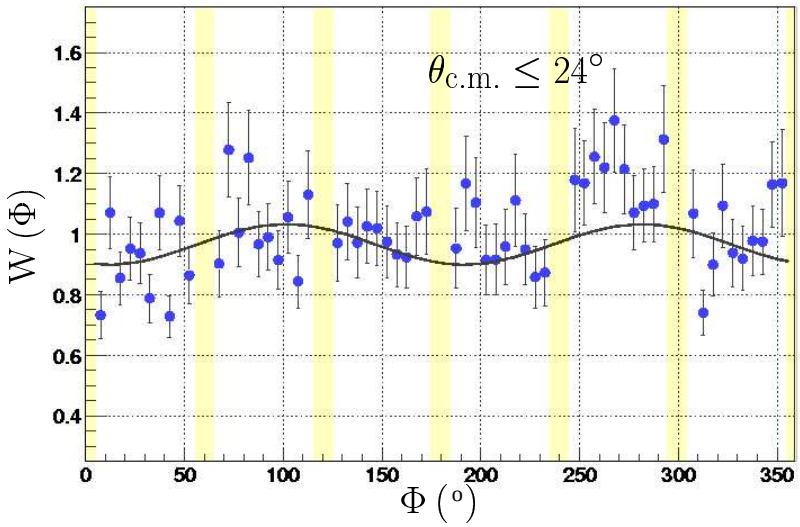

Figure 6.20: The photon asymmetry measurement for bin number 1. The highlighted regions represent the areas of no acceptance due to the torus coils of the CLAS detector.

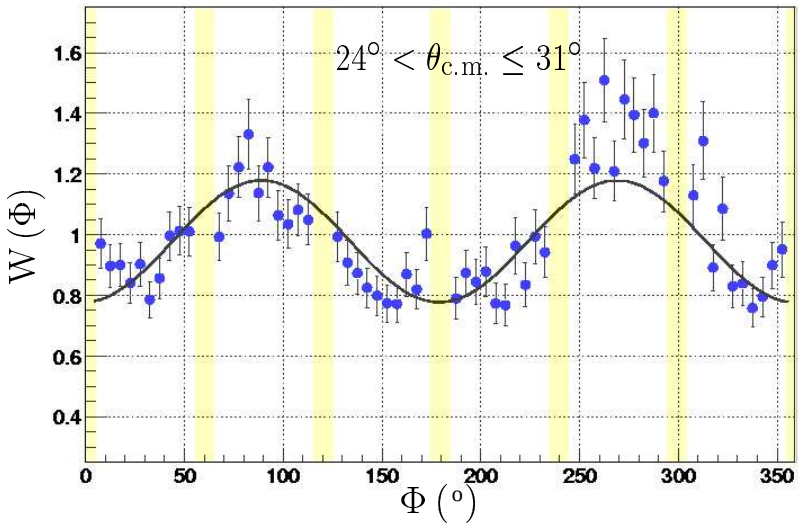

Figure 6.21: The photon asymmetry measurement for bin number 2. The highlighted regions represent the areas of no acceptance due to the torus coils of the CLAS detector.

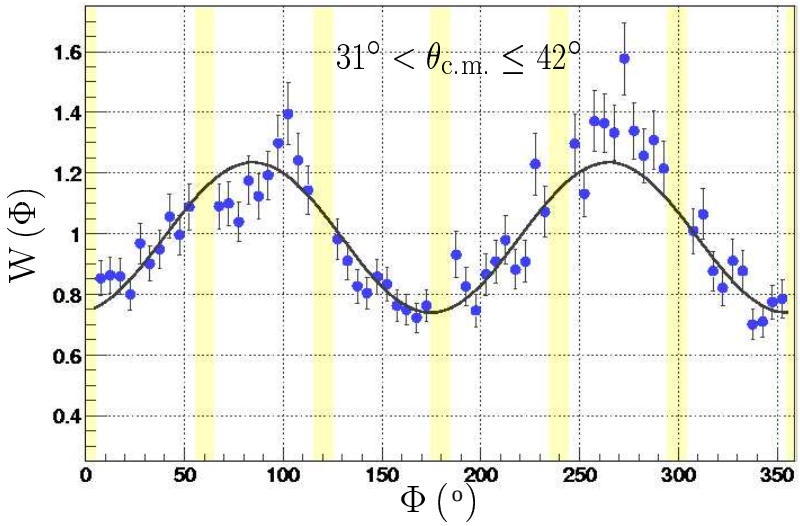

Figure 6.22: The photon asymmetry measurement for bin number 3. The highlighted regions represent the areas of no acceptance due to the torus coils of the CLAS detector.

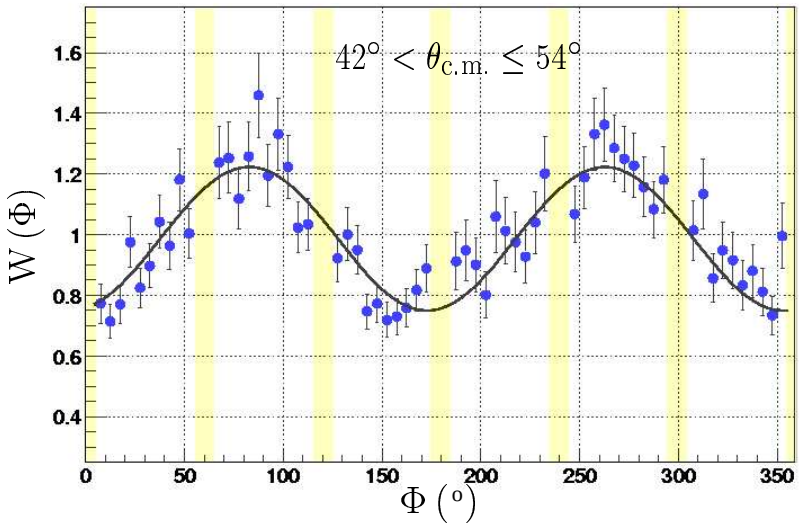

Figure 6.23: The photon asymmetry measurement for bin number 4. The highlighted regions represent the areas of no acceptance due to the torus coils of the CLAS detector.

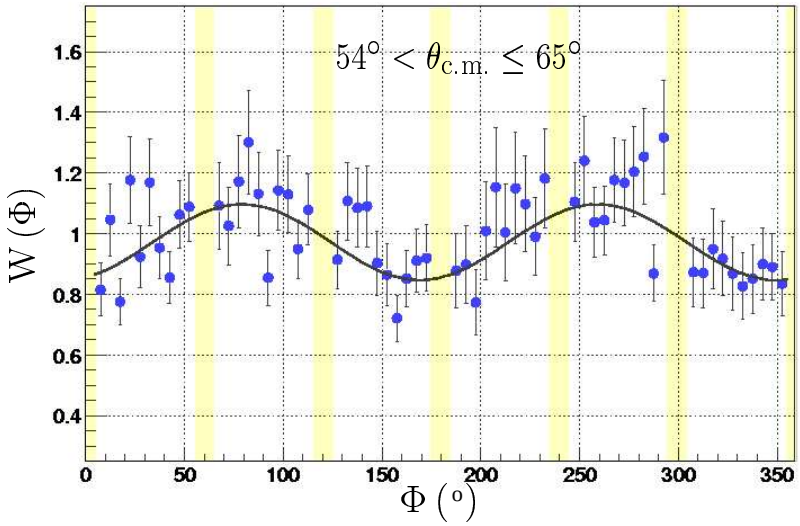

Figure 6.24: The photon asymmetry measurement for bin number 5. The highlighted regions represent the areas of no acceptance due to the torus coils of the CLAS detector.

Bin No.	χ^2_{red}	a$\pm\sigma_{\rm stat}$	b$\pm\sigma_{\rm stat}$	$\alpha\pm\sigma_{\rm stat}$ (°)
1	1.416	0.966 ± 0.015	0.066 ± 0.021	-11.570 ± 18.09
2	1.654	0.978 ± 0.011	0.201 ± 0.016	1.122 ± 4.11
3	1.390	0.987 ± 0.013	0.248 ± 0.013	5.409 ± 2.98
4	1.022	0.986 ± 0.012	0.237 ± 0.017	7.338 ± 3.84
5	0.886	0.972 ± 0.015	0.125 ± 0.021	10.954 ± 9.99

Table 6.4: A summary of the parameters obtained after fitting the W (Φ) distributions. All errors are those obtained from the fitting procedure.

Chapter 7

Discussion and Conclusions

7.1 Comparison with the Quark Model

The measurements of the photon asymmetry (Σ) from the analysis as described in Chapter 6.4 are compared with the quark model [7] in Fig. 7.1. It can be seen that at forward angles the same sign and a similar trend are found when comparing the data to the Σ prediction using the same $\left(\mathrm{a},\ \mathrm{b}'\right)$ parameterisation as the ω. However, the magnitude of the measured asymmetry is approximately two times greater in magnitude than this prediction.

The limitations of extracting a clean ρ^0 signal at $\theta_{\mathrm{c.m.}} \geq 60^\circ$ without a more vigorous analysis prove restrictive on any final conclusions. The most obvious point to take from the comparsion is that tensor coupling of the ρ^0 is clearly very different to that of the ω, and probaby much larger in magnitude [30].

However, with the large amount of exclusive $\overrightarrow{\gamma}\mathrm{p} \rightarrow \rho^0\mathrm{p} \rightarrow \pi^+\pi^-\mathrm{p}$ events available in the g8a data set there remains the possibility of future analysis within the g8 collaboration to extract the spin density matrix elements to a degree of accuracy previously unmatched. To make these measurements the angular decay spectrum of the $\pi^+\pi^-$ decay must be obtained in the ρ^0 rest frame, with the choice of spin quantisation axis determining the reference frame (see Chapter 2.4). In the transformation from the laboratory frame to a frame such as the helicity frame the method of normalisation used in this analysis becomes unusable because of the holes in the CLAS detector acceptance. A full Monte-Carlo acceptance correction using the GSIM [79] package will be required to make this transformation.

With the measurement of the spin density matrix elements of the ρ^0 it will be possible to extract new information on the missing resonances. Fig. 7.2 shows

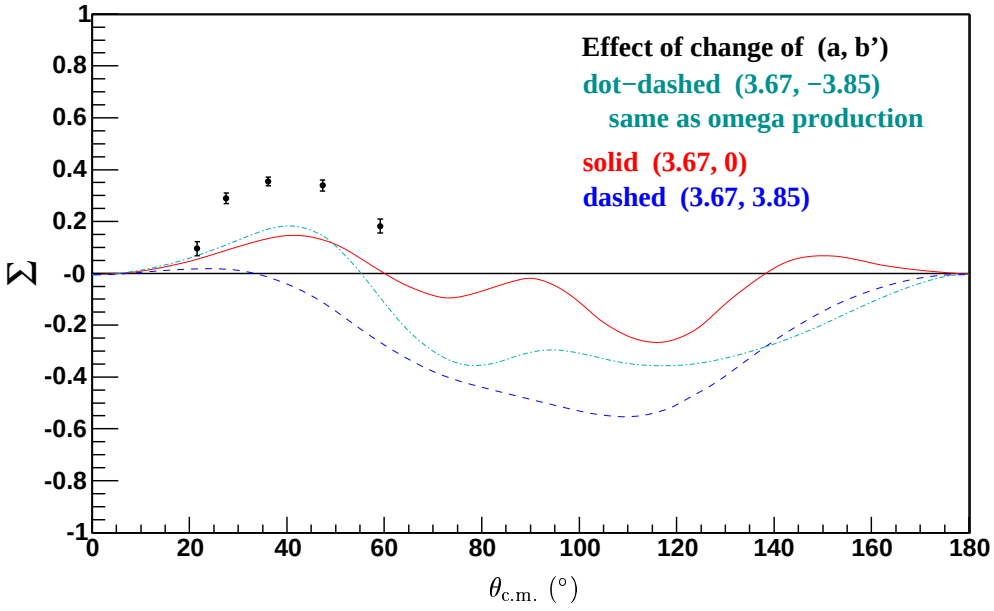

Figure 7.1: Comparison of the measured photon asymmetries with the quark model prediction. The error bars represent statistical errors only and the points lie at the mean point of the asymmetric $\theta_{\text{c.m.}}$ bins as shown in Fig. 6.4. While the trend for the asymmetry of the ρ^0 can be seen to agree with that of the ω, the amplitude is $\sim$ twice as great which suggests the tensor coupling is quite different for the ρ^0.

the prediction of Roberts [16, 83] for two of the spin density matrix elements. The dashed line is for only one missing resonance included in the calculation, the dash-dotted line for all but one of the missing resonances included, and the dotted line for all missing resonances to be included. The sensitivity of these two spin density matrix elements to the presence of the missing resonances can be seen from these predictions. This highlights how important such a measurement will be for our understanding of baryon spectroscopy.

7.2 Recommendations for Future Linear Polarised Photon Beam Running at JLab

As the g8a experiment was the commissioning experiment of the polarised source of photons in Hall B of JLab there were many lessons learned that will benefit the future running of such experiments at the laboratory. In this Chapter I will briefly highlight the lessons learned by the g8a group which should lead to a more streamlined experiment, and therefore leave more time available for physics analysis.

1. **Increased amorphous data acquisition**
   From Fig. 6.12 it is apparent that there was neither an adequate amount of amorphous data acquired relative to the amount of polarised data, nor was the amorphous data taken at regular intervals to better represent any drifts in the experimental detector systems. In future running it would be advisable to prioritise this alongside the polarised beam running as the accuracy of the calculation of the polarisation is highly dependent on this. It should be noted that in previous experiments at Mainz an amorphous data set would be created by adding together two sets of data with the planes of polarisation separated by 90° in the azimuthal plane. A small amount of data using an amorphous radiator would also be taken in this case to provide a check of systematics. However, as explained below in suggestion 3, there were problems with one of the two orientations of the polarisation plane in the g8a data which removed this method as a possibilty.

2. **Online calibration and detector monitoring**
   The offline calibration of the g8a data was a painful process spanning almost one year. During this time many problems where encountered which could

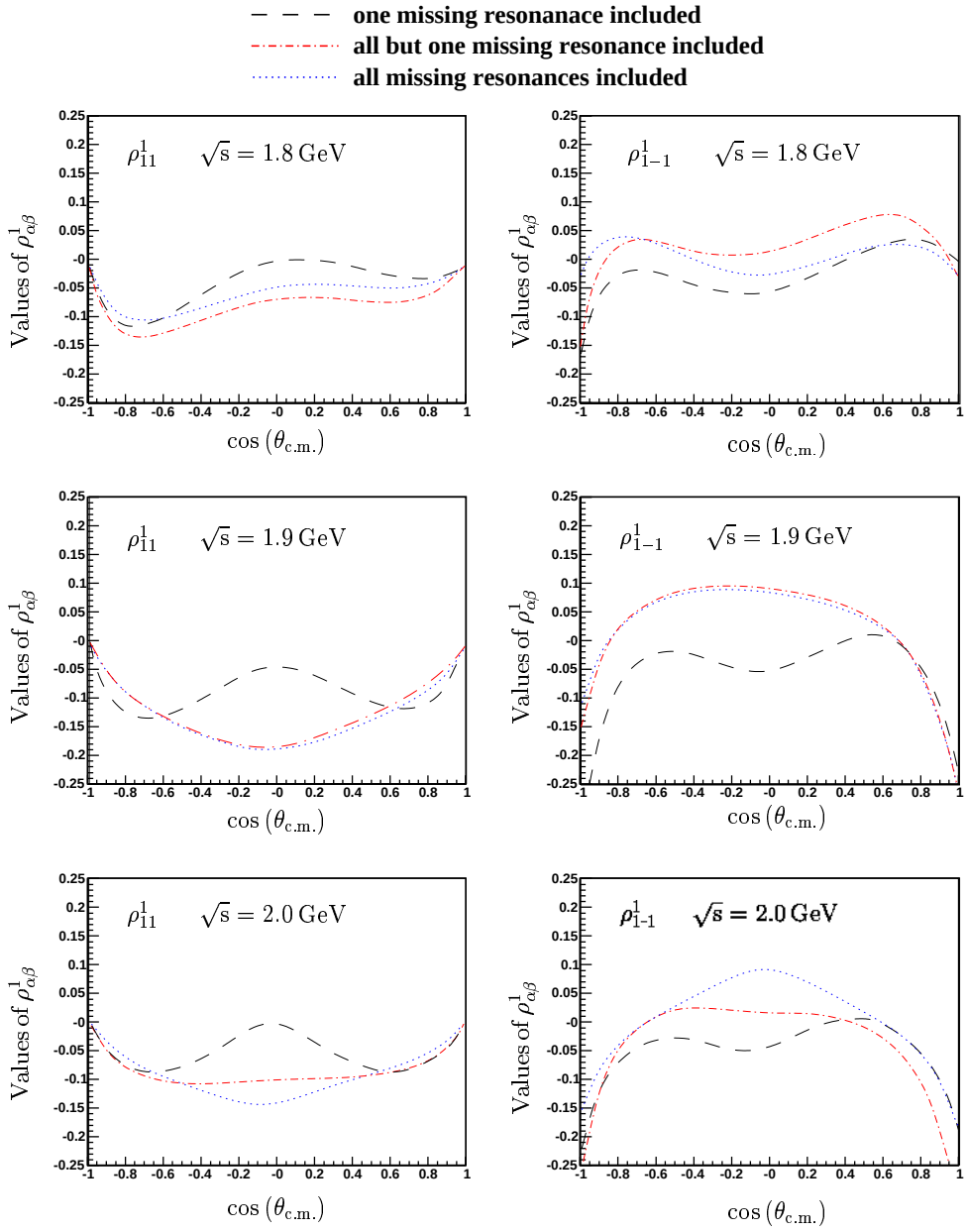

Figure 7.2: The prediction of Roberts [16, 83] for two of the spin density matrix elements of the ρ^0 . The dashed line is for only one missing resonance included in the calculation, the dash-dotted line for all but one of the missing resonances included, and the dotted line for all missing resonances to be included. $\theta_{\mathrm{c.m.}}$ is the polar angle of the π^+ in the $(\overrightarrow{\gamma}, \mathrm{p})$ c.m. frame.

have been prevented during experimental running if some approximate calibrations where carried out during this time. The online monitoring of detector stability, in particular the photon tagger and the goniometer which are two of the most important components of polarised beam running, is highly advisable in order to maximise the possible timing accuracy.

3. **Circular incident electron beam**
   The incident electron beam from the accelerator in JLab provides a beam of electrons which is slightly elliptical in the x-y-plane. It would be desirable for a method of focusing this beam to be circular before striking the diamond radiator which is orientated by the goniometer. The problem was intensified for the g8a run as one of the beam steering coils was downstream of the goniometer. A new coil has been installed upstream of the goniometer and this should improve the beam quality for future runs. The divergence of the incident electron beam in the y-axis is thought to be responsible for the data taken with the plane of polarisation lying in the y-z-plane (known as *parallel* as this plane is parallel to the Hall B floor in the laboratory frame) to be very unstable and of poor quality.

4. **Use a thinner diamond radiator**
   The polarised data that has been used in the physics analysis of the g8a data has all come from data acquired using a 50 μm thick diamond radiator. In order to run the photon tagger at an acceptable rate this required an incident electron beam with a currents ~ 7 nA. This was close to the lower limit of what the accelerator could produce with the desired stability for any length of time. The 20 μm thick diamond radiator which would have allowed experimental running with higher currents, and therefore better stability and slightly lower rates, was suspected to have been mounted poorly. This thinner radiator would have resulted in less multiple scattering and therefore a higher degree of linear polarisation. It would be essential for future runs under the same limitations with the incident electron beam to have a thinner diamond to avoid these problems.

7.3 Summary

From the measurements made in this work and the efforts of the g8 collaboration throughout these last few years much has been learned about experimental run-

ning with a polarised source. By the end of the second phase of g8 experiments we expect to have a high quality data set which will not only allow a better measurement of Σ, but also improved measurements of the spin density matrix elements for the ρ^0 and a full partial wave analysis.

Appendix A

The Theory of Coherent Bremsstrahlung

An electron incident on a suitably orientated radiator [47] will be decelerated by the electromagnetic field of the radiator's nuclei, thus emitting an energetic photon. The reaction is represented by $e + N \rightarrow e^{'} + N + \gamma$, where N represents the nuclei involved in the interaction, e and $e^{'}$ represent the incident and degraded electron respectively, and γ represents the photon. The kinematics are described by the following relations;

$$\overrightarrow{p_0} = \overrightarrow{q} + \overrightarrow{p} + \overrightarrow{k} \qquad E_0 = E + k \tag{A.1}$$

where $\overrightarrow{p_0}$, $\overrightarrow{p}$, $\overrightarrow{k}$ and E_0, E, k are the momenta and energy of the incident electron, degraded electron, and photon respectively. The recoil momentum transferred to the crystal lattice is represented by $\overrightarrow{q}$. The natural emission angle of the photons at high energies, also known as the bremsstrahlung characteristic angle, is given by $\theta_\gamma = \frac{m_e c^2}{E_0}$.

It has been shown by Uberall [84] that $\overrightarrow{q}$ is confined to a thin region in momentum-space. A crude approximation of this region is defined by the limits;

$$\delta \leq q_l \leq 2\delta \qquad 0 \leq q_t \leq 2x \tag{A.2}$$

where q_t and q_l are the transverse and longitudinal components of $\overrightarrow{q}$, the relative quantum energy $x = \frac{k}{E_0}$, and δ denotes the minimum longitudinal recoil momentum. This kinematical region was called the momentum "pancake" by Uberall, and is depicted in Fig. A.1.

A diamond crystal is a common choice to produce coherent bremsstrahlung.

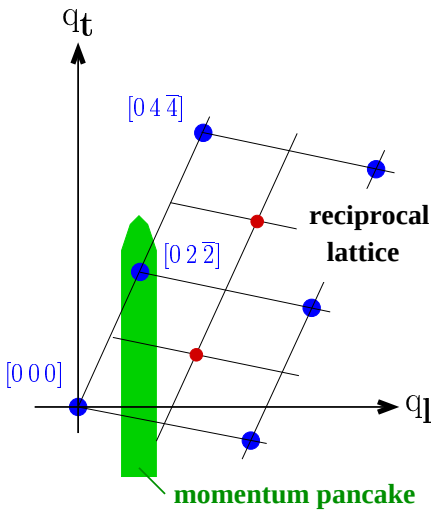

Figure A.1: The momentum "pancake". [...] denote the reciprocal lattice vectors.

It is chosen for it's small lattice constant and small atomic mass number, which favour the coherent intensity part of the bremsstrahlung produced. The radiator must be aligned correctly to select a specific energy range of photons with a high degree of linear polarisation. The alignment procedure is discussed further in Chapter 4.2, and Ref. [66]. In this process the recoil momentum is absorbed by the diamonds lattice. This happens when a reciprocal lattice vector lies inside the momentum pancake, as is shown in Fig. A.1.

As the bremsstrahlung photon energy increases, the pancake can be imaged to move through momentum space. As a new reciprocal lattice point enters the region it contributes to the spectra, and likewise as a reciprocal lattice vector leaves the pancake it ceases to contribute. Since the diamond momentum space is occupied at discrete intervals, as a reciprocal lattice vector is lost we see a discontinuous drop in intensity and polarisation. Fig. 3.7 represents this with simulation based on the anb code [48].

Bibliography

[1] B.A.Mecking et al. *Nucl. Inst. Meth. A*, 503:513–553, 2003.

[2] JLab, http://www.jlab.org.

[3] P.Cole, J.Connelly, and K.Livingston. Photoproduction of the ρ Meson from the Proton with Linearly Polarized Photons. JLab proposal E-94-109, 1994.

[4] F.Klein and P.Cole. Photoproduction of ω Mesons off Protons with Linearly Polarized Photons. JLab proposal E-99-013, 1999.

[5] D.Tedeschi, P.Cole, and J.Mueller. Photoproduction of ϕ Mesons with Linearly Polarized Photons. JLab proposal E-98-109, 1998.

[6] F.Klein, J.Kellie, and J.C.Sanabria. Photoproduction of Associated Strangeness using a Linearly Polarized Beam of Photons. JLab CAA, 2001.

[7] Q.Zhao et al. *Phys. Rev. C*, 58, 1998.

[8] M.Gell-Mann and Y.Ne'eman. *The Eightfold Way.* W.A.Benjamin, inc., 1964.

[9] D.H.Perkins. *Introduction to High Energy Physics 2nd Edition.* Addison Wesley, 1982.

[10] S.Boffi et al. *Electromagnetic Response of Atomic Nuclei.* Oxford Science Publications, 1996.

[11] J.Hamilton and B.Tromborg. *Partial Wave Amplitudes and Resonance Poles.* Oxford Clarendon Press, 1972.

[12] D.B.Lichtenberg. *Phys. Rev.*, 178:2197, 1969.

[13] R.E.Cutkosky and R.E.Hendrick. *Phys. Rev. D*, 16:2902, 1977.

[14] R.Koniuk and N.Isgur. *Phys. Rev. D*, 21:1868, 1980.

[15] S.Capstick and N.Isgur. *Phys. Rev. D*, 34:2809, 1986.

[16] S.Capstick and W.Roberts. *Phys. Rev. D*, 47:1994, 1993.

[17] P.Cole. *FIZIKA B (Zagreb)*, 8:71–80, 1999.

[18] C.P.Forsythe and R.E.Cutkosky. *Z. Phys. C*, 18:219, 1983.

[19] D.E.Groom et al. *Eur. Phys. C*, 15:1, 2000.

[20] ELSA, http://www-elsa.physik.uni-bonn.de.

[21] ESRF, http://www.esrf.fr.

[22] SPring-8, http://www.spring8.or.jp.

[23] T.H.Bauer et al. *Rev. Mod. Phys.*, 50:261, 1978.

[24] A.Donnachie et al. *J. Phys. G: Part. Phys.*, 22:733–740, 1996.

[25] G.L.Rakness. *Spin polarization transfer in exclusive ϕ electroproduction.* PhD thesis, University of Colorado, 2000.

[26] P.D.B.Collins. *An Introduction to Regge Theory.* Cambridge University Press, 1977.

[27] G.A.Schuler et al. *Nucl. Phys. B*, 407:539, 1993.

[28] J.A.Crittenden. *Springer Tracts in Modern Physics*, 140, 1997.

[29] Q.Zhao. Vector meson production in the quark model. *World Scientific*, Submitted June, 2001.

[30] Q.Zhao. Personal correspondence, qiang.zhao@surrey.ac.uk.

[31] F.J.Klein. *Bonn-IR-96-008.* PhD thesis, University of Bonn, 1996.

[32] πn newslett. 14, 141 (1998).

[33] Q.Zhao. *Phys. Rev. C*, 63, 2001.

[34] JLab exp E91-016: Omega Analysis. http://www.jlab.org/ pawel/omega.html.

[35] P.Ambrozewicz. http://www.jlab.org/ pawel/common phi/compare.html, Oct 2003.

[36] ABBHHM Collaboration. *Phys. Rev.*, 175:1669, 1968.

[37] H.R.Crouch et al. *Phys. Rev.*, 155:1448, 1967.

[38] Y.Eisenberg et al. *Phys. Rev. D*, 5:15, 1972.

[39] Y.Eisenberg et al. *Phys. Rev. Lett.*, 22:669, 1969.

[40] D.P.Barber. *Z. Phys. C*, 26:343, 1984.

[41] J.Ballam et al. *Phys. Rev. D*, 7, 1973.

[42] W.Struczinski et al. *Nucl. Phys. B*, 108:45, 1976.

[43] R.Beck. *Phys. Rev. Lett.*, 78:606–609, 1997.

[44] Mainz Microtron, http://www.kph.uni-mainz.de.

[45] C.W.Leemann et al. *Annu. Rev. Nucl. Part. Sci*, 51:413–50, 2001.

[46] D.Sober et al. *Nucl. Inst. Meth. A*, 440:263–284, 2000.

[47] U.Timm. *Fortschritte der Physik*, 19:765, 1969.

[48] A.Natter. http://www.pit.physik.uni-tuebingen.de/grabmayr/software/brems/brems-analytic.html.

[49] W.J.Briscoe et al. NSF Major Research Instrumentation, NSF Award 9724489.

[50] J.Kellie et al. The Selection of Diamond Radiators for use in Coherent Bremsstrahlung Experiments, preprint submitted to Elsevier Science 13 June 2002.

[51] B.K.Tanner. *X-ray diffration topography.* Pergamon, 1976.

[52] B.K.Tanner and D.K.Bowen. *High resolution X-ray diffractometry and topography.* Taylor and Francis, 1998.

[53] P.Cole. The IPN-Orsay/UTEP Instrumented Collimator. JLab internal publication, 1999.

[54] S.Christo. http://www.jlab.org/ christo/.

[55] O.Pogorelko et al. Mini Torus Magnet for CLAS, JLab internal document, 1993.

[56] S.Taylor et al. *Nucl. Inst. Meth. A*, 462:484, 2001.

[57] M.D.Mestayer et al. *Nucl. Inst. Meth. A*, 449:81–111, 2000.

[58] G.Adams et al. *Nucl. Inst. Meth. A*, 465:414, 2001.

[59] E.S.Smith et al. *Nucl. Inst. Meth. A*, 432:265–298, 1999.

[60] L.C.Smith et al. *Nucl. Inst. Meth. A*, 460:239, 2001.

[61] D.C.Doughty et al. *Nucl. Sci. IEEE Transactions*, 39:241–247, 1992.

[62] D.Cords et al. CLAS Event Format with BOS, CLAS-NOTE 94-012, 1994.

[63] V.Blobel et al. The BOS System for CLAS Detector, Unpublished, 1995.

[64] D.Axmark et al. http://www.mysql.com, since 1980s.

[65] D.Weygand et al. On CUE at JLab "a1c" is accessible from: cvs co /packages/utilities/a1.

[66] K.Livingston. The Stonehenge Technique. Unpublished, to be submitted to Nucl. Inst. Meth. A.

[67] Lothmon et al. *Nucl. Inst. Meth. A*, 343:494, 1994.

[68] C.Gordon, J.Melone and J.C.Sanabria. On CUE at JLab "st dt" is accessible from: cvs co /packages/utilities/st dt.

[69] D.Price. http://www.cvshome.org.

[70] E.Anciant et al. Tagger hit reconstruction software and tagger calibration overview. CLAS-NOTE 99-004, 1999.

[71] E.S.Smith et al. Calibration of the CLAS TOF System, CLAS-NOTE 99-011, 1999.

[72] D.Lawrence et al. CLAS Drift Chamber Calibration: Software and Procedures, CLAS-NOTE 99-018, 1999.

[73] M.Guillo et al. EC Time Calibration Procedure For Photon Runs in CLAS, CLAS-NOTE 01-014, 2001.

[74] P.Cole and R.Mammei. g8a active collimator calibration technique, cole@jlab.org, mammei@jlab.org.

[75] E.Pasyuk and L.Tudor. GPID scheme for photon running in CLAS, Unpublished CLAS-NOTE.

[76] E.Pasyuk. Energy loss routine on JLab CUE: cvs co /packages/eloss.

[77] J.Li. Personal correspondence, liji@jlab.org.

[78] R.H.Dalitz. *Phil. Mag.*, 44:1068, 1953.

[79] GSIM, http://www.jlab.org/Hall-B/document/gsim/userguide.html.

[80] Geant, http://wwwasd.web.cern.ch/wwwasd/geant/.

[81] The EPICS website, http://www.aps.anl.gov/epics/.

[82] C.Gordon, J.Melone and P.Cole. Vector Meson and Associated Strangeness Production Using a Linearly Polarised Photon Beam at Jefferson Lab. Fizika B (Zagreb), submitted September 2003.

[83] W.Roberts. Report to the GRAAL Group on Photoproduction of Baryon Resonances Using Polarised Photons (1994), unpublished.

[84] H.Uberall. *Phys. Rev.*, 103:1055, 1956.